A Wearable Transcranial Doppler Ultrasound Phased Array System

by

Sabino Joseph Pietrangelo

B.Sc., University of Michigan – Ann Arbor (2008)
S.M., Massachusetts Institute of Technology (2013)

Submitted to the Department of Electrical Engineering and Computer Science in partial fulfillment of the requirements for the degree of

Doctor of Philosophy

at the

MASSACHUSETTS INSTITUTE OF TECHNOLOGY

February 2017

Author . . . .
Department of Electrical Engineering and Computer Science
January 9, 2017

Certified by . . . .
Charles G. Sodini
LeBel Professor of Electrical Engineering
Thesis Supervisor

Certified by . . . .
Hae-Seung Lee
ATSP Professor of Electrical Engineering
Thesis Supervisor

Accepted by . . . .
Leslie A. Kolodziejski
Chairman, Department Committee on Graduate Students

A Wearable Transcranial Doppler Ultrasound Phased Array System

by

Sabino Joseph Pietrangelo

B.Sc., University of Michigan – Ann Arbor (2008)

S.M., Massachusetts Institute of Technology (2013)

Submitted to the Department of Electrical Engineering and Computer Science
on January 9, 2017, in partial fulfillment of the
requirements for the degree of
Doctor of Philosophy

Abstract

Transcranial Doppler (TCD) sonography is a specialized ultrasound technique that enables measurement of blood flow velocity from the basal intracerebral vessels. Use of TCD sonography is highly compelling as a diagnostic modality due to its safety in prolonged studies, high temporal resolution, and relative portability. Although TCD methods have been clinically indicated in a variety of cerebrovascular diagnostic applications, general acceptance by the medical community has been impeded by several critical deficiencies – including the need for a highly-trained TCD operator, operator dependent measurement results, and severe patient movement restrictions.

This thesis seeks to mitigate such limitations through the development of a compact, wearable TCD ultrasound system, permitting untethered cerebrovascular monitoring with limited operator interaction. The prototype system incorporates a custom two-dimensional transducer array and multi-channel transceiver electronics, thereby facilitating acoustic focusing via phased array operation. Algorithmic vessel search and tracking further reduce operator dependencies by expediting vessel localization, systematizing vessel identification, and dynamically adapting to relative vessel position. Additionally, focal correction methods are presented, which improve acoustic beamformation capabilities in the presence of tissue inhomogeneities.

Validation of the prototype hardware and embedded signal processing implementations under flow phantom and human subject testing yields high correlation with accepted velocimetry methods. Vessel search and tracking functionality are also verified experimentally. Circuit integration is explored to further reduce instrumentation dimensions and power consumption.

Thesis Supervisor: Charles G. Sodini
Title: LeBel Professor of Electrical Engineering

Thesis Supervisor: Hae-Seung Lee
Title: ATSP Professor of Electrical Engineering

Acknowledgments

I'd like to thank my parents and sisters for their enduring support. My family was an unending source of encouragement and perspective throughout this lengthy and occasionally turbulent journey. I want to express gratitude to my research advisors – Professors Charles Sodini and Hae-Seung Lee – and the rest of my thesis committee – Professor Thomas Heldt – for their mentorship, advice, and technical insight.

I also want to acknowledge my friends and colleagues – especially Michael Tomovich – for their assistance, understanding, and loyalty. When challenges arose, I was never alone.

Support from the MIT Medical Electronic Device Realization Center and its member companies is greatly appreciated and has made my graduate studies a practical reality. In particular, I'd like to thank Maxim Integrated and Dr. Brian Brandt for their continued involvement and guidance.

This work was sponsored in part by the MIT Medical Electronic Device Realization Center (MEDRC).

Contents

List of Figures

List of Tables

Chapter 1

Introduction

1.1 Background

Brain injury is often the result of a disturbance in the capacity of the cerebrovasculature to adequately perfuse the brain parenchyma. As such, characterization of cerebral blood flow (CBF) and its associated factors are of prime importance in neurocritical care, neurology, and related medical fields.

Traditional reference standards for assessing cerebrovascular state – notably cerebral angiography, electromagnetic flowmetry, and intracranial pressure (ICP) monitoring via intraventricular catheterization – are invasive in nature and associated with non-negligible rates of morbidity and mortality [1, 2]. Such invasive techniques are therefore clinically indicated only in severe pathological conditions, where their inherent risks can be justified.

The development of minimally-invasive, contrast-enhanced imaging methods – specifically computed tomographic angiography (CTA) and magnetic resonance angiography (MRA) – has provided clinicians the ability to evaluate cerebrovascular state at greatly reduced risks of complication. Although CTA and MRA are highly sensitive and specific in revealing a variety of cerebrovascular abnormalities, they pose several considerable limitations in clinical practice [3].

CTA and MRA imaging require expensive (several $100k to several $1M) stationary capital equipment and are therefore inaccessible or unavailable in many clinical environments. CTA and MRA may not be appropriate in all patient populations due to risks associated with their use. Such risks include allergy or toxicity to contrast media, internal metal objects (e.g., pacemakers, surgical clips, screws) in MRA, and exposure to ionizing radiation in CTA. Additional impediments to the usage of these methods include subject immobilization, procedure cost, and exam duration. CTA and MRA are useful diagnostic tools for assessing patient state at a single point in time, but are generally unfeasible for applications requiring continuous monitoring or repeated serial measurements.

The brain, however, is a dynamic organ and blood flow disruption is often exceedingly variable in time. Therefore, developments in continuous, real-time monitoring of intracranial dynamics using noninvasive methods are highly desirable, especially in clinical circumstances when direct invasive measurement is not feasible or bears too great a risk [4].

1.2 Motivation

Transcranial Doppler (TCD) sonography is a specialized Doppler ultrasound technique that enables measurement of blood flow velocities from the basal intracerebral vessels and is clinically indicated in a variety of diagnostic and prognostic cerebrovascular applications. TCD methods use a moderate frequency ($\approx 1-2$MHz) acoustic source to penetrate cranial bone and insonate the intracerebral arteries. Backscattered acoustic energy from erythrocytes and other scatterers moving through a predefined sample volume generates disturbances in the echo data received by TCD instrumentation. A time-varying cerebral blood flow velocity (CBFV) measurement is computed through spectral analysis of received echo data. Clinically relevant parameters, including flow direction, peak systolic and end diastolic flow velocity, time-average flow velocity, and pulsatility index, are extracted from the CBFV waveform [5].

TCD sonography is employed in a variety of clinical applications, including identification of intracranial vasospasm and stenosis, intra-operative monitoring, stroke risk stratification, and assessment of cerebrovascular autoregulation [6, 7]. A comprehensive evidence-based review of clinical TCD applications is found in [2].

The use of TCD sonography is compelling for certain diagnostic needs due to:

1. **Safety**

   The basic measurement technique is completely noninvasive and considered extremely safe, requiring no administration of contrast dyes, tracers, or ionizing radiation sources. There have been no reports of measurement related complications under standard diagnostic use [5].

2. **High temporal resolution**

   CBFV waveform sample rates > 100Hz enable sufficient resolution to assess cerebral hemodynamics – including autoregulation and CO_2 reactivity [8]. TCD is also capable of resolving the transient characteristics of circulating cerebral emboli [9].

3. **Real-time functionality**

   Negligible delay (< 0.5s) between current cerebrovascular state and subsequent measurement outputs is advantageous in emergent, intra-operative, and interventional settings, where guidance to clinicians is highly time-sensitive.

4. **Instrument portability**

   Cart-based sonography instrumentation is amenable to bedside evaluation in the intensive care unit, angiography suite, and operating room [5].

5. **Modest cost of assessment**

   Moderate capital costs of TCD instrumentation and limited variable costs – principally sonographer evaluation and clinician interpretation resources – yield relatively inexpensive assessment costs compared to other noninvasive cerebrovascular diagnostics [5, 8].

Among existing noninvasive diagnostics, TCD sonography is uniquely suited to achieve such objectives as a practicable modality for prolonged monitoring and repeated measurements.

Despite its advantages, the use of TCD sonography is typically confined to highly-specific clinical settings and the reliability of transcranial velocimetry data has not been generally accepted by the medical community [6, 10, 11]. Several constraints have impeded the extension of TCD sonography to broader contexts, including:

1. **Need for skilled TCD operator**

   Conventional TCD examination techniques require considerable operator training, fine manual dexterity, and extensive knowlege of the underlying cerebral anatomy [12, 13]. An experienced TCD operator – typically a sonographer, technologist, or clinician – must rely on auditory and visual cues and extensive examination guidelines throughout the course of measurement. The expertise required for proper TCD evaluation is not generally available outside of specialized clinical environments (e.g., neurocritical care units, vascular laboratories).

2. **Inter-operator variability**

   In practice, TCD sonography is a highly operator dependent technology. Variability is predominantly affected by operator proficiency in acoustic window location, intracranial vessel identification (including anatomic variations), probe placement and angulation, and range gate selection [6]. Measurement reproducibility is generally related to operator experience, with measurement error being lowest in highly-trained, well-practiced operators [10]. However, studies have revealed significant inter-operator variability in Doppler velocimetry data among even experienced operators [14, 15].

   In one study, aberrant results in several examinations performed by experienced operators led the authors to conclude that caution must be used when interpreting isolated CBFV data and that treatment decisions should never be made without repeated observations combined with additional clinical parameters [14, 16]. Because intra-operator measurements are less variable, it is highly preferable – although generally impractical – that serial TCD evaluations are performed by a single operator [14].

   Advances in TCD instrumentation – notably power motion-mode Doppler (PMD), which uses multi-gate sampling to provide flow signal intensity and direction across a broad range of intracranial depths, and transcranial color-coded sonography (TCCS), which employs duplex mode operation (i.e., Doppler and imaging) to display spatial dependence of flow, have enhanced operator visibility into the underlying anatomy [2, 17]. In general, such methods have demonstrated improved measurement reproducibility and diagnostic specificity, but remain heavily operator dependent [2, 18].

3. **Acoustic window patency**

   Inadequate acoustic window patency, resulting in no discernible Doppler flow signal, occurs in approximately 5 - 10% of the population [9, 19]. A patent temporal acoustic window (TAW) – the primary location for middle cerebral artery (MCA) insonation – was not identified in 8.2% of subjects in [20]. Lack of TAW patency is generally related to increased thickness of the temporal bone squama and has markedly higher rates of prevalence in non-white races, females, and patients aged 65 and older [20].

   Ultrasonic contrast agents may be used to improve TAW patency by considerably enhancing the effective scattering coefficient of blood and therefore greatly increasing the intensity of the backscattered acoustic signal [21]. However, administration of contrast agents requires intravenous injection, making the examination an invasive procedure and notably complicating its administration. Use of ultrasonic contrast agents are not considered in this work.

4. **Measurement locality**

   CBFV measurements via TCD sonography are limited to accessible segments of large diameter ($\gtrsim$ 1mm) intracranial vessels. TCD assessment is therefore most applicable when diagnosis pertains directly to the relevant measured vessel segment. TCD sonography can also detect indirect effects – such as abnormal waveform characteristics – suggestive of proximal hemodynamic or distal obstructive lesions [2]. Such indirect findings may be clinically informative, but are also generally inconclusive.

5. **Severe patient movement restrictions**

   Patients must remain rather still during the entirety of testing. For prolonged TCD monitoring, a probe-fixation headframe can be employed after an acceptable Doppler signal is obtained, but is generally only marginally effective [5]. Patient movement can create probe misalignment and a consequent loss of signal fidelity. The frequency and impact of probe displacement is highly dependent on measurement application, being remarkably problematic in prolonged evaluation of non-comatose patients [11]. An operator must therefore assess measurement results throughout the entirety of TCD monitoring to ensure adequate signal quality and suitable probe placement.

   Although instrumentation is modest in dimensions – relative to other cerebrovascular imaging modalities – cart-based systems preclude the use of TCD sonography in ambulatory measurements. Basic wearable TCD systems have demonstrated progress toward extended ambulatory monitoring, but with limited capabilities [22,23]. Despite existing for general ultrasound indications, a highly-portable transcranial duplex sonography system has not yet been developed [2,24].

6. **Doppler angle effect**

   Measured flow velocities reflect a cosine dependence on the angle between arterial flow and direction of acoustic propagation – known as the Doppler angle. Certain pathologies – such as intracranial stenosis – can be identified using TCD sonography by the existence of high velocity jets exceeding a predetermined threshold velocity. However, the existence of non-negligible Doppler angle can significantly reduce measured flow velocities and therefore degrade diagnostic sensitivity, especially for Doppler angles above $> 20°$.

   Angle correction can be employed by color flow imaging (CFI) capable instrumentation, particularly TCCS, increasing flow velocities by $25 - 30\%$ in some subjects [2]. TCCS, however, often suffers from exceedingly poor spatial resolution due primarily to distortion of the ultrasound beam through cranial bone [25]. Additionally, planar TCCS imaging may generate inaccurate Doppler angle values due to the three-dimensional course of intracranial arteries [2].

TCD sonography is a rapidly evolving diagnostic modality with a broad range of established and emerging clinical applications and a direct impact on patient management [17]. Recent technological developments in TCD instrumentation – notably PMD and TCCS – have enhanced the usability and clinical utility of TCD sonography, but have failed to fully resolve numerous common deficiencies. Advances in noninvasive diagnostic modalities that facilitate real-time, continuous monitoring of cerebrovascular state can profoundly alter the standard clinical approach to cerebrovascular evaluation. This work, therefore, seeks to identify and further enhance the functionalities necessary for broad clinical acceptance of sonographic transcranial velocimetry.

1.3 Approach and Thesis Contributions

Recent advances in ultrasound electronics and system architectures have led to substantial reductions in instrumentation dimensions (e.g., GE Vscan, Siemens Acuson P10). This work extends such decreases in system dimensions to a wearable form factor by identifying the anatomical, physiological, and algorithmic constraints particular to portable TCD sonography.

The use of a two-dimensional (2D) ultrasound transducer array and beam steering algorithms allows for autonomous vessel location and tracking. Automated mechanical steering – via servo control – has been previously investigated and successfully demonstrated for TCD vessel tracking, but is considerably limited by the single allowable steering direction of a transducer element [22, 26]. A phased array approach, in contrast, can establish multiple concurrent focal regions and thereby achieve background vessel tracking and focal point optimization without interruption to flow velocity measurements. Phased array implementations – in addition to beam steering – enable adjustable beam focusing, which can yield – for a fixed acoustic output power – a significant increase in acoustic intensity at the region of interest than can be achieved in the planar (i.e., unfocused) single element transducers commonly used in TCD instrumentation [17, 26]. Additionally, phased array beamformation permits the application of phase correction techniques to further improve energy focusing and mitigate the effects of refraction and focal aberrations [27, 28].

To facilitate development and limit system complexity, this work concentrates on unilateral TAW insonation of the MCA for velocimetry applications. Although this decision generally restricts the clinical utility of the system, it proves sufficient for a number of TCD applications. Of the major cerebral vessels, insonation and spectral Doppler (i.e., non-imaging) identification of the MCA through the TAW is generally the most straightforward due to favorable anatomical structure. The MCA is a high flow velocity, relatively large diameter cerebral vessel with approximately lateral course (i.e., normal to skull surface). TAW insonation of the ipsilateral MCA thereby typically results in limited steering angle magnitude ($< 15^\circ$ in azimuth and elevation planes), modest Doppler angle, and moderate insonation depths (30 – 60mm). Further efforts to expand insonation capabilities to additional cerebral vessels (e.g., anterior and posterior cerebral arteries) will not be discussed; the majority of analyses and designs presented in this work, however, remain valid [6].

Ultrasound field solvers, particularly Field II and k-Wave, are used extensively in the evaluation of acoustic propagation and refinement of signal processing techniques [29–31]. Although such simulation tools do not provide a suitable treatment of noise effects, nonlinearities, and other relevant phenomena, they are useful in validating functionality and comparing design performance metrics through simplifying assumptions.

This thesis describes the design and operation of a TCD phased array prototype system. The prototype system was architected, fabricated, and experimentally characterized. *In vivo* human validation of prototype system CBFV measurements at the MCA is also investigated by comparing velocimetry data to measurements from a commercial TCD system.

To expedite development, system implementations leverage commercially available discrete electronic components. Because access to internal nodes within discrete components is restricted and device operation is generally predefined, this decision severely limits the extent of realizable architectures. For this work, a fully digital phased array, with dedicated transmit and receive electronics for each array element, was selected due to its fully software defined configurability and ease of implementation when utilizing existing commercial electronics. Although this approach is somewhat excessive in terms of electronic hardware, power dissipation, and intermediate data rates – as compared to more elegant mixed-signal architectures – it provides a reasonable means of determining typical underlying signal levels, algorithm performance for practical *in vivo* measurements, and the general viability of wearable TCD sonography. Electronic beam steering algorithms for vessel location and tracking are developed and experimentally refined. Following validation of the discrete prototype system, an application specific integrated circuit (ASIC) based architecture is explored.

The major contributions of this work include:

1. Development of compact TCD velocimetry instrumentation in a wearable, untethered form factor.
2. Electronic beamformation via phased array operation for energy steering and focusing through the TAW.
3. Embedded vessel search algorithms for autonomous and rapid localization of maximum Doppler power regions.
4. Embedded vessel tracking algorithms for autonomous updating of focal position during prolonged monitoring – without introducing degradation to simultaneous flow velocity measurements.
5. Focal correction techniques to reduce effects of tissue inhomogeneities on phased array beamformation.
6. Investigation and design of an ASIC-based phased array TCD velocimetry system for reductions in power consumption, instrumentation dimensions, and improved functionality.

1.4 Thesis Organization

This thesis begins with a general description of acoustic theory relevant to diagnostic ultrasound instrumentation in Chapter 2. Following an explanation of fundamental principles of operation, Chapter 3 present the anatomical and physiological parameters, safety considerations, and other system constraints relevant to transcranial sonography.

Doppler signal processing and system control algorithms are developed in Chapter 4. A discrete TCD system architecture, hardware design, and prototype implementation are defined in Chapter 5. Experimental characterization and human subject validation of the discrete prototype are presented in Chapters 6 and 7, respectively. Integration of transceiver electronics into an ASIC and the development of an integrated system prototype is detailed in Chapter 8.

Chapter 9 presents a summary of this work. Functionality and performance of the devised system architectures are reviewed. Necessary future work and the identification of enhancements to subsequent system designs and implementations are also discussed.

Chapter 2

Principles of Operation

2.1 Acoustic Theory

Ultrasound is a cyclic acoustic disturbance at frequencies above the limit of human hearing (> 20 kHz). Acoustic energy perturbs the particles composing a propagating medium, causing them to oscillate about their equilibrium positions with no net displacement and producing local fluctuations in pressure. Because fluids continually deform under shear stress, a fluid medium can only support longitudinal acoustic waves, thereby confining particle motion along the direction of propagation. Human tissue is predominately an elastic solid comprised of complex structural formations and nonuniform interfaces. Due to its high water content, tissue is often approximated as a fluid acoustic medium. This simplification is less appropriate for highly anisotropic (e.g., striated muscle) and particularly dense (e.g., bone) structures, but allows for reasonably tractable analysis of acoustic radiation [6].

Acoustic waves, like all physical processes, are fundamentally nonlinear. Finite pressure amplitudes cause variations in wave velocity, resulting in progressive waveform distortion and harmonic frequency generation [32]. Use of linear acoustic models for diagnostic ultrasound applications is normally justified as they capture most salient features of propagation and provide insight into underlying phenomena without excessively complicating analysis [6]. An in-depth discussion of elastic waves in solids and nonlinear acoustics are beyond the scope of this thesis and are described fully in [32]. A fluid acoustic medium and linear wave propagation are assumed for the remainder of this work, unless explicitly stated.

Consequently, vibrations in Cartesian space can be described by the linear wave equation:

$$\left(\frac{\partial^2}{\partial x^2}+\frac{\partial^2}{\partial y^2}+\frac{\partial^2}{\partial z^2}\right)u(x,y,z,t)=\frac{1}{c^2}\frac{\partial^2 u(x,y,z,t)}{\partial t^2} \tag{2.1}$$

where u denotes the magnitude of instantaneous particle velocity (i.e., $u = |\vec{u}|$), (x, y, z, t) are spatiotemporal Eulerian coordinates, and c is the velocity of propagation. The wave equation can, in general, express multiple modes of propagation. However, because a fluid medium is assumed, longitudinal mode vibration is implied [6].

Propagation velocity (c) and wavelength (λ) are influenced by the mechanical properties of a medium. Although velocity is strictly dependent on wave amplitude, use of the linear propagation assumption yields a single value within a given medium – assuming negligible dispersion effects.

$$c=\sqrt{\frac{1}{\rho_0\kappa}} \tag{2.2}$$

$$\lambda=\frac{c}{f}=\frac{1}{f\sqrt{\rho_0\kappa}} \tag{2.3}$$

where f is the frequency of oscillation (related to angular frequency ω by $f = \frac{\omega}{2\pi}$), ρ_0 is mean density, and κ is the adiabatic compressibility of the material [33].

Pressure variations (p) – referenced to static pressure – and particle velocity magnitude are related by the characteristic acoustic impedance Z:

$$Z=\frac{p}{u}=\rho_0 c \tag{2.4}$$

Characteristic acoustic impedance is typically given in units of rayls ($1\,\mathrm{rayl} = 1\,\mathrm{kg}\cdot\mathrm{s}^{-1}\cdot\mathrm{m}^{-2}$) and – for the purposes of medical ultrasound applications – is significant at the interface of dissimilar media due to reflection effects [6,32].

Attenuation in tissue arises from several complex phenomena and is difficult to precisely derive from fundamental principles. Phenomenological models are generally used to combine various sources of energy loss by employing a single frequency-dependent attenuation factor $\alpha(f)$ [6]:

$$\alpha(f) = \alpha_0 + \alpha_1 f \tag{2.5}$$

where the offset term is commonly neglected ($\alpha_0 \approx 0$), α_1 is determined empirically for a specific medium, and α is often expressed in $\mathrm{Np \cdot cm^{-1}}$. Because both are based on the logarithmic scale, conversion between Neper and decibel is direct ($1\,\mathrm{Np} = 8.686\,\mathrm{dB}$).

Acoustic parameters are given for media relevant to transcranial Doppler (TCD) applications in Table 2.1. In biological media, acoustic properties are highly influenced by myriad factors (e.g., blood hematocrit, tissue water content, bone density) and can differ appreciably between specimen and in varying environmental conditions [6].

Table 2.1: Acoustic parameters for selected media [25, 34].

Medium	Phase Velocity, c [m/s]	Impedance, Z [Mrayl]	Atten. Coefficient, α_1 [Np/ (cm · MHz)]
Air	333	0.0004	—
Water	1480	1.48	0.0002
Soft Tissue	1540	1.63	0.08
Blood	1580	1.67	0.02
Brain	1460	1.50	0.06
Cranial Bone	2770	4.80	2.5

Acoustic intensity (I), known also as power density, is the instantaneous flux of acoustic power across a unit area normal to the direction of propagation. Intensity has a spatiotemporal dependence and is expressed as:

$$I(\vec{r},t) = p(\vec{r},t) \cdot u(\vec{r},t) = \frac{p(\vec{r},t)^2}{Z} = u(\vec{r},t)^2 \cdot Z \tag{2.6}$$

where $\vec{r} = (r_x, r_y, r_z)$ is the spatial vector referenced to the origin. Intensity is often given in units of $\mathrm{mW} \cdot \mathrm{cm}^{-2}$ for medical ultrasound applications.

Time-average intensity $\langle I \rangle_t$ is useful in representing acoustic fields in pulsed ultrasound since it removes temporal dependence:

$$\langle I(\vec{r}) \rangle_t = \frac{1}{T_{PRP}} \int_0^{T_{PRP}} I(\vec{r}, t)\, dt \tag{2.7}$$

where T_{PRP} is the pulse repetition period (i.e., time between successive pulses) [6].

Acoustic intensity is highly relevant in characterizing safe use and regulatory limitations of sonography systems. Several derived variants, notably spatial-peak-temporal-peak intensity (I_{SPTP}) and spatial-peak-temporal-average intensity (I_{SPTA}), enable quantification of time-varying, spatially distributed acoustic fields with a single value [6]:

$$I_{SPTP} = \max\left\{ I(\vec{r}, t) \right\} \tag{2.8}$$

$$I_{SPTA} = \frac{1}{T_{PRP}} \int_0^{T_{PRP}} I(\vec{r}_{\max}, t)\, dt \tag{2.9}$$

where $\max\{\cdot\}$ denotes the maximum value across all valid inputs (i.e., $0 \leq t < T_{PRP}$ and $r_z > 0$) and $\vec{r}_{\max}$ is the position of maximum intensity.

2.1.1 Scattering

Scattering is the underlying physical phenomena that enables the use of ultrasound for diagnostic purposes. In Doppler sonography, backscattered energy from a collection of scatterers is utilized to characterize particle velocities.

Scattering of ultrasound energy occurs due to deviations in acoustic properties (e.g., density, compressibility) of the propagating medium. The behavior of acoustic waves upon encountering a scatterer (i.e., region with distinct acoustic properties) is highly affected by the dimensions of the scatterer relative to acoustic wavelength. Biological media contains structure over a wide range of length scales (e.g., molecules, cells, organs). In general, scattering effects can be separated into three dimension dependent categories: specular scattering, diffusive scattering, and diffractive scattering [6]. Diffractive scattering is less relevant to TCD sonography, but is described fully in [32].

Specular Scattering

Specular scattering, known simply as reflection, occurs for scatterer boundaries much larger than the acoustic wavelength and can be accurately analyzed using basic ray theory. Reflection mechanisms are independent of acoustic frequency, but are markedly influenced by boundary shape. A planar surface (i.e., flat boundary between dissimilar media) acts as a specular scatterer when $\min\{l_s\} \gg \frac{\lambda}{\pi}$, where $\min\{l_s\}$ is the smallest dimension of the surface. Certain organ boundaries and interfaces between bone and soft tissue can be approximated as planar surfaces over a restricted transverse extent [6].

In the specular regime, the interaction of an incident plane wave with a planar surface yields both reflected and transmitted plane waves, as shown in Figure 2-1, where Z_1 and Z_2 are the acoustic characteristic impedances of the incident and transmit media, respectively.

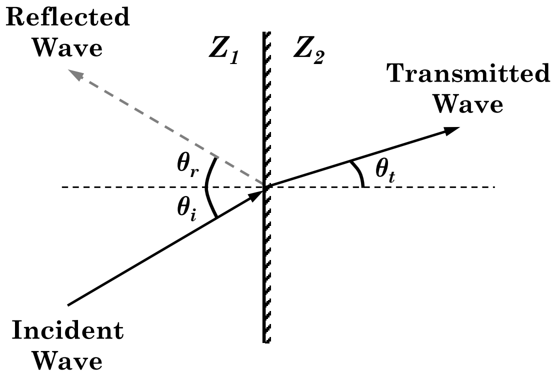

Figure 2-1: Specular scattering at a planar surface [6].

The relationship between the angles of incidence (θ_i), reflection (θ_r), and transmission (θ_t) are determined using Snell's law [35]:

$$\theta_r = \theta_i \tag{2.10}$$

$$\frac{\sin\theta_t}{\sin\theta_i} = \frac{c_2}{c_1} \tag{2.11}$$

where c_1 and c_2 are the propagation velocities within the incident and transmitted media, respectively. The resulting variation between the angle of incidence and angle of transmission is known as refraction. Recall from Table 2.1 that acoustic propagation velocity remains nearly constant for soft tissue, but diverges markedly in bone. Refraction effects are therefore most pronounced at interfaces between bone and soft tissue, particularly at oblique angles of incidence. For TCD applications, refraction due to cranial bone can lead to considerable beam pattern distortion, further complicating intracranial examination [27, 28].

The reflection coefficient (Γ) and transmission coefficient (T) describe the ratio between pressure wave magnitudes at the reflecting boundary. Assuming plane wave propagation:

$$\Gamma = \frac{p_r}{p_i} = \frac{Z_2\cos\theta_i - Z_1\cos\theta_t}{Z_2\cos\theta_i + Z_1\cos\theta_t} \tag{2.12}$$

$$T = \frac{p_t}{p_i} = \frac{2Z_2\cos\theta_i}{Z_2\cos\theta_i + Z_1\cos\theta_t} \tag{2.13}$$

where p_i, p_r, and p_t are the amplitudes of the incident, reflected, and transmitted pressure plane waves at the material interface, respectively.

Similarly, reflectivity (Γ_I) and transmissivity (T_I) characterize the relationship between acoustic plane wave intensities at the reflecting boundary [33]:

$$\Gamma_I = \frac{I_r}{I_i} = \Gamma^2 = \left(\frac{Z_2\cos\theta_i - Z_1\cos\theta_t}{Z_2\cos\theta_i + Z_1\cos\theta_t}\right)^2 \tag{2.14}$$

$$T_I = \frac{I_t}{I_i} = T^2\frac{Z_1}{Z_2} = \frac{4Z_1Z_2\cos^2\theta_i}{\left(Z_2\cos\theta_i + Z_1\cos\theta_t\right)^2} \tag{2.15}$$

where a planar reflecting surface larger than the insonated surface is assumed and I_i,

I_r, and I_t are the acoustic intensities of the incident, reflected, and transmitted plane waves at the material interface, respectively.

Acoustic reflection highlights a notable challenge associated with TCD sonography. Using characteristic impedance values for cranial bone and soft tissue from Table 2.1 – and approximating the cranial bone surface near the transducer as planar – yields a transmissivity of $T_I = 0.76$ for normal incidence. This suggests a significant decrease in the acoustic power transmitted through the skull due solely to characteristic impedance mismatch, in addition to beam refraction and increased attenuation through bone. Degradation of acoustic intensity due to reflection is further exacerbated by the pulse-echo nature of sonography, where acoustic propagation to and returning from the cerebral vessels encounters four distinct interfaces between bone and soft tissue. Although overly simplistic, neglecting the formation of standing wave patterns and the stratified internal structure of cranial bone, the preceding analysis of intracranial propagation illustrates a major limitation of transtemporal insonation in TCD sonography [6].

Diffusive Scattering

In contrast to reflection, diffusive scattering – known also as Rayleigh scattering – occurs when scatterer dimensions are much smaller than acoustic wavelengths. Rayleigh scattering is highly dependent on frequency, but ideally independent of scatterer shape and roughness features. For a spherical scatterer of diameter d_s, Rayleigh scattering occurs when $d_s \ll \frac{\lambda}{\pi}$ and results in the emission of an approximately spherical scattered wave.

For an individual scatterer, the differential scattering cross-section $\sigma_{ds}(\theta)$ defines the ratio of power scattered in a given direction $dp_s(\theta)$ to the differential solid angle $d\Omega$ and incident intensity I_i, where θ is the angle between the observation vector and the incident ray (i.e., z-axis in Figure 2-2). The differential scattering cross-section indicates the strength of scattering and is determined by both geometric (e.g., volume) and mechanical (e.g., density, compressibility) properties of the scatterer.

$$\sigma_{ds}(\theta) = \frac{dp_s(\theta)}{d\Omega I_i} \tag{2.16}$$

Parameters relevant to the analysis of diffusive scattering are shown in Figure 2-2.

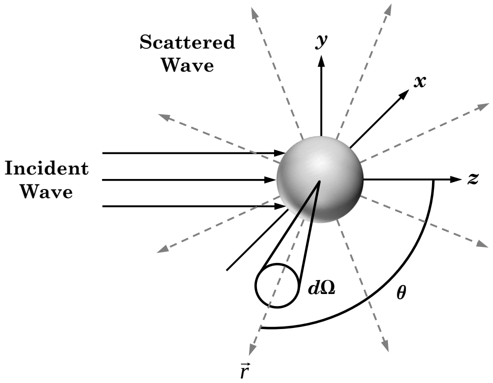

Figure 2-2: Diffusive scattering at a spherical scatterer [6].

For ideal diffusive scattering, the process is completely isotropic and $\sigma_{ds}(\theta)$ is constant across all angles, as expected for a spherical wave. In general, however, scattered intensity I_s from a single diffusive scatterer is dependent on both r and θ (neglecting attenuation effects):

$$\frac{I_s\left(r,\theta\right)}{I_i} = \frac{\sigma_{ds}\left(\theta\right)}{r^2} \tag{2.17}$$

Although diffusive scatterers cannot be individually resolved, scattering in this regime has important implications in sonography as tissue can often be modeled as an aggregate of sub-wavelength point scatterers. In medical Doppler ultrasound, diffusive scattering from blood is the fundamental mechanism that enables measurement of blood flow velocity [6].

Blood is not a homogeneous liquid but rather a suspension of cells and other particles within plasma. Erythrocytes (i.e., red blood cells) are flexible biconcave discs approximately 7μm in diameter by 2μm in thickness. Whole (i.e., unmodified) human blood contains approximately 5 million erythrocytes per microliter [32]. Erythrocytes make up roughly 45% of total blood volume, a value known as hematocrit (Ht). Scattering of ultrasound by blood is believed to be almost entirely due to erythrocytes [36]. Empirical measurements have established, however, that physical scattering of blood and other tissue structures remains partially anisotropic, even within the diffusive scattering regime [6, 37].

Neglecting structural complexities, a single erythrocyte can be accurately modeled as a spherical scatterer of equivalent volume, corresponding to a diameter of $\approx 6\mu$m. Considerable agreement between analytical and experimental results is achieved by representing the differential scattering cross-section of an erythrocyte as a function of angle between the incident ray and the observation vector (i.e., θ as shown in Figure 2-2) [38, 39].

$$\sigma_{ds}(\theta) = \frac{V_e^2 \pi^2}{\lambda^4} \left[\frac{\kappa_e - \kappa_f}{\kappa_f} + \frac{3(\rho_e - \rho_f)}{2\rho_e + \rho_f} \cos\theta \right]^2 \tag{2.18}$$

where V_e is erythrocyte volume, κ_e, ρ_e are erythrocyte compressibility and density, and κ_f, ρ_f are the compressibility and density of the surrounding fluid, respectively.

A scattered wave emanates from each erythrocyte within the region of insonation, yielding a Gaussian distribution of individual scattered wave intensities (I_s) that can be fully characterized by its mean and variance. This distribution arises mainly due to slight differences in the volume, compressibility, and density of each erythrocyte from the ensemble mean. In addition to amplitude deviations, every scattered waveform originates from an erythrocyte with unique spatial position. Appreciable phase offsets between scatterers thereby result in interference between scattered wavefronts. The preceding effects lead to the formation of a complex speckle pattern that, although often characterized using statistical terms, is deterministically related to the underlying tissue microstructure and acoustic instrumentation characteristics [6].

Diffusive scattering from a collection of point scatterers is characterized by the differential scattering coefficient $\mu_{ds}(\theta)$, which is the average power received from a volume of scatterers per steradian when insonated by a unit amplitude plane wave. The differential scattering coefficient – in the absence of multiple scattering – can thereby be expressed as the accumulative contribution for all scatterers:

$$\mu_{ds}(\theta) = \left| \sum_{n} f_{ds}(\vec{r_n})\, \sigma_{ds,n}(\theta_n) \right| \tag{2.19}$$

where $f_{ds}(\vec{r_n})$ is a scaling function between -1 and 1 accounting for position (i.e., $\vec{r_n}$) dependent phase interference effects and $\sigma_{ds,n}$ is the differential scattering cross-section of an individual scatterer [6].

For coincident transmit and receive apertures, the backscatter cross-section σ_{bs} and backscatter coefficient μ_{bs}, which characterize the power scattered in the direction of the incident source (i.e., $\theta = \pi$), are generally most relevant.

$$\sigma_{bs} = \sigma_{ds}(\pi) \tag{2.20}$$

$$\mu_{bs} = \mu_{ds}(\pi) \tag{2.21}$$

For media with no measureable spatial correlation in scattering properties, the scattering processing is incoherent and backscatter intensity is proportional to the number of insonated scatterers. At artificially low erythrocyte concentrations ($Ht <$ 8%), blood can be approximated as incoherent and the backscatter coefficient is approximately linearly proportional to the number of erythrocytes present within the volume of insonation [39]. At higher erythrocyte concentrations, the scattering process becomes exceedingly convoluted – likely resulting from multiple scattering effects and a progressive reduction in the incoherence of erythrocytes, which no longer behave as a random distribution of point scatterers. For *in vivo* erythrocyte concentrations (i.e, $Ht \approx 40 - 45\%$), the distance between scatterers becomes a modest fraction of erythrocyte diameter and therefore the position and motion of individual scatterers is highly dependent on surrounding erythrocytes [6, 39].

The effect of hematocrit on the backscatter coefficient of human blood can be expressed by the empirical relationship [40]:

$$\mu_{bs} = \frac{Ht(1 - Ht)^4}{(1 + 2Ht)^2} \frac{\sigma_{bs}}{V_e} \tag{2.22}$$

In practice, most insonation volumes for blood flow velocity estimation contain both erythrocytes and stationary tissue scatterers. For a given volume, stationary tissues (e.g., vascular wall structures) typically yield a substantial increase – by a factor of one to three orders of magnitude – in backscatter intensity when compared to erythrocyte scattering alone [33]. Although scattered power from stationary tissues, often referred to as clutter, can be attenuated via high-pass filtering during Doppler signal processing, the increased signal levels place considerable constraints on system dynamic range, clutter filter complexity, and transducer beamwidth to ensure velocimetry accuracy [6].

2.1.2 Tissue Inhomogeneities

The presence of rigid cranial bone between the acoustic transducer and cerebral arteries of interest has profound effects on the performance and operation of TCD ultrasound systems. Although soft tissue can be approximated as a fluid acoustic medium, transmission through bone further complicates propagation. In general, a longitudinal wave incident on the surface of bone, or any elastic solid, creates both longitudinal and shear transmitted waves [41]. Mode conversion is, however, highly dependent on the angle of incidence and numerical studies suggest that shear wave generation can be effectively neglected for the small incidence angles typically encountered in TCD evaluations ($\theta_i < 20°$) [42,43].

Transmission through bone leads to several other significant phenomena. The large difference in phase velocities between bone and soft tissue creates refraction in acoustic wave transmissions, which can substantially alter transducer beam patterns [28]. As discussed, the large mismatch in characteristic acoustic impedance at the interface between bone and soft tissue yields considerable reductions in transmitted wave intensity due to reflection effects. Cranial bone is also an extremely absorptive medium and its high attenuation factor further decreases wave intensity during propagation through the skull ($\sim 10 - 20$dB per transmission). The extent to which these preceding mechanisms influence acoustic propagation primarily determines the patency of acoustic windows (i.e., ability to receive a detectable Doppler signal) in patients undergoing TCD evaluation [6].

This work therefore generally incorporates basic homogeneous propagation models to guide system design choices. Experimental data from *ex vivo* cranial bone is utilized to evaluate the salient features of tissue inhomogeneities on expected signal levels (see Section 3.1.2).

2.1.3 Pulsed Wave Operation

Sonography can be categorized into two general classes of operation, continuous wave (CW) and pulsed wave (PW). Ultrasound imaging systems function solely in the PW regime due to spatial resolution concerns. Doppler sonography instrumentation, however, can employ both CW and PW modes. For transcranial measurements, CW operation is generally unfeasible since excessive reflection due to cranial bone produces severe system dynamic range requirements. In pulsed systems, the use of time-gating greatly reduces dynamic range concerns; PW operation is therefore of primary concern throughout this work.

PW excitation employs a gated periodic function to drive the transducer during the transmit phase. The basis function of pulsed excitation $e_{T0}\left(t\right)$ can be expressed as:

$$e_{T0}\left(t\right) = \prod\left(\frac{t}{T_e M} - \frac{1}{2}\right) e_{\text{periodic}}\left(t, T_e\right) \tag{2.23}$$

where $T_e = \frac{1}{f_e}$ is the fundamental period of $e_{\text{periodic}}\left(t, T_e\right)$, such that $e_{\text{periodic}}\left(t, T_e\right) = e_{\text{periodic}}\left(t + T_e, T_e\right)\ \forall t$ and M is the number of cycles (of period T_e) within a single gate.

The gating function $\prod\left(\frac{t - t_{\text{shift}}}{t_{\text{ON}}} - \frac{1}{2}\right)$ is a shifted, time-scaled rect function with interval $[t_{\text{shift}}, t_{\text{shift}+t_{\text{ON}}}]$, written as:

$$\prod\left(\frac{t - t_{\text{shift}}}{t_{\text{ON}}} - \frac{1}{2}\right) = \begin{cases} 1, & t_{\text{shift}} \leq t \leq t_{\text{shift}} + t_{\text{ON}} \\ 0, & \text{otherwise} \end{cases} \tag{2.24}$$

The basis function $e_{T0}\left(t\right)$ can therefore be alternately expressed as:

$$e_{T0}(t) = \prod\left(\frac{t}{T_e M} - \frac{1}{2}\right) e_{\text{periodic}}\left(t, T_e\right) = \begin{cases} e_{\text{periodic}}\left(t, T_e\right), & 0 \leq t \leq T_e M \\ 0, & \text{otherwise} \end{cases} \tag{2.25}$$

The PW driving waveform can then be synthesized as a combination of time-shifted basis functions:

$$e_{T,PW}\left(t\right) = \sum_{n=0}^{\infty} e_{T0}\left(t - nT_{PRP}\right) \tag{2.26}$$

where n corresponds to the pulse repetition number and T_{PRP} is the pulse repetition period. A meaningful parameter often used to characterize pulsed operation is the pulse repetition frequency $f_{PRF} = 1/T_{PRP}$.

A notional PW transmit excitation waveform $e_T\left(t\right)$ is shown in Figure 2-3, where waveform labels $e_{Tn}\left(t\right)$ indicate the nonzero segment of each time-shifted representation of the basis function.

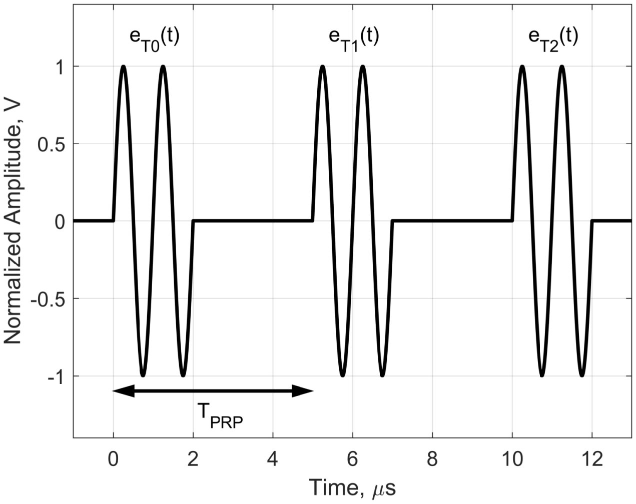

Figure 2-3: Pulsed wave excitation waveform ($M = 2$, $T_e = 1.0\mu$s, and $T_{PRP} = 5\mu$s).

Note that an artificially low T_{PRP} is used for illustration clarity. A realistic pulse repetition period is typically $T_{PRP} \approx 0.1 - 0.2$ms for medical ultrasound applications.

The windowing function $\prod\left(\frac{t}{T_e M} - \frac{1}{2}\right)$ is fairly narrow in time. Therefore, PW transmit excitation $e_T(t)$ has considerable half-power bandwidth $BW_{T,3dB}$:

$$BW_{T,3dB} = \frac{f_e}{M} \tag{2.27}$$

The frequency spectrum of a realistic PW excitation waveform $e_T(t)$ is given in Figure 2-4. The spectral content of $e_T(t)$ is characterized by a main tone at the excitation frequency f_e. Secondary tones occur at integer offsets of the pulse repetition frequency f_{PRF} from the main tone and are shaped by the transmit excitation bandwidth $BW_{T,3dB}$:

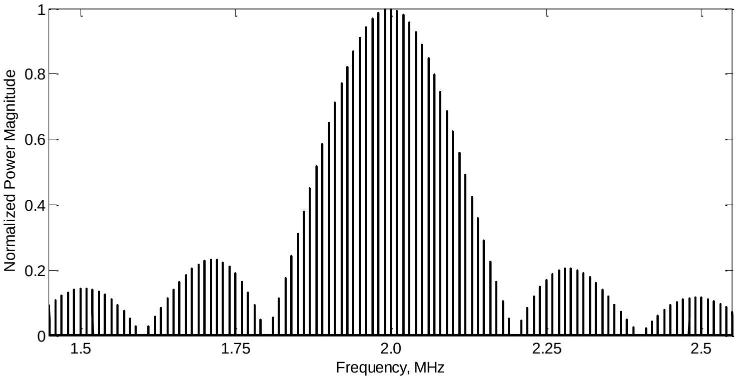

Figure 2-4: Notional pulsed transmit excitation spectrum for $M = 10$, $T_e = 0.5\mu$s, and $T_{PRP} = 0.1$ms [6].

2.2 Phased Array Beamforming

Phased array beamformation is based on the coherent summation of related waveforms. An acoustic beam pattern can be electronically formed through the control of time delays and amplitude scale factors for each element in the transducer array. Beamformation is comprised of beam steering (i.e., modification of main beam direction, referred to as the steering angle) and beam focusing (i.e., convergence of main beam energy at a particular depth, referred to as the focal length). Phased array beamformation is achieved during both pulse transmit and echo receive, creating an effective pulse-echo spatial impulse response expressed as $h_{PE}(\vec{r}, t) = h_R(\vec{r}, t) \underset{t}{*} h_T(\vec{r}, t)$, described in Section 2.3.2 [6].

In transmit beamforming, the excitation pulse for each element is a time-delayed version of the periodic basis function, defined by the transmit beamformer. Excitation amplitude scaling can also often applied to realize apodization of the transmit aperture. Due to the added hardware complexity of implementing amplitude scaling, beamformer apodization is not examined in this work. Following transduction, the delayed acoustic waveforms define a surface within the propagating media of approximately equal phase near the transducer elements, known as the equiphase surface. For a single element transducer, the transducer surface – driven by a common excitation – forms the equiphase surface. A phased array beam pattern is therefore comparable to the beam pattern of a single element transducer defined by the equiphase surface. The planar component of the equiphase surface determines the steering angle (i.e., beam steering), while surface curvature defines the focal length (i.e., beam focusing). The process of transmit beamformation is presented in Figure 2-5.

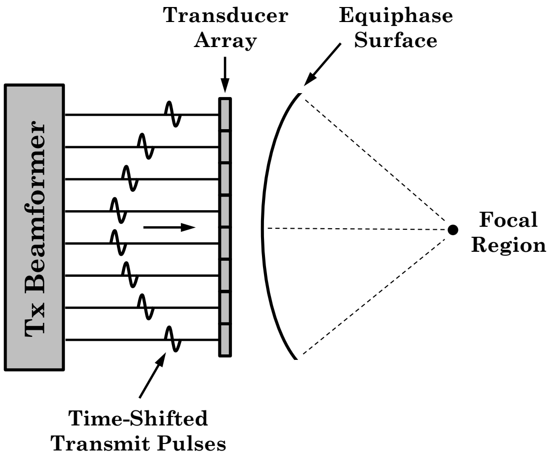

Figure 2-5: Transmit phased array beamformation [6].

Similarly, receive beamformation is achieved through control of time delays and amplitude scaling defined by the receive beamformer. However, because receive waveforms are manipulated subsequent to transduction, receive beamformer designs are less restricted by implementation constraints – such as interfacing with high-voltage pulse signals – and are therefore often more configurable.

Electronic beamformation is utilized in this work for the primary functions of:

- Steering main beam energy for localization of the vessel of interest.
- Increasing acoustic intensity – for a given acoustic output power – at the vessel of interest via focusing, thereby potentially improving acoustic window patency.

The coordinate framework for basic analysis of phased array beam steering and aperture focusing in a homogeneous acoustic medium is presented in Figure 2-6.

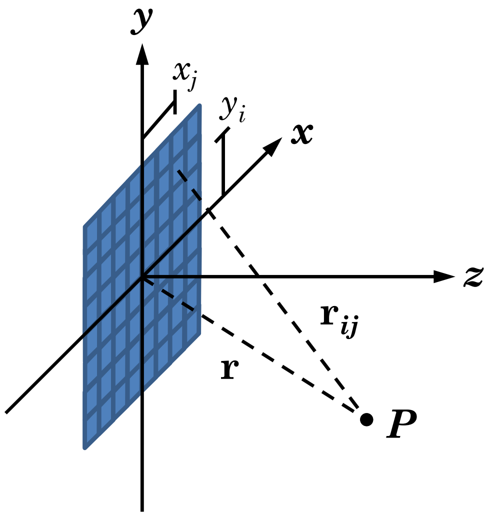

Figure 2-6: Coordinate system for analysis of electronic phased array beam steering and focusing [6].

To achieve beam steering along the $\vec{r}$ direction with a focal region at point P, the time delay required for a transducer element in the i^{th} row and j^{th} column – denoted $\Delta t_{i,j}$ – is expressed as:

$$\Delta t_{i,j} = \frac{r - r_{i,j}}{c} + t_0 = \frac{r - \sqrt{(r_x - x_j)^2 + (r_y - y_i)^2 + r_z^2}}{c} + t_0 \tag{2.28}$$

where $r = |\vec{r}| = |\,(r_x, r_y, r_z)\,|$, t_0 is a constant delay term ensuring causality (i.e., $\Delta t_{i,j} \geq 0 \; \forall \; i, j$), and x_j and y_i are the element center offsets from the origin in the x and y dimensions, respectively. Effects due to transducer element dimensions – particularly grating lobe generation and element directivity – are discussed in Section 2.3.3.

Tissue inhomogeneities act to distort the focal region, leading to spreading of acoustic energy and reductions in focal intensities. The phased array beam steering expression described in Equation 2.28 assumes a homogeneous medium and thus a constant propagation velocity c. Because propagation velocity is relatively constant in a variety of soft tissue types, this assumption yields tolerable effects in most medical ultrasound applications. As presented in Table 2.1, the propagation velocity through cranial bone, however, is markedly distinct from soft tissue.

For transcranial sonography applications, differences in path length through bone, due to skull thickness variations across the aperture and differences in $\vec{r_{ij}}$ angle, cause diminished coherence at the focal region – a phenomena referred to as focal aberration. Differences in acoustic propagation velocity at the interface between bone and soft tissue yield refraction effects, as discussed in Section 2.1.1, which alters wave direction and thereby produces beam pattern distortions [28]. Such nonidealities – in addition to significant signal attenuation – are a primary reason for poor image quality in transcranial ultrasound imaging modalities – including TCCS [6].

By adjusting timing delays, beam pattern distortion effects can be mitigated and the focal region restored to its intended position. Such methods, referred to as phase correction techniques, cannot generally be achieved using physical focusing mechanisms (e.g., curved transducer surfaces, lenses) – due to inadequate reconfigurability and mechanical realizability – and are thereby exclusive to phased array apertures [6]. Phase correction techniques are discussed further in Section 4.4.

2.3 Transducer Beam Patterns

An in-depth anaylsis of acoustic transducer beam patterns is presented in [34]. This work restricts its approach to rectangular geometries, due to their ubiquity in transducer arrays. Subsequent analyses are generally relevant to both transducer elements and to the equivalent transducer array apertures such elements comprise.

Transducer radiation patterns will first be developed for continuous excitations and later extended to pulsed wave fields. Although pulsed operation yields excitation dependent beam patterns, CW analysis can provide a practical starting point for transducer design since general approximate relationships between aperture dimensions and energy boundaries typically persist in the numerical evaluation of pulsed beam patterns.

2.3.1 Continuous Wave Beam Patterns

The beam pattern of a rectangular transducer is determined by two orthogonal dimensions, transducer width (L_x) and height (L_y). Under continuous excitation, the pressure field envelope of a rectangular transducer for observation points along the axial dimension is expressed as [32]:

$$p_{env}\left(z\right) = \left|2Zu_0\mathrm{Im}\left\{F\left(\frac{L_x}{\sqrt{2\lambda}}\right)F\left(\frac{L_y}{\sqrt{2\lambda}}\right)\right\}\right| \tag{2.29}$$

where $F\left(x\right)$ is the Fresnel integral, given by $F\left(x\right) = \int_0^x e^{-\jmath\pi t^2/2}dt$.

Due to diminished symmetry of rectangular elements, modulation of the near-field pressure envelope is moderate, as illustrated in Figure 2-7.

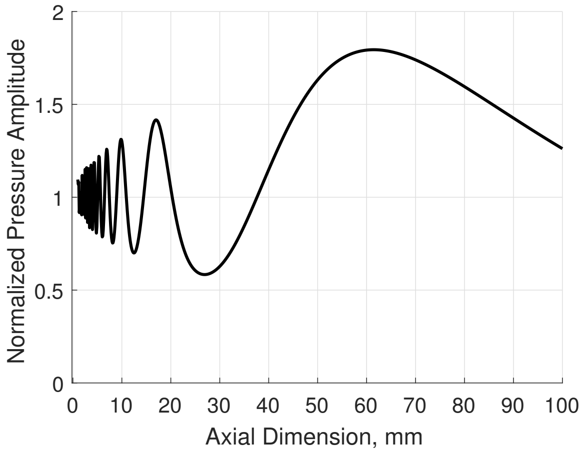

Figure 2-7: Analytical variation of on-axis pressure envelope for a rectangular transducer (L_x = 12mm, L_y = 12mm) operating at 2MHz. Values are normalized to the pressure magnitude at the transducer surface.

Figure 2-8 characterizes the simulated single frequency beam pattern in a lossless, homogeneous medium for a rectangular transducer in the xz and xy-planes [29, 30].

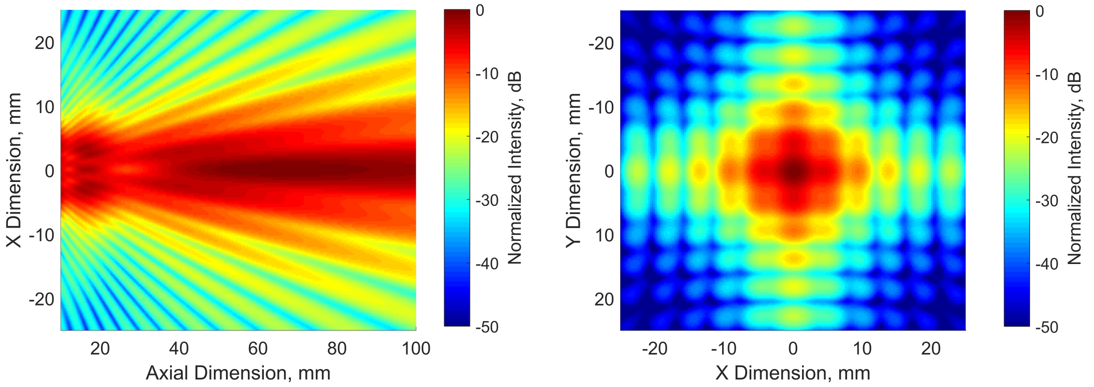

(a) Intensity variation in the xz-plane at $y = 0$mm.

(b) Intensity variation in the xy-plane at $z = 60$mm.

Figure 2-8: Simulated intensity beam pattern for a rectangular transducer ($L_x = 12$mm, $L_y = 12$mm) operating at 2MHz.

Far-Field Region

For unfocused planar transducers, the progression from the near-field (i.e., Fresnel region) to the far-field (i.e., Fraunhofer region) occurs at the transition distance z_r, referred to as the natural focus of the transducer [34].

$$z_r = \frac{\max\left\{l_t\right\}^2}{4\lambda} \tag{2.30}$$

where $\max\left\{l_t\right\}$ is the largest dimension of the transducer surface (e.g., diameter of a circular transducer). Note that because a single acoustic wavelength is used, CW excitation is implied.

Within the near-field region of an unfocused transducer, acoustic energy is mostly confined to the transverse extent of the transducer. As the beam propagates into the far-field, a single main lobe is established and acoustic energy diverges transversely with approximately constant angle, known as the divergence half-angle θ_d, as depicted in Figure 2-9.

The divergence angle ($2\theta_d$) and half-power angle ($2\theta_{3dB}$) can be determined from the main lobe characteristics. The half-power angle, known also as the angular full width to half maximum (FWHM), is defined as the angle between the half-power

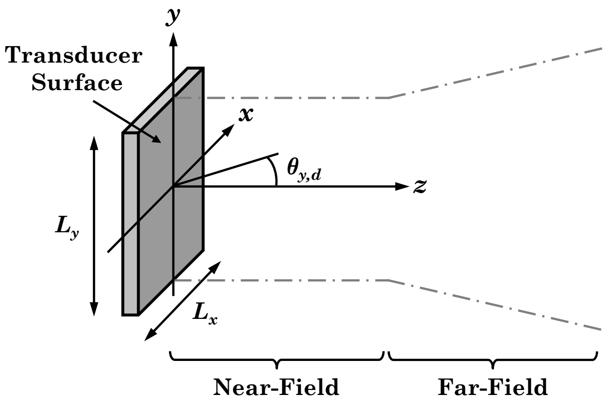

Figure 2-9: Approximate beam shape and far-field divergence for an unfocused transducer. Adapted from [6,34].

values of the main lobe. For the rectangular transducer these parameters exist for both orthogonal directivity planes.

$$2\theta_{x,d} = 2\sin^{-1}\left(\frac{\lambda}{L_x}\right), \quad 2\theta_{y,d} = 2\sin^{-1}\left(\frac{\lambda}{L_y}\right) \tag{2.31}$$

$$2\theta_{x,3dB} = 2\sin^{-1}\left(\frac{0.44\lambda}{L_x}\right), \quad 2\theta_{y,3dB} = 2\sin^{-1}\left(\frac{0.44\lambda}{L_y}\right) \tag{2.32}$$

Main lobe beamwidth $w(z)$ and half-power beamwidth $w_{3dB}(z)$ can be computed for a given far-field depth z:

$$w_x(z) = 2z\tan(\theta_{x,d}), \quad w_y(z) = 2z\tan(\theta_{y,d}) \tag{2.33}$$

$$w_{x,3dB}(z) = 2z\tan(\theta_{x,3dB}), \quad w_{y,3dB}(z) = 2z\tan(\theta_{y,3dB}) \tag{2.34}$$

At observation points in the far-field of the transducer, the acoustic waveform is less irregular and the off-axis beam pattern can be expressed analytically. For a sinusoidally driven rectangular transducer of width L_x and height L_y, acoustic pressure in the far-field is computed as [34]:

$$p(\phi_x, \phi_y, r, t) = \frac{L_x L_y k Z u_0}{2\pi r}\cos\left(2\pi f t - kr + \frac{\pi}{2}\right)\operatorname{sinc}\left(\frac{L_x k \sin\phi_x}{2\pi}\right)\operatorname{sinc}\left(\frac{L_y k \sin\phi_y}{2\pi}\right) \tag{2.35}$$

where the sinc function is defined as:

$$\operatorname{sinc}(x) = \frac{\sin(\pi x)}{\pi x} \tag{2.36}$$

As illustrated in Figure 2-10, the azimuth angle ϕ_x is the angle between the z-axis and the projection of $\vec{r}$ on the xz-plane. The elevation angle ϕ_y is the angle between the z-axis and the projection of $\vec{r}$ in the yz-plane.

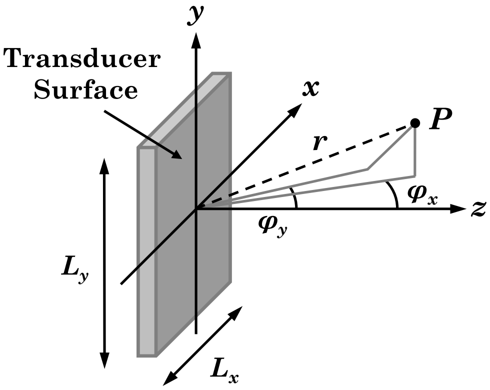

Figure 2-10: Coordinate system for analysis of planar rectangular transducer beam patterns [6].

From Equation 2.35, the angular dependence of acoustic pressure is determined by the transducer directivity factor $H_r(\phi_x, \phi_y)$, which is dependent on directivity in two orthogonal planes, the xz-plane (i.e., azimuth plane) and the yz-plane (i.e., elevation plane) [6]:

$$H_r(\phi_x, \phi_y) = H_x H_y = \left|\operatorname{sinc}\left(\frac{L_x k \sin\phi_x}{2\pi}\right)\right| \left|\operatorname{sinc}\left(\frac{L_y k \sin\phi_y}{2\pi}\right)\right| \tag{2.37}$$

For a given observation radius (i.e., fixed r), the directivity factor is often visually represented using a polar radiation plot, existing for both the azimuth plane, primarily dependent on L_x dimension, and the elevation plane, primarily dependent on L_y dimension. Figure 2-11 shows the directivity of a square transducer element, which has an equivalent directivity pattern in both the azimuth (i.e., H_x) and elevation (i.e., H_y) planes due to transducer symmetry.

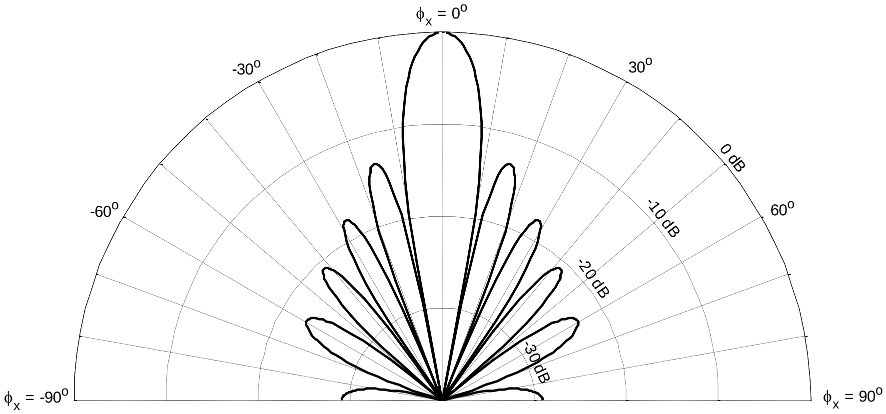

Figure 2-11: Analytical far-field directivity pattern in the azimuth plane for square transducer ($L_x = L_y = 4$mm) operating at 2MHz [6].

Focused Transducers

Acoustic focusing, which converges a radiating beam into a spot at the focal plane, is often employed in medical ultrasound to improve lateral resolution and increase the maximum attainable intensity for a given driving signal amplitude. Focusing is physically realized by a lens or curved transducer surface. In transducer arrays, focusing is achieved by time (or phase) shifting the waveform associated with each transducer element to produce an equivalent lens. Figure 2-12 depicts the approximate extent of appreciable acoustic energy in a notional focused transducer, where l_f is focal length and w_x and w_y are the beamwidths – also referred to as spot widths – in the x and y dimensions, respectively.

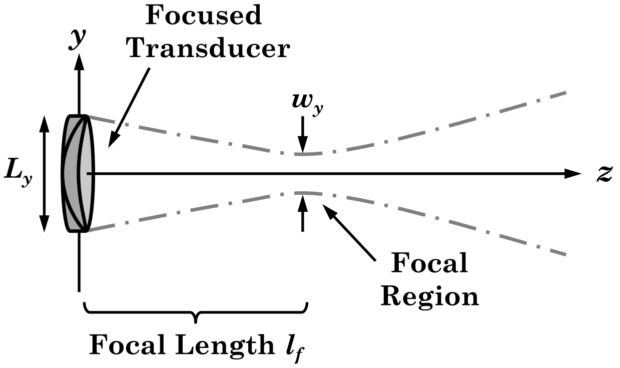

Figure 2-12: Approximate beam shaped of a focused transducer. Adapted from [6,34].

It is convention to define l_f as the length at which the beam intensity is maximal (i.e., acoustic focus), which can differ from geometric focal length (l_R). Pressure amplitude at the acoustic focus moderately exceeds pressure amplitude at the geometric focus, with the acoustic focus always occuring closer to the source [38].

Focal gain (G_f) characterizes the extent of focusing, yielding the ratio of pressure amplitude at the geometric focus to the pressure amplitude at the aperture surface. At shallow focal depths, focal gain increases significantly – as presented in Equation 2.38:

$$G_f = \frac{p_{env}(l_R)}{p_{env}(0)} \approx \frac{z_R}{l_R} \tag{2.38}$$

Weak to moderate degrees of focusing, yielding $1 \lesssim G_F \lesssim 6$, are assumed throughout this text.

Acoustic energy cannot be focused beyond an aperture dependent maximum focal length $l_{f,\max}$ [34]:

$$l_{f,\max} = \frac{\max\{l_t\}^2}{2.44\lambda} \approx z_R \tag{2.39}$$

Therefore, to achieve focusing for greater insonation depths, a larger transducer aperture must be employed.

At the focal plane, the focused spot width (i.e., lateral distance between main lobe nulls) of a rectangular aperture is determined for each lateral axis:

$$w_x = \frac{2\lambda l_f}{L_x}, \;\; w_y = \frac{2\lambda l_f}{L_y} \tag{2.40}$$

The minimum lateral spacing at which two point scatterers are resolvable, known as lateral resolution (LR), is reasonably estimated by spot width.

Focused half-power spot width is expressed for the rectangular transducer as:

$$w_{x,3dB} = \frac{0.88\lambda l_f}{L_x}, \;\; w_{y,3dB} = \frac{0.88\lambda l_f}{L_y} \tag{2.41}$$

For simplicity, acoustic intensity within the half-power spot width is often assumed to be relatively uniform.

Pressure amplitudes near the focal region decrease more rapidly than pressure amplitudes near the axial maximum of the unfocused transducer. The axial distance over which the beam remains focused is known as the depth of focus l_{dof}. As energy becomes more concentrated in the lateral dimensions (i.e., smaller spot width), depth of focus decreases. Under non-radially symmetric aperture geometries, the relationship between l_{dof} and transducer dimensions is not straight, but is primarily influenced by the largest transducer dimension. For a square aperture, depth of focus can be approximated as [34]:

$$l_{dof} \approx \frac{w_x^2}{2\lambda} \tag{2.42}$$

Narrow depth of focus is a critical limitation of fixed focus sonography systems. Focusing is highly advantageous in TCD systems due to considerable increases in local pressure amplitude at the region of interest. TCD sonography, however, requires velocimetry measurements over a wide range of insonation depths ($\approx 30 - 80$mm), which is well beyond the depth of focus for a single transducer element. Phased array architectures, however, enable electronically adjustable focal length and are therefore suitable for focused TCD sonography [6].

2.3.2 Pulsed Wave Beam Patterns

Classical treatment of acoustic fields is based on continuous wave solutions. Although analytical beam pattern expressions from CW derivations are useful in obtaining insight into PW functionality, such results do not yield a precise description of PW beam pattern formation – especially for pulse durations when $M < 6$ [38]. Because pulsed operation is achieved through time gating, time domain expressions are amenable for PW analysis.

A widely used method, first developed by Tupholme and Stepanishen and further refined by Jensen, employs the transducer spatial impulse response to compute radiation patterns for an arbitrary excitation waveform [44–46]. Assuming an infinite rigid transducer baffle and a homogeneous propagating medium, the pressure variation at point P is expressed by a general form of the Rayleigh integral [33]:

$$p\left(\vec{r},t\right)=\frac{\rho_0}{2\pi}\int_{\mathrm{S}}\frac{\frac{\partial u}{\partial t}\left(\vec{r_s},t-\frac{|\vec{r}\,'|}{c}\right)}{|\vec{r}\,'|}dS \tag{2.43}$$

where S denotes the transducer surface and $u\left(\vec{r_s},t\right)$ is the time dependent velocity normal to the transducer surface at dS (i.e., $\vec{r_s}$ is a vector from the origin to dS).

Separation of the transducer spatial impulse response $h\left(\vec{r},t\right)$, which characterizes the three-dimensional field due to impulse excitation, from the Rayleigh integral is used to facilitate radiation pattern calculations. Assuming uniform velocity across the transducer surface, $h\left(\vec{r},t\right)$ can be expressed as [46]:

$$h\left(\vec{r},t\right)=\int_{\mathrm{S}}\frac{\delta\left(t-\frac{|\vec{r}\,'|}{c}\right)}{2\pi\left|\vec{r}\,'\right|}dS \tag{2.44}$$

where $\delta\left(\cdot\right)$ denotes the Dirac delta function. Effects due to attenuation and non-uniform surface velocity – caused by media absorption and apodization, respectively – can be incorporated into this analysis framework through direct modification of the spatial impulse response.

For transducer arrays, an equivalent spatial impulse response $h_{\mathrm{array}}\left(\vec{r},t\right)$ is defined by combining the spatial impulse responses of individual transducer elements:

$$h_{\mathrm{array}}\left(\vec{r},t\right)=\sum_{n=1}^{N}h_n\left(\vec{r}_n,t_n\right)=\sum_{n=1}^{N}h_{\mathrm{el}}\left(\vec{r}-\vec{r}_{\mathrm{offset},n},t-t_{\mathrm{delay},n}\right) \tag{2.45}$$

where $h_{\mathrm{el}}\left(\vec{r},t\right)$ is the spatial impulse response for an element at the origin, N is the number of array elements, $\vec{r}_{\mathrm{offset},n}$ is a vector from the origin to the n^{th} transducer element center, and $t_{\mathrm{delay},n}$ is the excitation delay for the n^{th} transducer element. Equation 2.45 assumes equivalent transducer elements and simple time delays between element excitations [6].

Because the spatial impulse technique separates transducer geometry effects from the excitation waveform, modifications to the driving signal – such as timing delays in phased array systems – do not require repeated integration to determine $h\left(\vec{r},t\right)$

and therefore often result in more efficient computation. The resultant pressure field for a given excitation is expressed as [46]:

$$p\left(\vec{r},t\right) = \rho_0 u\left(t\right) \underset{t}{*} \frac{\partial h\left(\vec{r},t\right)}{\partial t} \tag{2.46}$$

where $\underset{t}{*}$ denotes temporal convolution.

Analytical solutions for the spatial impulse response can be computed for a number of basic transducer geometries, as described in [33, 47]. The method is often solved numerically by field solvers, such as the Field II ultrasound simulator developed by Jensen [29, 30]. Figure 2-13 displays the effect of pulse length on the pulse intensity profile.

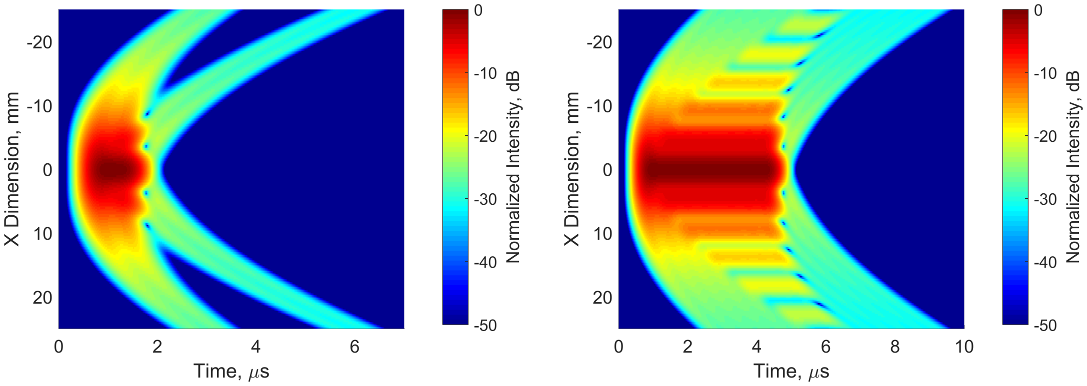

(a) Time dependent intensity variation in the x dimension for $M = 2$

(b) Time dependent intensity variation in the x dimension for $M = 8$

Figure 2-13: Simulated intensity envelope for a rectangular transducer ($L_x = 12$mm, $L_y = 12$mm) operating at 2MHz.

Using the concept of time-average intensity, the beam pattern for pulsed excitation apertures can also be computed using field solvers, as shown in Figure 2-14. Pulsed excitations, as a result of their considerable bandwidth, tend to produce less abrupt beam patterns (i.e., lower spatial derivatives) and lower sidelobe levels than observed in monochromatic CW operation. This effect is most pronounced in the near-field region, where CW operation can lead to high intensity variability. As pulse length expands (i.e., M increases), the resulting field pattern converges to the continuous wave solution [6].

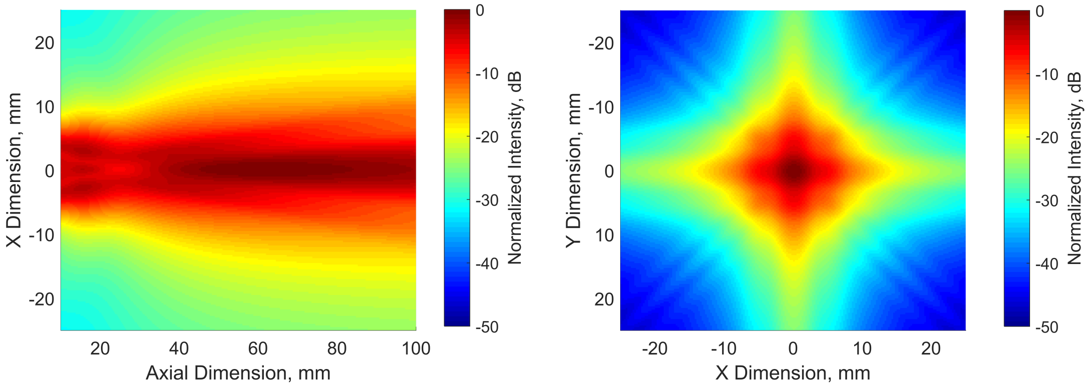

(a) Intensity variation in the xz-plane at $y = 0$mm.

(b) Intensity variation in the xy-plane at $z = 60$mm.

Figure 2-14: Simulated time-average intensity for a rectangular transducer ($L_x = 12$mm, $L_y = 12$mm) operating at 2MHz for M = 2.

2.3.3 Transducer Arrays

Transducer arrays are found in the majority of modern ultrasound imaging systems. The intention of this work is to utilize electronic steering of acoustic energy to accurately locate a specific cerebral vessel (i.e., MCA) within a designated spatial volume. This task necessitates the use of a two-dimensional (2D) transducer array, which will therefore be examined specifically.

A piezoelectric transducer matrix is typically composed of rectangular radiating elements spatially offset by the element pitch in each dimension (pitch_x and pitch_y), as shown in Figure 2-15. Other parameters relevant to the array geometry are the lateral dimensions of individual elements (L_x and L_y), the number of elements along each dimension (N_x and N_y), and the spacing between adjacent element edges (kerf_x and kerf_y).

To first order, a 2D phased array can be estimated as an equivalent mechanically steered aperture with variable focal length. The effective dimensions of this equivalent aperture are approximated as $L_{x,eq} \approx N_x \cdot \text{pitch}_x$ and $L_{y,eq} \approx N_y \cdot \text{pitch}_y$. This analogy is overly simplistic in that electronic steering of the phased array can create focal patterns that are not physically realizable in a focused element. Also, additional complexities are observed in the phased array beam pattern due to the segmentation of the transducer surface into array elements [6].

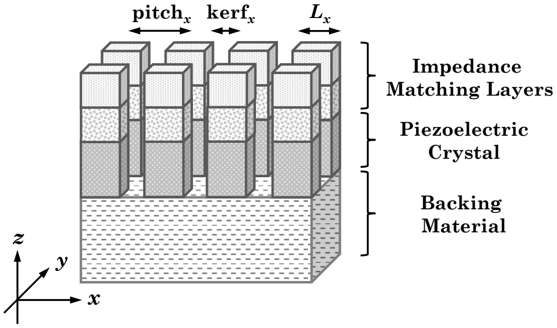

Figure 2-15: Configuration of partial 2D transducer array structure [6].

Unlike single element transducers, array apertures are formed electronically through delay mechanisms rather than by physical form. Such electrically defined apertures are advantageous in that both transmit and receive apertures can be defined independently, aperture characteristics (e.g., steering angle, focal region) can be directly altered, and – for certain system architectures – multiple receive beam patterns can be defined post hoc via post-processing.

A transducer array cannot be accurately analyzed as a coherent set of infinitesimal isotropic radiators, as is done for a single element transducer. Instead, the transducer array is a collection of individual radiating elements with appreciable dimensions, relative to λ, and therefore an anisotropic directivity pattern. The beam pattern of a phased array is dependent on both the relative excitation delay between elements and the radiation pattern of the elements themselves. Figure 2-16 presents the beam patterns of two square array elements with dimensions on the order of λ (i.e., 0.5mm = 0.65λ and 1.2mm = 1.6λ for 2MHz acoustic vibrations in soft tissue).

Although smaller element dimensions yield more favorable element directivity patterns (i.e., approaching isotropic), practical transducer array designs introduce several conflicting aims. As described in Section 2.3.1, aperture dimensions must increase when focusing is required at greater tissue depths.

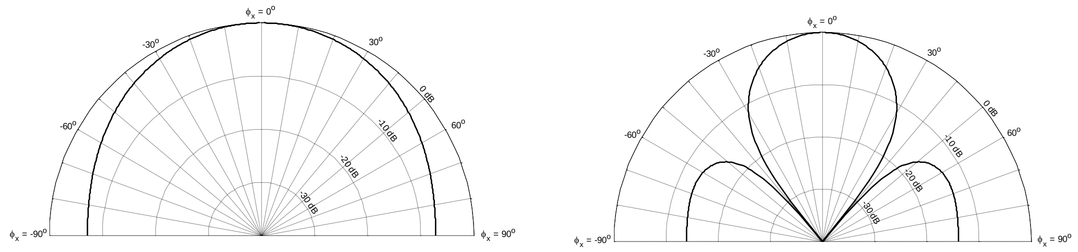

(a) Intensity variation for element with dimensions $L_x = 0.5$mm, $L_y = 0.5$mm.

(b) Intensity variation for element with dimensions $L_x = 1.2$mm, $L_y = 1.2$mm.

Figure 2-16: Analytical far-field directivity pattern in the azimuth plane for a square array element operating at 2MHz.

As individual element dimensions decrease, the total number of elements required to obtain a given aperture area rises quadratically. The corresponding addition of electrical hardware and element interconnects leads to greater fabrication difficulty, system complexity, cost, and power dissipation. However, as transducer element dimensions increase – especially greater than λ – the range of realizable steering angles for the phased array system is limited by element directivity effects [6].

Due to the discrete structure of a transducer array, a variety of secondary factors – including element variation, cross-coupling between elements, and time delay quantization – can influence beam pattern formation. Quantization effects, which tend to predominately affect sidelobe levels, are tolerable in most applications for quantization errors $< 10\%$ of the underlying signal period (i.e., T_e) and can be readily assessed using acoustic field solvers [48]. The result of element variation and electromagnetic cross-coupling between elements, however, is typically assessed using multiphysics finite element analysis (FEA) or through experimental acoustic field characterization.

An added complexity related to the radiation pattern of transducer arrays is the emergence of grating lobes. Grating lobes occur at specific angles in which acoustic waves emerging from two neighboring elements are exactly in phase for a certain angle (referred to as the grating angle), creating constructive interference and substantial acoustic intensity outside the main beam. In ultrasound imaging, the presence of grating lobes leads to confounding receive echoes since acoustic energy is no longer confined along the main beam direction. The presence of grating lobes can also degrade Doppler ultrasound measurements, even when no appreciable flow exists within grating lobes, by markedly increasing stationary backscattered power and thereby degrading the minimum detectable signal for a given system dynamic range. Grating lobes are typically stronger than sidelobes and can yield intensities on the order of main lobe intensities [6]. Grating angle differs for both the azimuth and elevation planes and is given by:

$$\phi_{x,gn} = \sin^{-1}\left(\frac{n\lambda}{\text{pitch}_x} - 1\right) \tag{2.47}$$

$$\theta_{y,gn} = \sin^{-1}\left(\frac{n\lambda}{\text{pitch}_y} - 1\right) \tag{2.48}$$

where n is an integer value, although typically the fundamental (i.e., $n = 1$) is of primary interest. Solutions resulting in $|\phi_{x,gn}| > 90^\circ$ or $|\theta_{y,gn}| > 90^\circ$ are non-physical and therefore invalid.

When allowable steering angle is limited in each dimension, the maximum element pitch required to avoid grating lobe formation is given as:

$$\text{pitch}_{x,\max} = \frac{\lambda}{1 + \sin\left(\phi_{x,\max}\right)} \tag{2.49}$$

$$\text{pitch}_{y,\max} = \frac{\lambda}{1 + \sin\left(\theta_{y,\max}\right)} \tag{2.50}$$

To avoid grating lobe formation for all physical steering angles – that is, $|\phi_x| \leq 90^\circ$ and $|\theta_y| \leq 90^\circ$ – element pitch must satisfy the following conditions:

$$\text{pitch}_x < \frac{\lambda_{\text{min}}}{2}, \ \text{pitch}_y < \frac{\lambda_{\text{min}}}{2} \tag{2.51}$$

where, due to an inverse relationship between wavelength and frequency, λ_{min} corresponds to the highest frequency component in the emitted signal. The preceding inequality can be viewed as a consequence of the Nyquist sampling theorem in the spatial domain, where the presence of grating lobes are an indication spatial aliasing. Grating lobe effects can be reduced through PW excitation and for angles that occur beyond the element directivity main lobe.

2.4 Pulse-Echo Operation

The spatial impulse response method developed in Section 2.3.2 can be extended to analysis of pulse-echo processes for point scattering. Figure 2-17 presents the fundamental elements of pulse-echo operation.

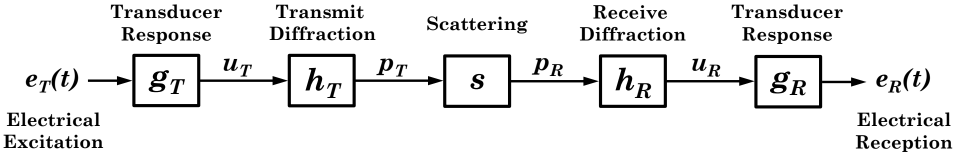

Figure 2-17: Block diagram representation of an acoustic pulse-echo process. Adapted from [6, 47].

During transmission, the electrical excitation signal $e_T(t)$ yields a transmit velocity $u_T(t)$ at the transducer surface. Using the transmit electroacoustic conversion impulse response $g_T(t)$, transmit surface velocity is expressed as:

$$u_T(t) = e_T(t) \underset{t}{*} g_T(t) \tag{2.52}$$

The transmit (i.e., incident) pressure field $p_T(\vec{r}, t)$ can thereby be computed as:

$$p_T(\vec{r}, t) = \rho_0 u_T(t) \underset{t}{*} \frac{\partial h_T(\vec{r}, t)}{\partial t} = \rho_0 e_T(t) \underset{t}{*} g_T(t) \underset{t}{*} \frac{\partial h_T(\vec{r}, t)}{\partial t} \tag{2.53}$$

where $h_T(\vec{r}, t)$ is the transmit aperture spatial impulse response.

Inhomogeneities are treated as point scatterers using the scattering field function $s(\vec{r})$ [33]:

$$s(\vec{r}) = \frac{\Delta\rho(\vec{r})}{\rho_0} - 2\frac{\Delta c(\vec{r})}{c_0} \tag{2.54}$$

where ρ_0 and c_0 are the average density and velocity of propagation within the medium, respectively. Functions $\Delta\rho(\vec{r})$ and $\Delta c(\vec{r})$ contain perturbations in acoustic properties and thereby produce scattering.

For a finite number of point scatterers ($N_{\text{scatterers}}$), functions $\Delta\rho\left(\vec{r}\right)$ and $\Delta c\left(\vec{r}\right)$ are expressed as:

$$\Delta\rho\left(\vec{r}\right) = \sum_{n=1}^{N_{\text{scatterers}}} \left(\rho_n - \rho_0\right)\delta\left(\vec{r} - \vec{r}_n\right) \tag{2.55}$$

$$\Delta c\left(\vec{r}\right) = \sum_{n=1}^{N_{\text{scatterers}}} \left(c_n - c_0\right)\delta\left(\vec{r} - \vec{r}_n\right) \tag{2.56}$$

where ρ_n and c_n indicate the density and acoustic velocity of perturbations (i.e., discrete scatterers), respectively, and $\vec{r}_n$ denotes the position vector of the n^{th} scatterer with respect to transducer origin [6].

The electrical receive signal $e_R\left(t\right)$ can thereby be computed completely in terms of the electrical excitation, transducer impulse responses, aperture spatial impulse responses, and the scattering field function. Assuming coincident transmit and receive apertures – such that the origin remains common – $e_R\left(t\right)$ is expressed as [32, 46]:

$$e_R\left(t\right) = \frac{1}{c_0^2} e_T\left(t\right) \underset{t}{*} g_T\left(t\right) \underset{t}{*} g_R\left(t\right) \underset{t}{*} \frac{\partial h_T\left(\vec{r}, t\right)}{\partial t} \underset{t}{*} \frac{\partial h_R\left(\vec{r}, t\right)}{\partial t} \underset{r}{*} s\left(\vec{r}\right) \tag{2.57}$$

where $h_R\left(\vec{r}, t\right)$ is the receive aperture spatial impulse response and $g_R\left(t\right)$ is the receive electroacoustic conversion impulse response, which is necessary to convert between receive velocity $u_R\left(t\right)$ and the receive voltage waveform $e_R\left(t\right)$:

$$e_R\left(t\right) = u_R\left(t\right) \underset{t}{*} g_R\left(t\right) \tag{2.58}$$

Transmit and receive electroacoustic conversion impulse responses – denoted $g_T\left(t\right)$ and $g_R\left(t\right)$, respectively – can be determined from equivalent circuit transducer models, as discussed in Section 6.1.

The preceding analysis of pulse-echo operation assumes linearity, time-invariance, and point single scattering (i.e., scattering at discrete points due solely to incident radiation). This method can, in principal, be modified to account for anisotropic point scattering via the differential scattering cross-section $\sigma_{ds}(\theta)$, as discussed in Section 2.1.1. Bulk inhomogeneities, however, cannot be modeled under the previous formulation and require alternative approaches, such as finite-difference time-domain

(FDTD) methods, and FEA methods [31,49].

2.5 Summary

This chapter introduces basic principles of acoustic theory – including propagation, attenuation, and scattering. Descriptions of pulsed wave operation and transducer element beam patterns are also detailed. From these fundamental concepts, analysis of transducer arrays and phased array beamformation is presented. Lastly, the interaction of these various physical factors on system pulse-echo operation is examined. The resulting analytical framework is employed throughout this thesis in the design and quantitative evaluation of diagnostic ultrasound instrumentation.

Chapter 3

Transcranial Velocimetry Constraints

3.1 Anatomical and Physiological Considerations

3.1.1 Cerebrovasculature

Brain tissue is fundamentally reliant on uninterrupted and sufficient oxygenation. Blood flow requirements for the brain, relative to other organs, are considerable. Under resting conditions, the brain accounts for almost 20% of bodily oxygen demands [50, 51]. The cerebrovascular anatomy is composed of multiple redundancies, known as collaterals, such that adequate perfusion can many times be maintained in the event of inadequate flow through a single vascular route (e.g., due to blockage or stenosis) [52].

The main anatomical structure of the cerebrovasculature is the Circle of Willis, as depicted in Figure 3-1. The Circle of Willis is composed of the left and right branch pairs of the anterior cerebral artery (ACA), terminal internal carotid artery (TICA), posterior cerebral artery (PCA), posterior communicating artery (PCoA), middle cerebral artery (MCA), and the non-paired anterior communicating artery (ACoA), and basilar artery (BA). The TICA is the distal segment of the supraclinoid internal carotid artery (ICA) just proximal to its bifurcation into the ACA and MCA. For each cerebral hemisphere, under standard anatomic and non-pathological conditions, the MCA and ACA are supplied by the ipsilateral ICA. The left and right PCAs are supplied by the BA and flow through the communicating vessels (i.e., ACoA and PCoA) is generally minimal. Abnormalities in the anatomy of the cerebral vessels is, however, extremely common and considerable [6].

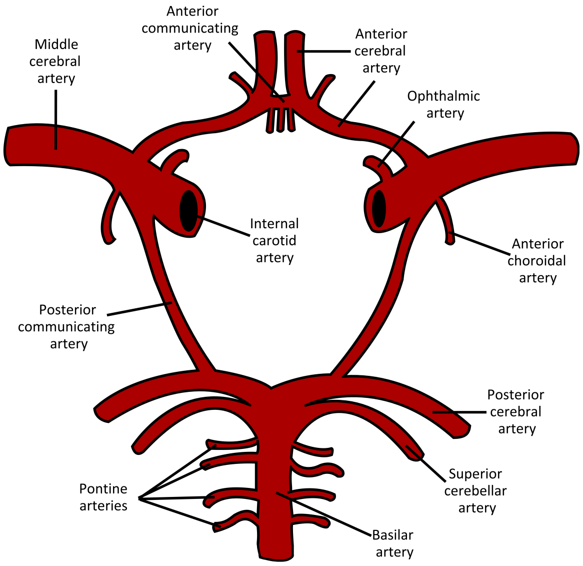

Figure 3-1: Anatomical structure of the cerebrovasculature. Adapted from [6, 53, 54].

Anatomic variation – including vessel caliber, course, and origin – and knowledge of the most frequent deviations – must be recognized when identifying vessels during TCD evaluation. Aspects of vessel identification are summarized for the major intracranial vessels in [12, 55]. The reliability of vessel identification techniques varies among the intracranial vessels, with the highest accuracy of identification occurring for the ipsilateral MCA.

The left and right MCAs – the primary vessels of interest for this work – supply blood to the lateral surface of each cerebral hemisphere and carry the vast majority of blood leaving the Circle of Willis ($\approx 80\%$) [56]. From its origin as a continuation of the left or right TICA, the ipsilateral MCA courses laterally (i.e., away from the cerebral midline) and slightly anteriorly [55]. The proximal portion of the MCA, known as the M1 or sphenoidal segment, gives rise to numerous small lenticulostriate perforators and has a normal mean diameter of 2.5 to 3.8mm [57, 58]. The distal M1 segment furcates – typically a bi- or trifurcation – into the MCA M2 branches, which course 90° superiorly and posteriorly into the Sylvian fissure [6, 55].

The MCA – along with its branches – is normally the only vessel perceptible from the TAW using TCD sonography between insonation depths of 25 to 50mm [12]. Flow direction of the ipsilateral MCA is generally toward the transducer, which is also observed for the PCA. To distinguish the MCA from the PCA, it is useful to trace the MCA extent with increasing depth to the TICA bifurcation, which is identified by bidirectional flow at an insonation depth of 55 to 65mm. MCA flow velocities are typically slightly larger than those obtained at the ACA and are generally at least 25% larger than PCA flow velocities. Finally, upon compression of the ipsilateral common carotid artery under normal cerebrovascular anatomy, flow in the MCA and ACA is temporarily obliterated or severely diminished while flow in the PCA is relatively unaffected [6].

Cerebral blood flow velocity (CBFV) measurements are generally characterized by a set of clinically relevant parameters, particularly peak systolic velocity (PSV), end diastolic velocity (EDV), and time mean velocity (MV). Time mean velocity carries the highest physiological significance as it most closely correlates with cerebral perfusion. Certain applications of TCD, however, rely on the complete time domain velocity waveform for adequate temporal resolution of cerebral hemodynamics [6]. Flow velocity measurements in TCD sonography are generally referenced to the velocity envelope – corresponding to blood flow velocity in the vessel centerline. Spectral distribution characteristics may also be assessed – particularly during the detection of turbulent flow [55].

TCD examinations commonly include bilateral evaluation. Although the cerebrovasculature is ostensibly similar on either side, moderate differences in velocimetry data for each cerebral hemisphere often occur, especially in the presence of pathology. Differences between the left and right hemispheres should not be considered abnormal unless they exceed 30% [59].

Table 3.1 gives typical dimensions and flow velocity values for the M1 segment of the MCA in adult subjects.

Table 3.1: Summary of normal adult anatomical values and flow velocities for the M1 segment of the MCA [6, 12, 57, 60].

Insonation Depth [mm]	Segment Length [mm]	Diameter [mm]	$\overline{MV} \pm \sigma_{MV}$ [cm/sec]	$\overline{PSV} \pm \sigma_{PSV}$ [cm/sec]	$\overline{EDV} \pm \sigma_{EDV}$ [cm/sec]
30 – 60	16.2	2.5 – 3.8	65 ± 17	94 ± 23	46 ± 12

It is customary to assume that Doppler angle (θ_D) is approximately 0° when performing non-imaging (i.e., "blind") TCD examinations because the exact angle between the ultrasound beam and intracranial vessel segment is unknown. For MCA insonation, θ_D is commonly thought to be moderate. Due to a cosine dependence, $|\theta_D| < 20^\circ$ results in maximum velocity underestimation of $\approx 6\%$. Color flow imaging (CFI) capabilities in transcranial color-coded sonography (TCCS) systems, however, facilitate direct measurement of Doppler angle and thereby enable angle correction of flow velocities.

Validation studies suggest that Doppler angle is generally unpredictable and often significantly larger than conventionally assumed [18, 61, 62]. For transtemporal insonation of the MCA, one study yielded mean Doppler angle of $33^\circ \pm 15^\circ$ resulting in average peak systolic flow velocity underestimation of 15% [61]. A similar study found that angle corrected MCA velocities were 25 to 50% higher than uncorrected values in 20% of subjects and $> 50\%$ higher than uncorrected values in 6.7% of subjects [63].

Such significant discrepancies in CBFV data from single element TCD instrumentation lead to lower diagnostic sensitivity in certain pathologies – compared to TCCS instrumentation [2]. However, angle correction via planar TCCS imaging may still result in underestimation of flow velocity due to the three-dimensional course of intracranial arteries [2].

3.1.2 Cranial Acoustic Windows

Acoustic access to the intracranial cerebral vessels is facilitated by the occurrence of anatomical features – relative thinning of cranial bone or natural foramina – known as cranial acoustic windows [20]. In general, three primary cranial acoustic windows are used in TCD sonography: the transtemporal, transorbital, and transforaminal acoustic windows. Insonation of the MCA is normally accomplished through the transtemporal acoustic window (TAW), which is considered in detail.

The TAW is located near the temple region and exists due to regions of thinning in the suprazygomatic portion of the temporal bone, which allows favorable transmission of acoustic energy at reduced attenuation. Despite the relative thinness of temporal bone within the TAW, considerable signal attenuation does occur, with attenuation extent being largely dependent on bone thickness. A patent TAW allows insonation of the ipsilateral TICA, ACA, MCA, PCA, ACoA, and PCoA under favorable anatomic conditions [64]. The TAW is further subdivided into four regions, known as the posterior, middle, anterior, and frontal temporal acoustic windows, as illustrated in Figure 3-2.

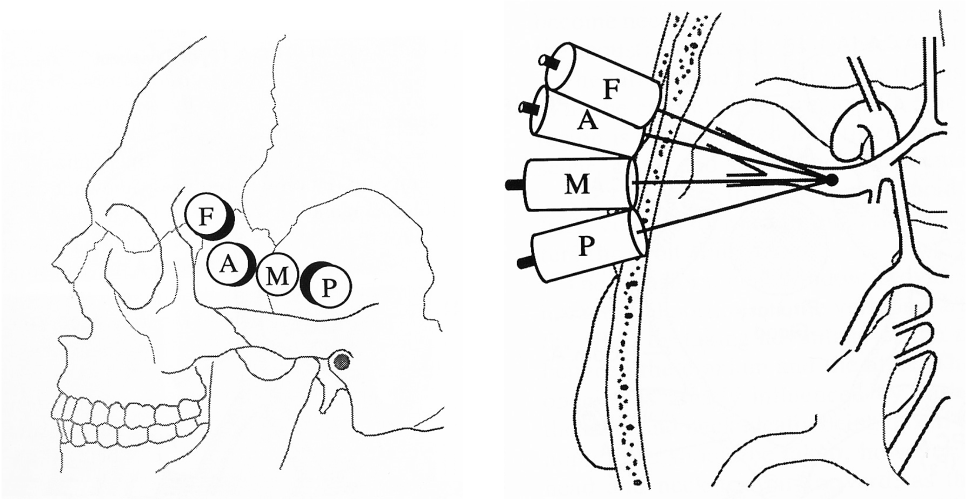

(a) Relative position of the transtemporal acoustic window (sideview).

(b) Window dependent transducer angulation (topview).

Figure 3-2: Depiction of the posterior (P), middle (M), anterior (A), and frontal (F) temporal acoustic window regions. From [55].

Significant variation occurs in the precise location of patent TAW regions, therefore approximate locations as given. The posterior TAW, the TAW region with highest patency rates and the largest spatial separation of the anterior and posterior circulations, lies directly anterior to the external auditory meatus and slightly superior to the zygomatic arch [55]. The anterior TAW is roughly 3cm anterior to the posterior TAW and slightly posterior to the frontal process of the zygomatic bone. A middle TAW is located approximately midway between the posterior and anterior windows. Rarely, a frontal TAW – located just anterior to the pterion – is also used for transtemporal insonation [55]. Patent acoustic window regions are often fairly small and lateral movement of the transducer by a few millimeters can greatly degrade received Doppler signal levels [12]. The middle and anterior TAWs can generally achieve insonation of the MCA with the transducer lying relatively flat against the skin surface. The posterior TAW often requires anterior and superior beam angulation to achieve insonation of the MCA [6].

The transmission of acoustic energy through temporal bone has been studied experimentally by Grolimund in *ex vivo* skulls [12]. Although analytical propagation models are beneficial in understanding opposing design goals within an ultrasound system, experimentation is the only suitable means of obtaining an accurate depiction of tissue propagation losses due to a wide variability in cranial bone properties. The Grolimund experiments employed a 16mm diameter circular transducer operating at 2MHz and used hydrophone measurements to determine receive intensities and beam distortions following transmission through *ex vivo* skulls at the optimal temporal window – defined by the thinnest section of temporal bone. Receive intensities and beam patterns were compared to transmission characteristics in the absence of inhomogeneities (i.e., water medium). The degree of beam distortion due to refraction was shown to depend highly on the variation of thickness within the cranial bone adjacent to the transducer. Due to irregular thickness variations, observed refraction effects cannot be corrected by physical transducer surfaces or lens structures. In the presence of cranial bone, the mean change in intensity of the transmitted acoustic wave at the thinnest temporal bone section was -7dB (i.e., 80% intensity reduction). Pulse-echo operation is therefore expected to attain a reduction on the order of 14 to 20dB in acoustic intensity due to the attenuative, reflective, and refractive effects of cranial bone [6].

A primary obstacle associated with TCD examination is the inability to obtain a detectable received Doppler signal in approximately 5 to 10% of patients due to a lack of patent acoustic window, unusual vessel position, or excessive vessel tortuosity [9, 19]. The absence of a suitable TAW for MCA insonation was observed in 8.2% of individuals in a validation study (occurring in 5.0% of subjects monolaterally and 3.2% of subjects bilaterally) [20]. Lack of a satisfactory TAW is inherently related to increased temporal squama thickness, which has a mean value of 3.5mm at its thinnest region, and is notably more prevalent in non-white races and females (12.1% TAW absence in females, 5.6% TAW absence in males) [6, 65].

TAW patency is further affected by a number of bone pathologies, including hyperostosis, which causes localized increases in cranial bone density and thickness [55]. Age has also been shown to have significant influence on TAW patency, with 5.1% of patients under the age 65 lacking an acceptable TAW, as opposed to 14.1% of patients age 65 and older [20]. Age dependent effectiveness is a major concern for the clinical use of TCD sonography since rates of cerebrovascular related pathologies increase in elderly populations.

Duplex instrumentation (i.e., TCCS) offers several advances to conventional TCD methods – particularly angle correction capabilities and improved operator awareness of anatomical context. However, TCCS is associated with decreased rates of transtemporal patency, further complicating broad acceptance of transcranial sonography methods within the medical community [2, 62].

Ultrasonic contrast agents can be used to improve TAW patency by enhancing the effective scattering coefficient of blood, but invasive administration – requiring intravenous injection – and significantly lower cavitational thresholds thereby complicate the evaluation process and yield additional safety concerns [21, 25]. Increased echogenicity due to administration of contrast agents is dose dependent and limited to short time intervals ($\approx$ 60 to 300s), thereby precluding their use in extended monitoring applications [66, 67]. The use of ultrasonic contrast agents is not considered in this work.

During prolonged TCD monitoring, a headframe can be employed to hold the transducer in position after an acceptable Doppler signal is obtained. Patient movement – or other sources of motion – can cause probe misalignment and a consequent degradation in Doppler signal strength. The frequency of probe displacement effects is highly dependent on measurement application, being more problematic in prolonged evaluation of non-comatose patients. Transducer position and angulation must therefore be regularly optimized to ensure adequate alignment and measurement accuracy [6, 11].

3.2 Acoustic Safety Considerations

Although diagnostic ultrasound is generally considered a low-risk measurement modality, analysis of acoustic bioeffects should be considered to ensure safe and effective use. Various governmental and professional standards, particularly from the United States Food and Drug Administration (FDA), American Institute of Ultrasound in Medicine (AIUM), and British Medical Ultrasound Society (BMUS), have been established to quantify safe operating regimes and thereby limit the potential of patient harm [6, 68–70].

Safety guidelines are particularly meaningful for the continuous TCD monitoring applications of this work, due to prolonged examination duration, high acoustic absorption in bone, and the acoustic output power necessary to achieve adequate insonation of the intracranial vessels. Ultrasound induced bioeffects can be broadly divided into thermal and nonthermal categories. Specific limits exist for each phenomenon and potential for tissue damage is expected only when ultrasound exposure thresholds are exceeded.

Thermal effects (i.e., tissue heating) are related to the conversion of acoustic energy into heat and are therefore dependent on time-average intensity measures and tissue absorption factors. A thermal index is used to predict the rise of tissue temperature in °C under worst case conditions. Due to the presence of cranial bone at the tissue surface, the relevant thermal parameter for transcranial applications is the thermal cranial index (TIC) [25]. Heating of cranial bone due to absorption results in secondary heating of adjacent brain tissue via heat conduction. The AIUM and BMUS recommend limiting $TIC < 2.0$, which is similar to the global TIC limit in commercial TCD systems [6, 71].

TIC is directly related to acoustic power and can be expressed as:

$$TIC = \frac{W_0}{8}\sqrt{\frac{\pi}{A_{ap}}} \tag{3.1}$$

where W_0 is time-average acoustic source power (measured in W) and A_{ap} is the active aperture area (measured in m^2) [6, 25].

Time-average acoustic output power W_0 can be determined for a gated sinusoidal excitation waveform by the expression:

$$W_0 = A_{ap}\frac{p_0^2}{2Z}\frac{MT_e}{T_{PRP}} \tag{3.2}$$

where p_0 is the surface pressure amplitude and Z is the characteristic acoustic impedance of the propagating media.

Nonthermal effects – primarily cavitation (i.e., collapse of gas bubbles within the medium) and acoustic streaming (i.e., steady fluid current due to nonlinear absorption) – are influenced by peak rarefaction pressures within the acoustic field. Nonthermal effects are characterized by the mechanical index (MI), an attempt to indicate the probability of mechanical damage in a nonthermal process, is given by [68]:

$$MI = \frac{p_{rar,\max}}{1000\sqrt{f_e}} \tag{3.3}$$

where $p_{rar,\max}$ is the derated (i.e., accounting for soft tissue attenuation) spatiotemporal peak rarefactional pressure (measured in Pa) and f_e is the excitation frequency (measured in Hz). Safety guidelines suggest, in the absence of ultrasound contrast agents, that $MI < 1.9$ [68]. Using a typical 2MHz excitation frequency, this results in a maximum rarefactional pressure of 2.7MPa (neglecting derating). For most TCD applications, TIC is a more restricting limitation and operational MI values are considerably below their threshold values. Because MI is computed without accounting for the significant attenuating effects of cranial bone, *in situ* MI values can be expected to be considerably reduced in practice [6].

FDA guidelines limit the spatial-peak-temporal-average intensity I_{SPTA} (as defined in Section 2.1) for diagnostic ultrasound uses to $< 720\text{mW/cm}^2$ (for devices following the output display standard) [68]. I_{SPTA} is dependent on spatial-peak pressures – influenced primarily by transducer characteristics, excitation amplitude, and transmit duty cycle (i.e., relative temporal extent of the excitation waveform to the pulse repetition period). In conventional single element TCD systems, I_{SPTA} constraints are not typically a limiting factor for diagnostic operation. Under acoustic focusing – such as phased array operation – focal gain ($G_f > 1$) yields increased peak intensities for a given acoustic output power. Therefore, I_{SPTA} limits may be more constraining than other acoustic safety indices – especially for shallow depths of insonation where focal gain is maximal.

A basis of ultrasound safety is prudent use of the ALARA principle (i.e., "as low as reasonably achievable"). This principle states that acoustic output power should always be the minimal level necessary to achieve adequate diagnostic information. The ALARA principle is utilized in TCD evaluations by the initial use of moderate power levels during cranial window location. If adequate Doppler signals cannot be obtained, the operator increases acoustic output power levels toward their limiting values and repeats the vessel location procedure. In accordance with the ALARA principle, once the optimal cranial window is localized and a sufficient Doppler signal obtained during examination, acoustic output power should be reduced to the minimal level achievable without discernible degradation to Doppler signal fidelity [6].

Current safety index models do not account for duration of exposure. As ultrasound monitoring paradigms shift – especially toward prolonged monitoring capabilities – exposure standards may adapt to account for this modified use cases. Because ultrasound exposure guidelines do not yet exist for extended monitoring, a conservative interpretation of the current standards will instead be accepted. Such interpretation is commiserate with existing commercial TCD systems, which can be used for continuous monitoring [71].

Maximum acoustic index values for the prototype TCD systems developed in this work are given in Table 3.2.

Table 3.2: Prototype TCD system maximum global acoustic indices [6].

Parameter	Accepted Safe Limit	Prototype Device Limit
TIC	< 2.0	< 1.8
MI	< 1.9	< 1.5
I_{SPTA}	< 720 mW/cm^2	< 700 mW/cm^2

3.3 Summary

This chapter introduces several fundamental limitations of CBFV estimation via Doppler sonography methods. First, an overview of the cerebrovasculature is presented – detailing the relevant nominal vessel anatomy and flow velocity parameters. For transtemporal insonation of the MCA, the effect of Doppler angle on measurement accuracy is considered. Second, acoustic propagation through temporal bone and the presence of cranial acoustic windows is examined. Finally, acoustic indices and safety guidelines particular to transcranial operation are discussed; an appropriate set of acoustic limits for prototype hardware is established.

Chapter 4

Algorithm Development

4.1 Pulsed Doppler Operation

In a majority of TCD applications, the true clinical parameter of interest is cerebral blood flow (CBF). Doppler methods, however, yield flow velocities and – due to anatomical constraints – diameter of the cerebral arteries cannot be measured via acoustic means with sufficient accuracy to obtain absolute volumetric flow [55]. Nonetheless, Doppler ultrasound can provide a phenomenal representation of the dynamic progression of *in vivo* blood through the cerebrovasculature, which cannot be acquired from any other noninvasive modality [6].

Although absolute CBF cannot be accurately measured in TCD sonography without reliable vessel dimensions, relative changes in CBFV can be a surrogate marker for CBF variation when changes in vessel lumen diameter are small (or otherwise predictable). The MCA – and other major basal cerebral arteries – serve mainly as conductance channels and are not significantly involved in the active regulation of blood flow. Studies have shown that CBF, measured at the internal carotid artery via electromagnetic flowmetry, and CBFV envelope, measured at the MCA via TCD, are highly correlated for moderate changes in ABP [55, 72].

Certain applications of TCD – notably emboli detection and vasospasm monitoring – do not rely on the assumption of constant vessel diameter, but instead depend on CBFV parameters directly as indications of pathology. Recognition of the underlying assumptions required by specific TCD applications is critical for the proper interpretation of measurement data.

4.1.1 Velocity Estimation for a Single Scatterer

Pulsed wave (PW) operation exploits time encoding of scatterer spatial position. In TCD sonography, exceedingly large amplitude reflections, due to the presence of cranial bone and other axially distant stationary scatterers, can be neglected by time gating the receive signal about the depth of interest and thereby achieving fine axial resolution. Because receiver electronics must simultaneously detect low-level signals from moving scatterers and high-level scattering from stationary tissue, PW operation greatly reduces system dynamic range requirements by eliminating the effect of scatterers outside the sample volume.

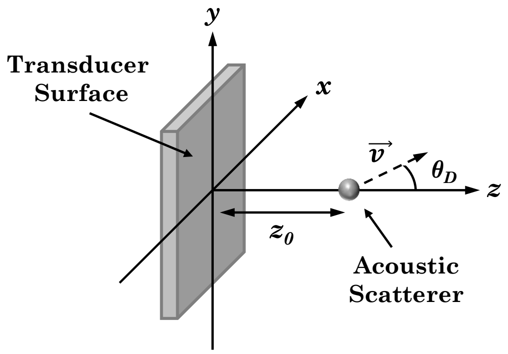

Figure 4-1: Coordinate system for analysis of PW velocity estimation [6].

At a basic level, scatterer velocity is determined by repeated pulse emissions and comparison of received time shifts between adjacent pulses. The PW velocity estimation algorithm is described for a single scatterer within a highly simplified framework and then extended to an ensemble of scatterers. As shown in Figure 4-1, a scatterer starts at depth z_0 – relative to the ultrasound transducer surface – and moves with a constant velocity vector $\vec{v}$, where θ_D is the angle between $\vec{v}$ and the z-axis (i.e., the Doppler angle), $v_z = \vec{v}\cos\theta_D$ represents the velocity component normal to the transducer surface, and the scatterer is assumed to be along or sufficiently near the z-axis (i.e., within the beamwidth of the transducer) [6]. Plane wave propagation of the incident and scattered waveforms is initially assumed for analytical tractability, but later expanded within a realistic acoustic context.

The time-space relationship between a constant velocity scatterer and the periodic transmit waveform is depicted in Figure 4-2.

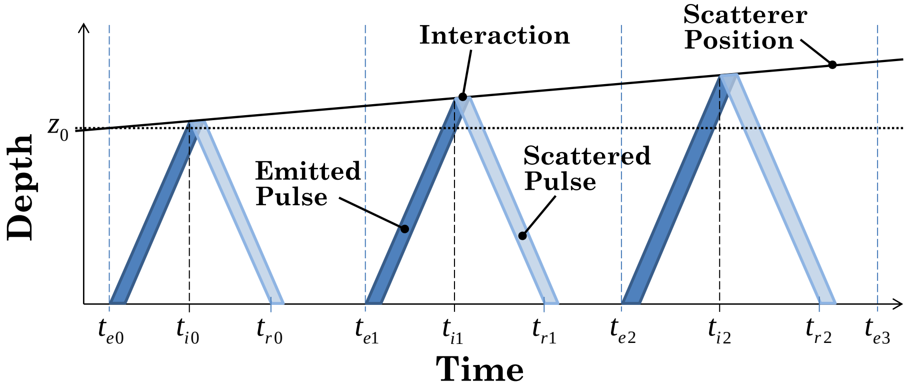

Figure 4-2: Time-space diagram of scatterer and pulse interaction.
Adapted from [6, 33].

In Doppler sonography, M (i.e., number of cycles within the periodic basis function) is typically a moderate value (i.e., $M < 20$) corresponding to a range gate length l_g of several millimeters. Range gate length characterizes the instantaneous extent of insonation depth:

$$l_g = \frac{Mc}{2f_e} \tag{4.1}$$

Sample offset time T_s is defined as the delay between pulse emission and sampling of the electrical receive signal. The sample depth z_s is thereby expressed as:

$$z_s = \frac{T_s c}{2} \tag{4.2}$$

where z_s is selected to correspond to the depth of interest – typically aperture focal length in focused applications.

Sampling of the electrical receive signal $e_R(t)$ at sample offset time T_s is therefore only affected by scatterers contained within the sample volume depth z_{sv}:

$$z_{sv} = \left[z_s - \frac{l_g}{2},\ z_s + \frac{l_g}{2} \right] \tag{4.3}$$

A single acoustic pulse emission $e_{T0}(t)$ – the pulsed excitation basis function described in Section 2.1.3 – is initiated at time t_{e0} and travels outward from the transducer with propagation velocity c. Scatterer and pulse front depth along the z-axis are expressed as [6]:

$$z_{scatterer}(t) = z_0 + t\,|\vec{v}|\cos\theta_D = z_0 + v_z t \tag{4.4}$$

$$z_{pulse}(t) = c \cdot (t - t_{e0}) \cdot H_{step}(t - t_{e0}) \tag{4.5}$$

where $H_{step}(t)$ is the Heaviside step function, given by:

$$H_{step}(t) = \begin{cases} 0, & t < 0 \\ 1, & t \geq 0 \end{cases} \tag{4.6}$$

The scatterer and pulse front are spatiotemporally coincident at the interaction time t_{i0}, which results in the emission of a scattered acoustic wave and yields an interaction time of:

$$z_{scatterer}(t_{i0}) = z_{pulse}(t_{i0}) \to t_{i0} = \frac{z_0}{c - v_z} + \frac{c}{c - v_z} t_{e0} \tag{4.7}$$

Beginning at time t_{r0}, a backscattered wave is received at the transducer. The time delay between pulse emission and interaction is equivalent to the time delay between interaction and pulse reception, leading to the relation [33]:

$$t_{r0} = t_{e0} + 2(t_{i0} - t_{e0}) \to t_{e0} = t_{r0}\frac{c - v_z}{c + v_z} - \frac{2z_0}{c + v_z} \tag{4.8}$$

Due to periodic replication of the emitted pulse, a single pulse receive waveform can be written in terms of the emitted pulse from the preceding pulse repetition:

$$e_{Rn}(t) = A_R e_{Tn}\left(t\frac{c - v_z}{c + v_z} - \frac{2z_0}{c + v_z}\right) = A_R e_{T(n-1)}\left(t\frac{c - v_z}{c + v_z} - \frac{2z_0}{c + v_z} - T_{PRP}\right) \tag{4.9}$$

where A_R is an amplitude scaling coefficient – accounting for scattering strength, attenuation, and other factors – and T_{PRP} is the pulse repetition period ($T_{PRP} = \frac{1}{f_{PRF}}$).

By recursion to the initial pulse emission, the single pulse receive waveform due to the n^{th} pulse repetition can described in terms of the pulsed excitation basis function:

$$e_{Rn}\left(t\right) = A_R e_{T0}\left(t\frac{c - v_z}{c + v_z} - \frac{2z_0}{c + v_z} - nT_{PRP}\right) \tag{4.10}$$

Summation of the single pulse receive waveforms over all pulse repetitions yields the electrical receive signal $e_R\left(t\right)$:

$$e_R\left(t\right) = \sum_{n=0}^{\infty} e_{Rn}\left(t\right) \tag{4.11}$$

Sampling $e_R\left(t\right)$ at the pulse repetition frequency (i.e., one sample per pulse period) with a constant sample offset time T_s – corresponding to the desired sampling depth z_s – yields a discrete-time receive sequence $x\left[n\right]$:

$$x\left[n\right] = e_R\left(nT_{PRP} - T_s\right) \tag{4.12}$$

To avoid time aliasing, the pulse repetition frequency must be selected such that received signals from adjacent pulse repetitions do not overlap in time. Under this f_{PRF} requirement, the n^{th} sample is determined solely by the n^{th} single pulse receive waveform:

$$x\left[n\right] = e_{Rn}\left(nT_{PRP} - T_s\right) \tag{4.13}$$

Without loss of generality, the pulsed excitation basis function is expressed as a gated sinusoid to facilitate spectral analysis of the receive sequence $x\left[n\right]$:

$$e_{T0}(t) = \prod\left(\frac{t}{T_e M} - \frac{1}{2}\right)\sin\left(2\pi f_e t\right) = \begin{cases} \sin\left(2\pi f_e t\right), & 0 \le t \le T_e M \\ 0, & \text{otherwise} \end{cases} \tag{4.14}$$

Using the basis function expression, the receive sequence can be solved for explicitly.

$$x[n] = A_R e_{T0} \left(nT_{PRP} \frac{c - v_z}{c + v_z} - nT_{PRP} - \frac{2z_0}{c + v_z} - T_s \frac{c - v_z}{c + v_z} \right) \tag{4.15}$$

Defining a constant phase term ψ_e:

$$\psi_e = 2\pi f_e \left(\frac{2z_0}{c + v_z} + T_s \frac{c - v_z}{c + v_z} \right) , \tag{4.16}$$

yields a reduced form of the expression:

$$x[n] = -A_R \sin \left(\frac{4\pi f_e T_{PRP} v_z n}{c + v_z} + \psi_e \right) \tag{4.17}$$

Therefore, under the simplified framework presented, sampling the electrical receive signal $e_R(t)$ at the pulse repetition frequency yields a frequency spectrum with energy concentrated at the Doppler frequency f_d:

$$f_d = \pm \frac{2 f_e v_z}{c + v_z} \approx \pm \frac{2 f_e v_z}{c} \tag{4.18}$$

Pulse repetition frequency limits exist in order to ensure aliasing is prevented throughout the velocity estimation procedure. To avoid aliasing in the frequency domain, a minimum pulse repetition frequency $f_{PRF,\min}$ is determined by the maximum scatterer velocity magnitude.

$$f_{PRF,\min} = \frac{4 f_e v_{\max}}{c} \tag{4.19}$$

This restriction permits scatterer velocity to vary within $[-v_{\max}, v_{\max}]$ without risk of frequency aliasing. A priori knowledge of scatterer velocity (e.g., absence of negative flow) can be used to extend acceptable flow velocities to larger values without accuracy degradation – via non-symmetric interpretation of spectral data. Pathological blood flow is, however, often notably distinct from normal flow patterns, which cannot generally be presumed. In TCD applications, flow direction is highly dependent on anatomical factors – transtemporal insonation typically yields positive flow velocities for the ipsilateral MCA and negative flow velocities for the ipsilateral anterior cerebral artery.

As sampling depth z_s increases, scattered energy from the sample volume takes additional time to reach the transducer surface and therefore the rate of pulse emissions (i.e., f_{PRF}) must decrease to avoid time domain aliasing:

$$f_{PRF,\max} = \frac{c}{2z_s + l_g} \tag{4.20}$$

The preceding velocity estimation procedure is primarily founded on methods introduced by Bonnefous and Pesque, which were later refined by Jensen [46, 73] and presented in [6]. Alternate velocity estimation methods are also commonly used, including phase and autocorrelation-based techniques, presented in [32, 74].

4.1.2 Velocity Estimation for an Ensemble of Scatterers

The velocity estimation methods initially presented for a single scatterer can be expanded to practical acoustic contexts for a collection of scatterers. Recall from Equation 2.57 that the electrical receive signal $e_R(t)$ is established via convolution of the PW transmit excitation waveform $e_T(t)$ with physical system characteristics – notably transmit and receive transducer impulse responses $g(t)$ and spatial impulse responses $h(t)$. Because the convolution operation is time invariant, the receive waveform from stationary scatterer and time-shifted pulse emissions is unchanged – neglecting noise effects.

If the effective pulse-echo spatial impulse response $h_{PE}(\vec{r}, t)$ is relatively constant in magnitude for the range of scatterer positions, then scatterer waveforms can be approximated solely by timing delays with no appreciable change in amplitude. For scatterers confined to the sample volume depth range z_{sv} and within a nearly constant magnitude region of the pulse-echo beam pattern main lobe, the velocity estimation procedure remains valid. As scatterers move away from the z-axis, the use of a single Doppler angle θ_D becomes less valid due angular spreading. Such angle variation errors, however, are fairly negligible in TCD insonation of the MCA, since the scatterers are confined to a roughly 3mm diameter vessel at a sample depth of $\approx$ 40mm [6].

For transducer arrays, where beam steering enables the main lobe to be offset from the vector normal to the transducer surface, the coordinate system can be transformed such that the z-axis corresponds to the beam steering angle, and θ_D is defined between the steering direction and the scatterer velocity vector, thus approximating the phased array as an equivalent steered element.

Because a linear system is assumed, velocity estimation analysis can be applied to an ensemble of scatterers defined by a dynamic scattering field $s\left(\vec{r}, t\right)$, where each scatterer position is approximated using a scatterer velocity vector and previous scatterer position:

$$\vec{r_n}\left(t\right) = \lim_{\Delta t \to 0} \vec{r_n}\left(t - \Delta t\right) + \vec{v_n}\left(t\right)\Delta t \tag{4.21}$$

One practical inconsistency with the velocity estimation analysis presented in Section 4.1.1 is that constant scatterer velocity is maintained over all pulse repetitions, but scatterers must remain confined to the sample volume depth range z_{sv} and a constant magnitude region of the pulse-echo beam pattern. These analytical limitations present two major discrepancies. First, blood flow within major arteries is a highly pulsatile phenomenon. Scatterer velocity is therefore grossly misrepresented by a constant velocity approximation. Blood flow velocity can, however, be accurately characterized as constant over a time interval of several milliseconds [75]. Second, after sufficient time all scatterers with non-zero velocity will not be confined to the sample volume depth range or a constant magnitude region of the pulse-echo beam pattern.

These concerns can be mitigated by use of the spectrogram, known in the context of ultrasound as the sonogram, which provides a time-varying spectral representation of the receive sequence $x\left[n\right]$ through computation of the time-dependent Fourier transform [76]. To determine the spectral content of $x\left[n\right]$ for a particular sample interval – corresponding to a time interval in $e_R\left(t\right)$ – the receive sequence is multiplied by a window sequence.

For a sufficiently short window (i.e., on the order of several milliseconds in duration), flow velocity characteristics and the pulse-echo spatial impulse response magnitude (across the length traveled by a scatterer) can be approximated as constant [77–79]. For an ensemble of erythrocytes at *in vivo* concentrations and flow velocities, there will still be a large number of scatterers entering and exiting the sample volume depth range. From each pulse repetition, however, this number is a slight fraction of the total scatterers within the sample volume and is neglected [6].

The spectral content of $x[n]$ for arterial blood flow – even when utilizing short window sequences – contains a wide distribution of frequencies, a result of radial dependence of erythrocytic velocity. Within the circulatory system, blood flow is often laminar (i.e., Reynolds number < 2000) and evidence of turbulence can be an indication of pathology (e.g., stenotic vessel). A notional scatterer velocity distribution for laminar flow is depicted in Figure 4-3.

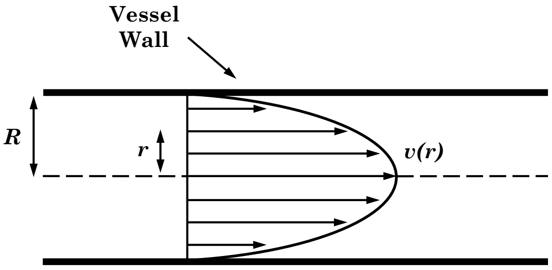

Figure 4-3: Laminar flow velocity in a long, rigid tube. Adapted from [6, 33].

The scatterer velocity profile for steady (i.e., non-pulsatile) laminar flow in a rigid tube can be described by the Poiseuille relation, given by [33]:

$$v(r) = v_{0,\max}\left[1 - \left(\frac{r}{R}\right)^{p_0}\right] \tag{4.22}$$

where r is radial position, R is tube radius, $v_{0,\max}$ is maximum scatterer velocity, and p_0 is velocity profile order. Near an inlet, entrance effects tend to dominate thereby yielding a flat velocity profile ($p_0 \to \infty$). For long tubes, viscosity effects establish parabolic flow ($p_0 \to 2$). As indicated by Equation 4.22, a linear relationship exists between $v_{0,\max}$ and mean flow velocity.

In practice, blood vessels are elastic structures, rather than rigid tubes, and blood flow is pulsatile, rather than steady. Scatterer velocity is therefore radially and temporally influenced. Using Fourier decomposition, scatterer velocities throughout pulsatile flow can be analyzed from a set of Womersley equations, but require a number of vessel specific parameters not generally available in a clinical setting [80, 81].

Ideally, the spectral power at a particular Doppler frequency is proportional to the number of erythrocytes within the sample volume moving at the corresponding axial velocity. Formally, since the backscatter coefficient of blood is nonmonotonic with hematocrit, this relationship is not valid for erythrocyte scattering (as described in Section 2.1.1). However, because hematocrit is assumed constant throughout the sample volume, the proportionality assumption is approximately valid. Therefore, calculation of spectral mean Doppler frequency $\bar{f}_d[n]$ can theoretically yield an accurate representation of mean flow velocity $\bar{v}[n]$ [6].

Spectral mean Doppler frequency $\bar{f}_d[n]$ is computed by power-weighting the spectral content of the time-dependent discrete Fourier transform (TDDFT) of $x[n]$:

$$\bar{f}_d[n] = \frac{\int\limits_0^{2\pi} \lambda |X[n,\lambda)|^2 d\lambda}{\int\limits_0^{2\pi} |X[n,\lambda)|^2 d\lambda} \tag{4.23}$$

where $X[n,\lambda)$ is the TDDFT of $x[n]$ [76]. Recall that n is a sequence index corresponding to continuous time sampling at $t_n = n \cdot T_{PRP} + T_s$.

Doppler estimated mean flow velocity $\bar{v}[n]$ is thereby expressed as:

$$\bar{v}[n] = \frac{\bar{f}_d[n]\, c}{2 f_e \cos\theta_D} \tag{4.24}$$

Volumetric flow (e.g., CBF through the MCA) can be obtained by utilizing measured vessel diameter $d_v[n]$:

$$q[n] = \frac{\pi \bar{v}[n]\, d_v^2[n]}{4} = \frac{\pi c \bar{f}_d[n]\, d_v^2[n]}{8 f_e \cos\theta_D} \tag{4.25}$$

Equation 4.25 is not generally useful in clinical evaluation, since accurate vessel diameter measurements are often unavailable in TCD applications.

Finally, if vessel diameter is constant over the cardiac cycle, blood flow through the vessel can be estimated to within a constant scale factor (i.e., q_0). For a constant vessel diameter, the linear relationship between volumetric blood flow and mean flow velocity $\bar{v}[n]$ facilitates changes in blood flow within the vessel of interest to be directly monitored using CBFV measurements.

$$\hat{q}[n] = \frac{\pi c \bar{f}_d[n] d_v^2}{8 f_e \cos\theta_D} = q_0 \bar{f}_d[n] \tag{4.26}$$

4.2 Doppler Velocimetry Signal Processing

Signal processing is necessary to condition the received radio frequency (RF) echo waveforms into meaningful velocimetry data. Developments in digital signal processing electronics have enabled the practical realization of robust configurable processing schemes primarily defined by system firmware.

The velocity estimation analysis presented in Section 4.1.2 was simplified for analytical tractability. A practical velocity estimation signal processing scheme used throughout this work is presented in Figure 4-4, where G_{AFE} is the analog front-end (AFE) amplifier gain, T_{ADC} is the analog-to-digital converter (ADC) sampling period, $w[n]$ is a windowing sequence, M_D is the decimation factor, and FFT is the fast Fourier transform operation. Alternative velocity estimation methods are often used – especially in distinct applications like color flow imaging – and are described in [32, 33].

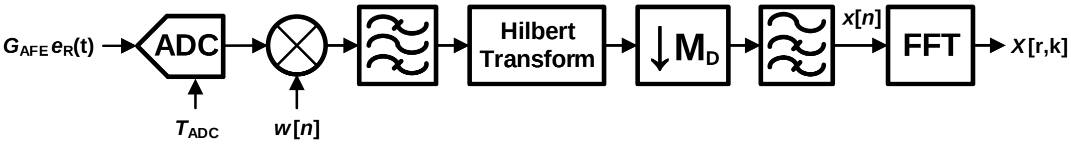

Figure 4-4: Velocity estimation signal processing block diagram.

The windowing sequence $w[n]$ is used to segment the sampled data into fixed length sequences. A decrease in window sequence length results in finer temporal resolution, but also yields spreading of the Doppler spectrum – a phenomenon known as spectral broadening. By evaluating expected time-variation and frequency content in realistic CBFV waveforms, a sufficient balance between time and spectral resolution can be achieved through selection of $w[n]$ length, denoted N_w.

Matched filtering is used subsequent to windowing to limit out of band noise and interferers, thereby increasing signal-to-noise ratio (SNR). The SNR of the received signal after filtering is theoretically maximized when the filter transfer function is matched to the spectral content of the received signal. An optimal matched filter can be implemented by defining the filter impulse response $h_{bp}[n]$ as the underlying pulsed excitation basis function $e_{T0}(t)$ sampled at T_{ADC}. Neglecting frequency dependent attenuation and transducer bandwidth effects, the spectral envelope of the received signal is therefore approximately equivalent to the band-pass filter transfer function and SNR is maximal [6].

The Hilbert transform is used in Doppler processing to generate an analytic signal (i.e., a complex valued signal composed of in-phase and quadrature data) from the real valued receive sequence and is defined in the frequency domain as [76]:

$$H_{HT}(\omega) = \begin{cases} e^{+\jmath\pi/2}, & -\pi < \omega < 0 \\ e^{-\jmath\pi/2}, & 0 < \omega < \pi \\ 0, & \omega = -\pi,\ 0,\ \pi \end{cases} \tag{4.27}$$

In effect, the Hilbert transform implements a 90° phase shift to achieve in-phase $y_I[n]$ (i.e., original real valued signal) and quadrature $y_Q[n] = y_I[n] * h_{HT}[n]$ signals. The analytic signal output of the Hilbert transform processing block is then formed as $y_{HT}[n] = y_I[n] + \jmath y_Q[n]$. As is evident from Equation 4.17, the baseband receive sequence $x[n]$ is a weighted summation of sinusoidal waveforms and thus yields a symmetric spectra. The Hilbert transform dissociates this symmetry prior to decimation by oppositely affecting positive and negative complex exponential components such that spectral content corresponds to both flow velocity and flow direction – that is, flow away from the transducer only yields spectral content at negative frequencies and flow toward the transducer only yields spectral content at positive frequencies.

The baseband receive sequence $x[n]$ is realized via decimation by $M_D = \frac{T_{PRP}}{T_{ADC}}$. Due to this decimation factor relationship, the receive signal is consequently sampled at T_{PRP}. Because energy still exists over a wide spectral range, significant aliasing occurs during decimation. Such aliasing does not, however, degrade the baseband signal as it results in reinforcement of the main tone – and corresponding Doppler information – by the secondary tones and equivalent Doppler content. Prior to decimation, the sequence should be shifted by the sample offset T_s such that the baseband samples correspond to scatterer interactions within the sample volume centered at the sample depth z_s [6].

Scattering from stationary tissue tends to dominate the receive signal spectrum. Practical systems must therefore incorporate sharp high-pass filtering of the baseband signal, often referred to as the wall or clutter filter, to attenuate the high amplitude stationary reflections (i.e., spectral content at or near DC).

The FFT is used to implement the discrete Fourier transform, which allows computation of the processed receive sequence spectral content – and therefore the velocity distribution of the scatterer ensemble. Characteristics of the frequency spectra are highly influenced by window sequence length and an N_w-point FFT is generally taken to compute spectral content – since, beyond N_w, higher-order transforms do not improve spectral resolution. Temporal resolution and noise effects can be improved to a degree by averaging overlapping data segments, rather than using adjacent segments, known as Welch's method.

The time-varying spectral information contained in $X\left[r,k\right]$ is visually presented using the sonogram, which depicts the Doppler spectral power within individual frequency bins – nominally corresponding to the relative number of scatterers traveling within a given velocity range – for each time segment by a gray scale or color intensity. Assuming uniform insonation of the vessel cross-section, the approximate spatial distribution of velocities across the vessel lumen can therefore be visualized.

4.2.1 Spectral Envelope Generation

The spectral mean Doppler frequency $\bar{f}_d\left[n\right]$ is established in Equations 4.23 and 4.24 as the primary variable of interest. However, use of $\bar{f}_d\left[n\right]$ in velocimetry estimation is only formally valid under a narrow set of demanding conditions [55]:

1. There are no vascular bruits or vessel wall movements.
2. The signal to noise ratio is sufficiently high.
3. The sample volume is centered on a straight segment of the artery.
4. There are no branches or adjacent small vessels within the sample volume.
5. There is minimal beam pattern variation over the cross-section of the vessel.

In clinical settings, most of these conditions are violated and the accuracy of velocity measurements is therefore degraded. Consequently, TCD instrumentation and most clinicians have adopted the Doppler spectral envelope $f_{d,\max}$ – the maximum instantaneous Doppler frequency – as the relevant measurement parameter in a majority of TCD applications.

The Doppler spectral envelope – and the related velocity envelope $v_{\max}$ – generally corresponds to the velocity in the lumen centerline and under laminar flow is proportional to mean flow velocity. As previously noted, arterial blood flow is pulsatile in nature and is not entirely described by the Poiseuille relation – given in Equation 4.22. However, the small diameter of the cerebral vessels – relative to other major arteries – has a stabilizing effect on the velocity profile and experimental results have validated the laminar flow approximation within the MCA [55].

Use of the Doppler spectral envelope $f_{d,\max}$ – in place of the spectral mean Doppler frequency $\bar{f}_d\,[n]$ – yields a less sensitive, more robust characterization of CBFV in clinical environments. Validity of $\bar{f}_d\,[n]$ requires that the entirety of the vessel cross-section is equally insonated – an unattainable condition in practice. Accurate application of the Doppler spectral envelope $f_{d,\max}$, however, requires only that some portion of the sample volume contains the region of maximal flow velocity $v_{\max}$.

Robust generation of the spectral envelope under low SNR conditions, however, is problematic and is itself an area of research. A variety of spectral analysis methods for envelope estimation – including autoregression, singular value decomposition, neural network analysis, wavelet transformation, and Fourier analysis – are found in the relevant literature [77, 82–86].

Figure 4-5 displays simulated spectral content for parabolic flow under variable SNR conditions with an underlying Doppler spectral envelope $f_{d,\max}$ of 2.5kHz. In Figure 4-5(a) – where SNR is 10dB – the transition from noise power to Doppler flow power at 2.5kHz is visually apparent and readily estimated with minimal error under a variety of spectral envelope estimation techniques. In Figure 4-5(b) – where SNR is 2dB – the transition from noise power to Doppler flow power is less visually discernible and estimation of the Doppler spectral envelope is highly variable and method dependent.

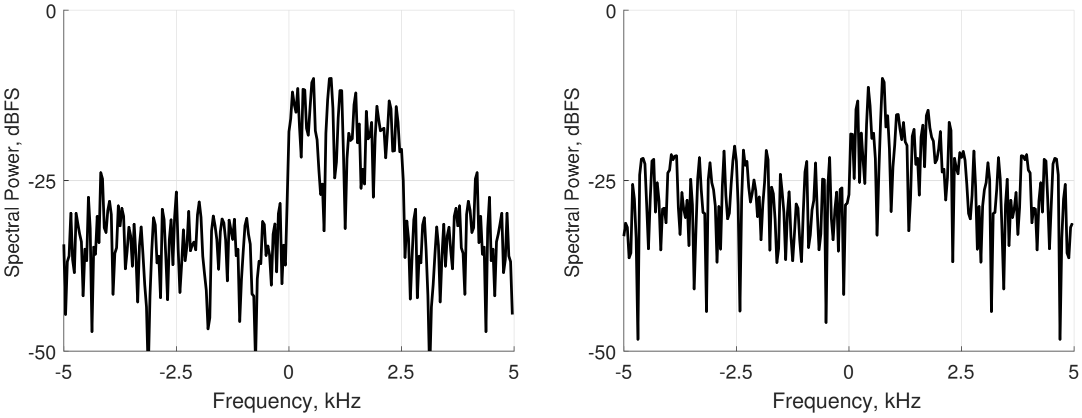

(a) Spectrum for $SNR = 10$dB.

(b) Spectrum for $SNR = 2$dB

Figure 4-5: Simulated spectral characteristics of parabolic flow under variable SNR.

A simulated stationary Doppler signal with known spectral characteristics is generated and utilized as a reference sequence; white noise is added to enable assessment under various SNR values. Fourier transformation – via FFT – and autoregression (AR) – via Burg's method – are employed for spectral evaluation. Spectral envelope estimation is performed on the underlying spectra using the modified threshold crossing method (MTCM) and the hybrid geometric method, described in [87, 88].

Figures 4-6 and 4-7 present the mean and standard deviation of spectral envelope bias for an underlying constant parabolic flow simulation with $v_{\max}$ of 100cm/s. Autoregressive spectral evaluation is computed for fixed model order (i.e., $p = 8$) and for the optimal Akaike information criterion (AIC) model order [89].

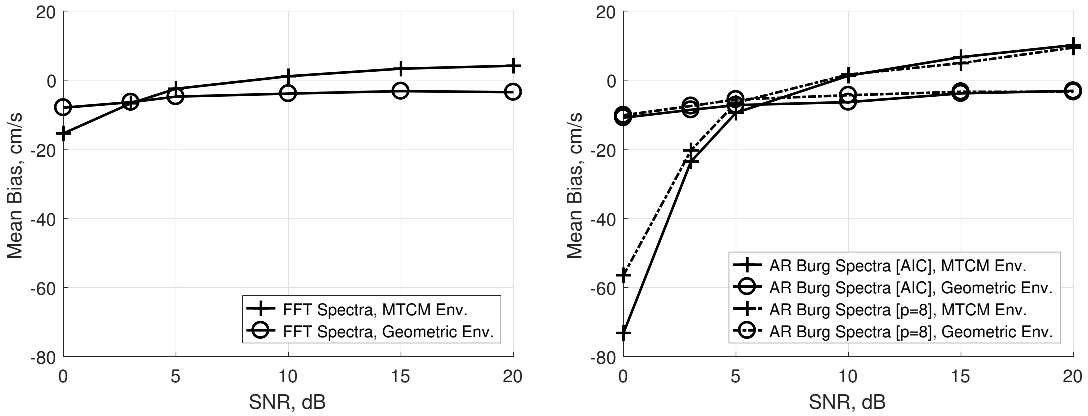

(a) Fourier transform spectral generation. (b) Autoregressive spectral generation.

Figure 4-6: Simulated mean spectral envelope bias for $v_{\max} = 100$cm/s under variable SNR.

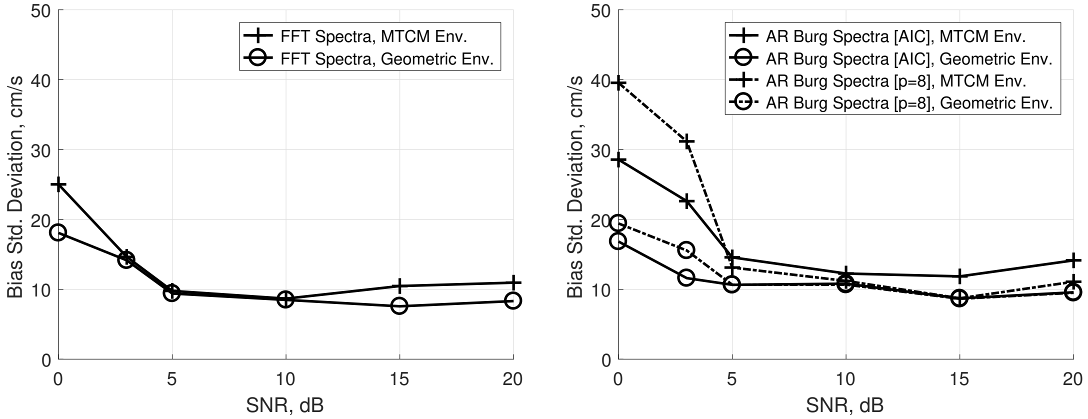

(a) Fourier transform spectral generation. (b) Autoregressive spectral generation.

Figure 4-7: Simulated standard deviation of spectral envelope bias for $v_{\max} = 100$cm/s under variable SNR.

Over the expected range of CBFV values – specifically $|v_{\max}| \leq 150$cm/s – and SNR values relevant to TCD sonography – specifically SNR < 20dB – autoregressive spectral evaluation methods tended, on average, to yield significantly higher mean and standard deviation of spectral envelope bias than FFT-based approaches. Applying Fourier transform spectral evaluation over the range of CBFV and SNR values, the MTCM and hybrid geometric method yielded nearly equivalent mean normalized spectral envelope biases of 6.2% and 7.8%, respectively. MTCM evaluation, however, yielded significantly lower normalized bias variability than the hybrid geometric method – specifically, $\sigma_{MTCM} = \pm 3.6\%$ and $\sigma_{Geo} = \pm 6.1\%$. The MTCM for spectral envelope estimation using FFT-based spectral evaluation is considered throughout the remainder of this work.

The modified threshold crossing method (MTCM) is a simple iterative algorithm based on the chi-square statistics of white noise spectra [82]. Starting from the edge (positive or negative) of the power spectra, power samples in successive frequency bins are compared to a threshold noise level (ψ_{MTCM}). If there are at least m_{MTCM} bins that exceed the threshold noise level ψ_{MTCM} in a sequence of r_{MTCM} successive bins (typically $m_{MTCM} = r_{MTCM} = 2$), the Doppler spectral envelope estimate $\hat{f}_{\max}$ is taken as the highest bin frequency in the sequence [87, 88]. If a particular spectra does not yield an adequate threshold crossing, $\hat{f}_{\max}$ from the preceding spectra is used (i.e., zero-order hold). The threshold noise level ψ_{MTCM} is a scaled average of spectral noise power from the edges of the power spectra (i.e., frequencies corresponding to flow velocities outside an assumed physiological limit), where the theoretically optimal scaling factor N_{MTCM} is SNR dependent – $N_{MTCM} = 8$ for 5dB $<$ SNR $<$ 13dB [87].

4.3 Power Mode Doppler Signal Processing

As described in Section 2.1.1, the relationship between the quantity of erythrocytes within the sample volume and resultant backscattered power is exceedingly complex. To first order, however, as the overlap between sample volume and vessel cross-section increases, backscattered Doppler power consequently increases. Characterization of Doppler power can therefore be valuable in certain TCD applications [17]. In this work, Doppler power analysis is employed to guide algorithmic beamformation for autonomous vessel location and tracking.

The Doppler power ratio P_{rel} represents the degree of erythrocytic scattering and its relative direction within the sample volume:

$$P_{rel} = \frac{\int_{0}^{\pi} |X[n,\lambda)|^2 d\lambda}{\int_{\pi}^{2\pi} |X[n,\lambda)|^2 d\lambda} \tag{4.28}$$

where – as in Equation 4.23 – $X[n,\lambda)$ is the TDDFT of the baseband receive waveform $x[n]$ after clutter reject filtering.

In regions with dominant positive flow, spectral power at positive frequencies ($0 < \lambda < \pi$) greatly exceeds spectral power at negative frequencies ($\pi < \lambda < 2\pi$), yielding large values of P_{rel} ($\sim$ 5 to 20 dB). For unidirectional positive flow, as expected in TAW insonation of the MCA, spectral power at negative frequencies is due entirely to system noise. Assuming frequency-independent baseband noise, mean Doppler power ratio $\bar{P}_{rel}$ thereby yields measurement SNR:

$$SNR = \left(\bar{P}_{rel} - 1\right)/2 \tag{4.29}$$

Maximization of P_{rel} through electronic beamformation therefore nominally yields a sample volume with minimal negative flow, maximal vessel overlap area, and maximal SNR. In contrast to integrated Doppler power, a simultaneous ratio of powers is employed to determine P_{rel}. Values of P_{rel} are therefore largely self-calibrated and can be equitably compared throughout the focal region bounds without accounting for focal depth, acoustic attenuation and reflection, transducer beam pattern, and transmit power level.

4.3.1 Doppler Power Mapping

Doppler power mapping is employed in this work for autonomous localization of CBFV. Mapping occurs as a two-step process: coarse vessel search and fine vessel search. A coarse grid is initially defined over the entire volume of interest. For MCA localization, the search region extent is confined to ±15mm in both lateral dimensions and 40 – 65mm in depth. For each coarse grid position, the system dwells for a defined number of pulse repetitions. Following the dwell period, P_{rel} is determined and the system updates the beamformation coefficients to achieve focusing at the subsequent coarse grid position. Spacing between adjacent coarse grid locations is limited to the half-power main lobe beamwidth, such that undersampling of the volume is avoided.

At coarse grid locations yielding a Doppler power ratio above a specified threshold value, a fine local grid is defined and the dwell process repeated. The Doppler mapping procedure returns the location corresponding to the global Doppler power ratio maxima following local subsampling and redundancy checks – to ensure consistency and signal integrity in identified high flow regions. Fine local search greatly improves the minimum map resolution for a marginal increase in cumulative vessel search time.

Because the MCA – under standard anatomic configurations and non-pathological conditions – is the dominant source of positive flow within the search region, the search process infers a suitable focal location for MCA velocimetry – nominally with full overlap of the vessel lumen and acoustic sample volume. Alternate objective functions, search volume bounds, and vessel identification criteria can be utilized in Doppler mapping to improve measurement robustness for various intracranial vessels and monitoring applications.

4.3.2 Doppler Power Tracking

Vessel tracking is a continuous background process that defines a secondary (i.e., tracking) receive focus; the primary (i.e., hold) receive and transmit focal regions remain coincident. The procedure steers the tracking receive focus at offsets from the hold receive focus and compares the Doppler power ratio P_{rel} of both receive paths. If Doppler power ratio in the tracking receive path exceeds that of the hold receive path for sufficient duration, the transmit and hold receive path focal points are updated.

A diagram of the vessel search and tracking processes is presented in Figure 4-8.

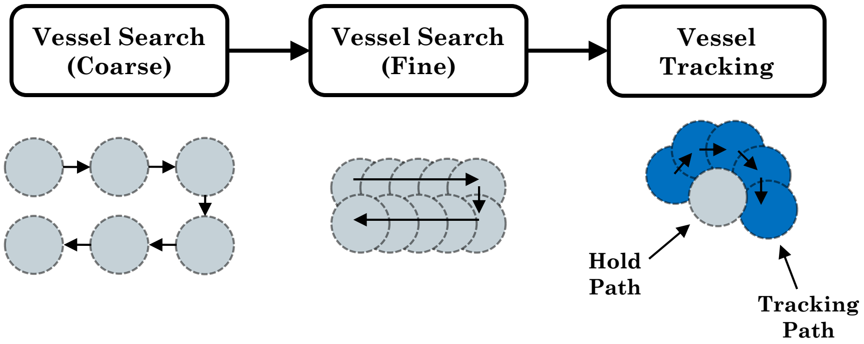

Figure 4-8: Doppler mapping vessel search and tracking processes.

Figure 4-9 presents a flowchart of the algorithmic vessel search and tracking procedures.

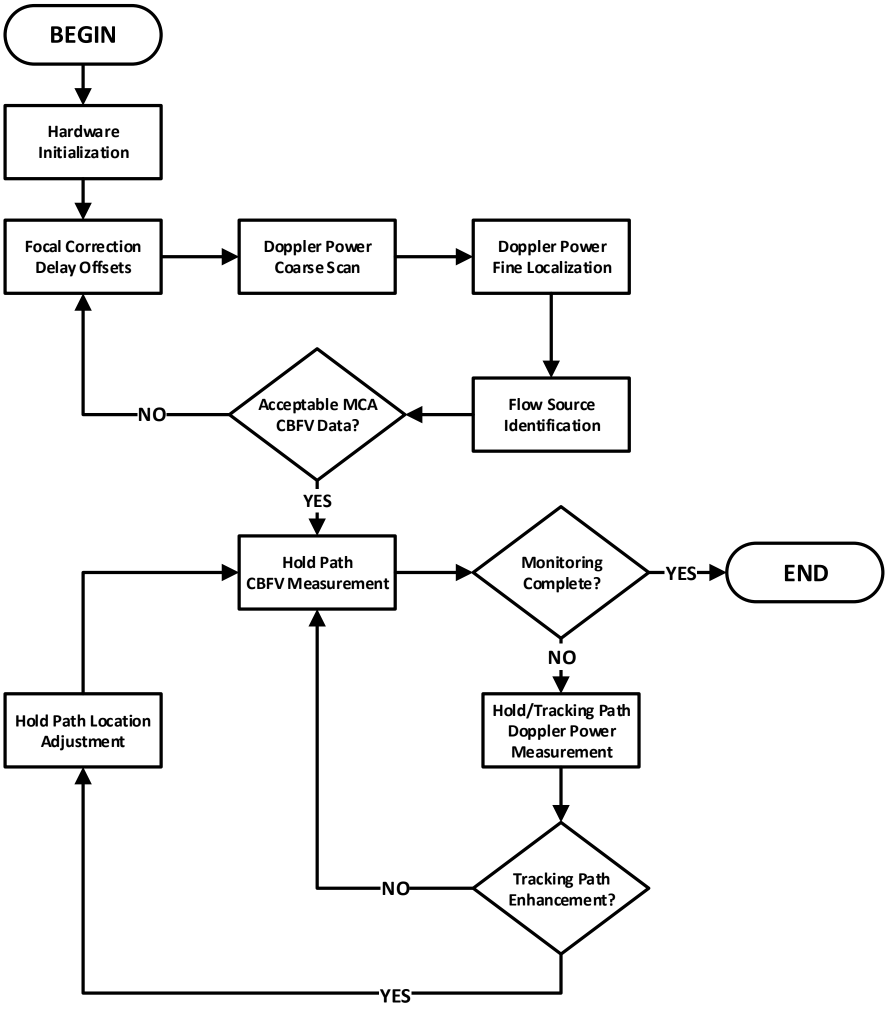

Figure 4-9: Flowchart of vessel search and tracking algorithms.

Tracking procedures enable the system to adapt to relative vessel motion and simultaneously maintain uninterrupted CBFV monitoring. Limitations in tracking robustness are highly dependent on the transmit half-power main lobe beamwidth ($\approx$ 2 to 4mm) and relative vessel movement dynamics. If vessel tracking fails to maintain sufficient Doppler power ratio, the Doppler power mapping procedure is repeated until a suitable vessel segment is located.

4.3.3 Multi-Gate Processing

Acoustic intensity – for both focused and unfocused apertures – generally diverges axially more moderately than it does laterally. Multi-gate processing leverages this aspect by defining multiple range gates during decimation – typically corresponding to within the depth of focus ($\approx$ 10 to 20mm). For a given focal region, this effectively enables the system to achieve Doppler velocimetry operation at an arbitrary number of finely spaced (e.g., $\approx$ 2mm) sample depths – although measurements are not generally independent due to finite range gate length l_g.

Multi-gate processing is utilized in Doppler power mapping to enable multiple simultaneous search locations, thereby reducing cumulative vessel search time. In Doppler power tracking, numerous range gates are employed in the hold and tracking paths to increase effective tracking volume coverage. Multi-gate processing requires per gate clutter filtering and Fourier transformation, thereby practically limiting the viable number of range gates for given processing and communication resources.

4.4 Focal Correction

Transducer arrays, by employing timing delays, can achieve non-physically realizable apertures and are thereby well suited for focal correction techniques, which are used to restore coherence at the focal point following refraction and aberration induced beam degradation [90]. By utilizing hydrophone-assisted phase correction (i.e., adjustment of excitation phases based on hydrophone measurements when inhomogenieties are present) on *ex vivo* skulls for a phased array operating at an excitation frequency of 0.74MHz, Clement and Hynynen were able to attain pronounced improvements to beam pattern definition and focal intensity as compared to uncalibrated focusing for the same acoustic output power [91].

Although hydrophone-assisted techniques are not applicable for *in vivo* measurements, they validate the utility of focal correction methods in transcranial sonography. For pulse-echo operation, simplified focal correction techniques can utilize reflected echo timing to estimate skull thickness and – assuming known acoustic propagation velocities – estimate the propagation delay from each element to the desired focus. Focal correction of delay coefficients can subsequently incorporate these model-based propagation times to increase *in vivo* focal intensity.

The coordinate framework for focal correction analysis due to bulk inhomogeneities (e.g., cranial bone) is presented in Figure 4-10.

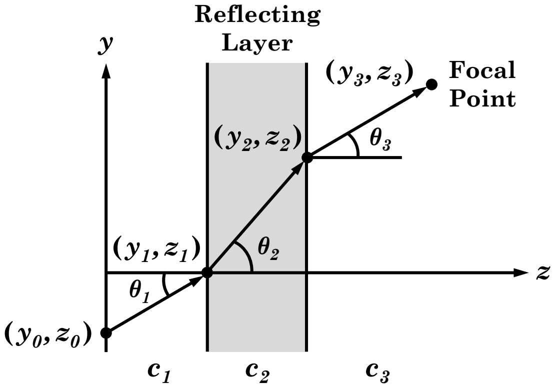

Figure 4-10: Coordinate system for analysis of bulk inhomogeneities.

where – in this analysis – (y_0, z_0) corresponds to the center of the relevant transducer element and (y_3, z_3) corresponds to the desired focal point.

By Snell's law, given in Equation 2.11, the lateral offset through each media section – that is, $\Delta y_i = y_i - y_{(i-1)}$ – can be determined iteratively:

$$\Delta y_i = \frac{c_i \Delta y_{(i-1)} \Delta z_i}{\sqrt{c_{(i-1)}^2 \Delta y_{(i-1)}^2 + c_{(i-1)}^2 \Delta z_{(i-1)}^2 - c_i^2 \Delta y_{(i-1)}^2}} \tag{4.30}$$

Since (y_0, z_0) and (y_3, z_3) are known and propagation velocities are assumed – where $c_1 = c_3$ correspond to soft tissue and c_2 corresponds to cranial bone – the remaining media interface locations (y_1, z_1) and (y_2, z_2) are computed numerically.

After the geometry is known, determination of propagation delay from the transducer element to the focal point is determined:

$$\Delta t = \sum_i \frac{\sqrt{\Delta y_i^2 + \Delta z_i^2}}{c_i} \tag{4.31}$$

Focal correction is simulated in a two-dimensional geometry with 8 transducer elements using k-Wave [31]. Propagation-based correction directly utilizes observed propagation delays from the transducer element to the desired focal point – similar to the hydrophone-based methods in [91]. Echo-based correction estimates the reflecting layer thickness via echo delay times and subsequently employs the analytical framework given in Equations 4.30 and 4.31. The simulated two-dimensional heterogeneous media consists of a 3mm external soft tissue layer, 4.5mm reflecting layer (i.e., cranial bone), and semi-infinite internal soft tissue layer.

Figure 4-11(a) displays the temporal-average intensity for a focal point at (0, 35)mm in a homogeneous soft tissue media. Under fixed steering coefficients, the inclusion of a reflecting layer to create heterogeneity has significant impact on the temporal-average intensity distribution – as shown in Figure 4-11(b).

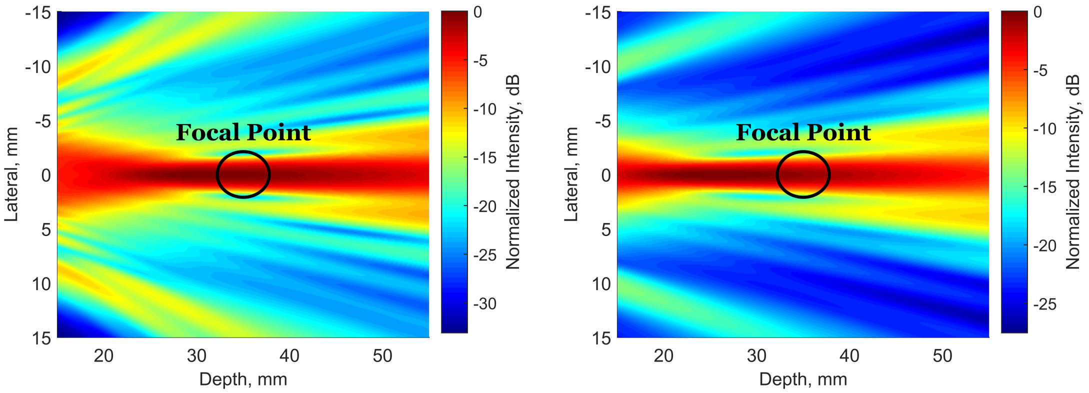

(a) Intensity in homogeneous media.

(b) Intensity in heterogeneous media.

Figure 4-11: Effect of reflecting layer inclusion on temporal-average intensity with an intended (0, 35)mm focus.

Propagation and echo-based focal correction methods are employed to reestablish the desired focal point at (0, 35)mm – as displayed in Figure 4-12.

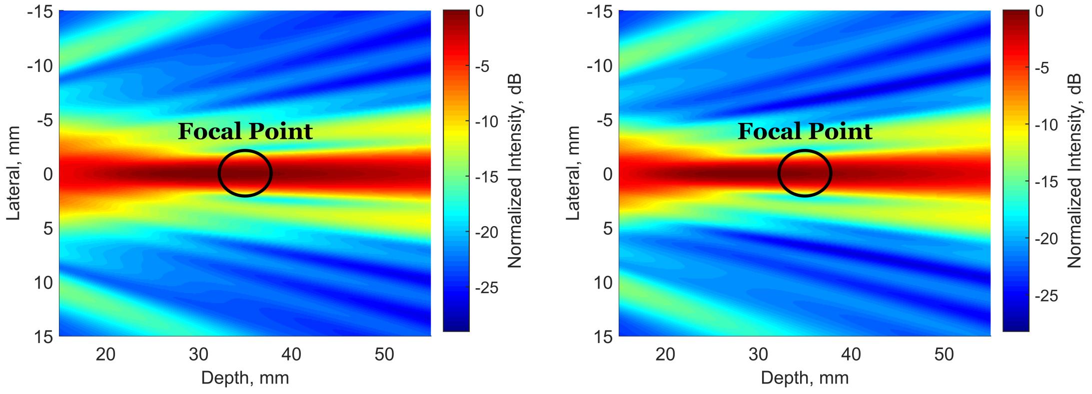

(a) Intensity in propagation-based method.

(b) Intensity in echo-based method.

Figure 4-12: Effect of focal correction methods on temporal-average intensity in heterogeneous media with an intended (0, 35)mm focus.

The propagation-based focal correction method increased focal point temporal-average intensity by 0.7dB compared to the reference case given in Figure 4-11(b). Similarly, the echo-based focal correction method increased focal point temporal-average intensity by 0.3dB compared to the reference case.

The focal delay for each transducer element is given in Figure 4-13 for the reference case – that is, assuming fixed propagation velocity throughout the heterogeneous media – and for both focal correction methods. The propagation and echo-based focal correction methods yield similar trends in element delay values.

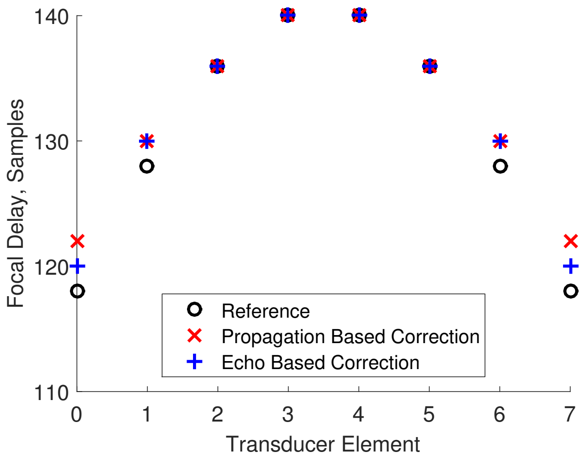

Figure 4-13: Transducer element focal delays in heterogeneous media with an intended (0, 35)mm focus.

Reflecting layer presence yields a limited impact on focal intensity in the reference case for the intended (0, 35)mm focal point – primarily through the reduction of focal length. Degradation of the beam pattern is particularly severe for off-axis focusing. Figure 4-14 presents the temporal-average intensity for nominal focusing at (8, 35)mm in homogeneous and heterogeneous media with fixed steering coefficients.

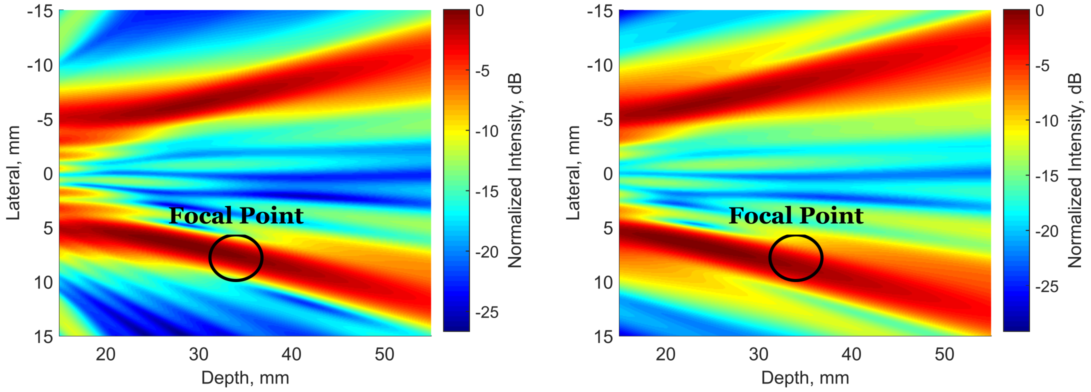

(a) Intensity in homogeneous media.

(b) Intensity in heterogeneous media.

Figure 4-14: Effect of reflecting layer inclusion on temporal-average intensity with an intended (8, 35)mm focus.

Employing focal correction methods yields a marked improvement in focal point intensity, as shown in Figure 4-15.

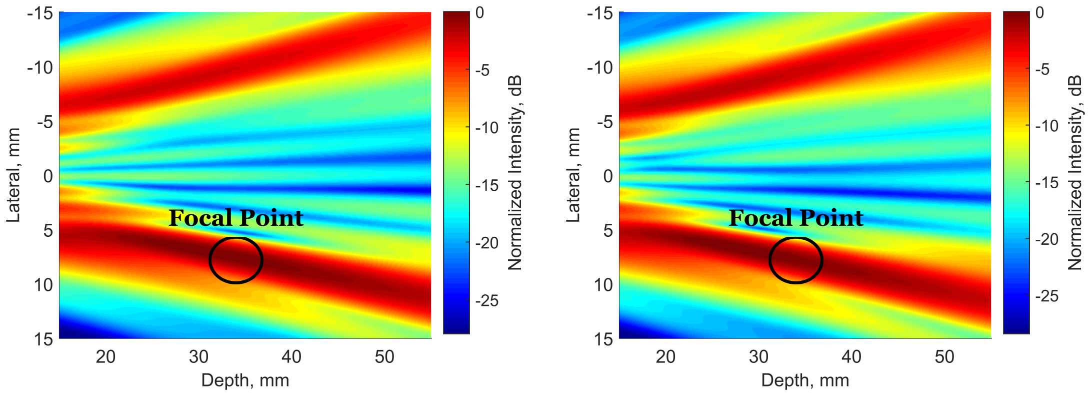

(a) Intensity in propagation-based method.

(b) Intensity in echo-based method.

Figure 4-15: Effect of focal correction methods on temporal-average intensity in heterogeneous media with an intended (8, 35)mm focus.

In Figures 4-14 and 4-15, transducer element pitch above the grating lobe threshold – detailed in Equation 2.51 – is utilized, yielding significant acoustic intensity at the negative steering angle. Practical considerations regarding transducer array design are explored in Section 5.2.

For off-axis steering – with an intended focal point at (8, 35)mm – the propagation and echo-based focal correction methods both increase focal point temporal-average intensity by 1.8dB compared to the reference case given in Figure 4-14(b).

Focal delays for off-axis steering are given for the reference case and both focal correction methods in Figure 4-16. As expected, the propagation and echo-based focal correction methods yield similar trends in element delay values.

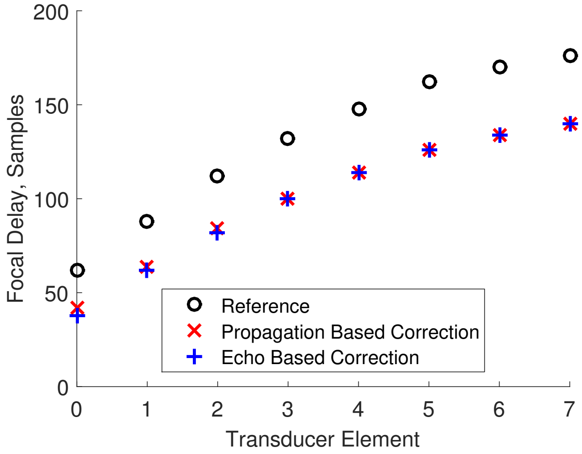

Figure 4-16: Transducer element focal delays in heterogeneous media with an intended (8, 35)mm focus.

Although illustrative, the propagation-based method is unfeasible for *in vivo* measurements, since it requires acoustic measurements at the focal point (i.e., within the brain parenchyma). However, the echo-based focal correction method is realizable with acoustic phased array instrumentation – via analysis of cranial bone reflection characteristics. The echo-based method yielded similar simulated performance in focal-coherence correction as the direct propagation delay method – although propagation velocities were known *a priori*.

The coordinate system presented in Figure 4-10 and ensuing analyses were relevant for two-dimensional geometries. However, the methods described can be adapted to physical three-dimensional geometries through transformation of the coordinate system such that the revised z-axis corresponds to the beam steering angle. Focal correction simulations assumed a cranial bone segment of fixed thickness and acoustic phase velocity. For *in vivo* measurements, cranial bone thickness and acoustic phase velocity vary over lateral extent – especially near the acoustic window location. Additionally, the layered nature of cranial bone results in further inhomogeneity – and likely reduces the effectiveness of focal correction methods [92].

4.5 Summary

This chapter introduces a PW velocity estimation technique and defines a capable signal processing architecture to accommodate non-stationary (i.e., temporally-varying) scattering processes and spectral envelope generation under low SNR conditions. The Doppler power ratio P_{rel} is presented, which enables power mode Doppler signal processing techniques – notably, Doppler power mapping and tracking. The realization of practical mapping and tracking methods facilitates algorithmic vessel localization, thereby reducing operator interaction during monitoring. Lastly, focal correction methods are developed to increase acoustic focal intensity in the presence of tissue inhomogeneities – consequently improving measurement SNR.

Chapter 5

Discrete Phased Array System Design

This work addresses the development of a wearable, highly-compact transcranial Doppler (TCD) sonography system, particularly for middle cerebral artery (MCA) insonation. The design of transducer geometries and electrical hardware must therefore consider a variety of factors relevant to transcranial operation, specifically vascular and cranial window anatomy, blood flow characteristics, acoustic safety indices, spectral analysis, and signal processing limitations – presented in Chapters 3 and 4.

5.1 System Architecture

Hardware development within this chapter utilizes discrete, commercially available circuit components. This approach places considerable restrictions on viable hardware architectures, since access to internal nodes and diversity in component configurations is limited. A capable and robust discrete system architecture is shown in Figure 5-1. Although the present discrete architecture is adequate in achieving necessary system functionality, it does so in a considerably hardware inefficient manner – leading to increased power dissipation, hardware dimensions, and instrumentation complexity. Improvements to this basic architecture will be discussed in Chapter 8.

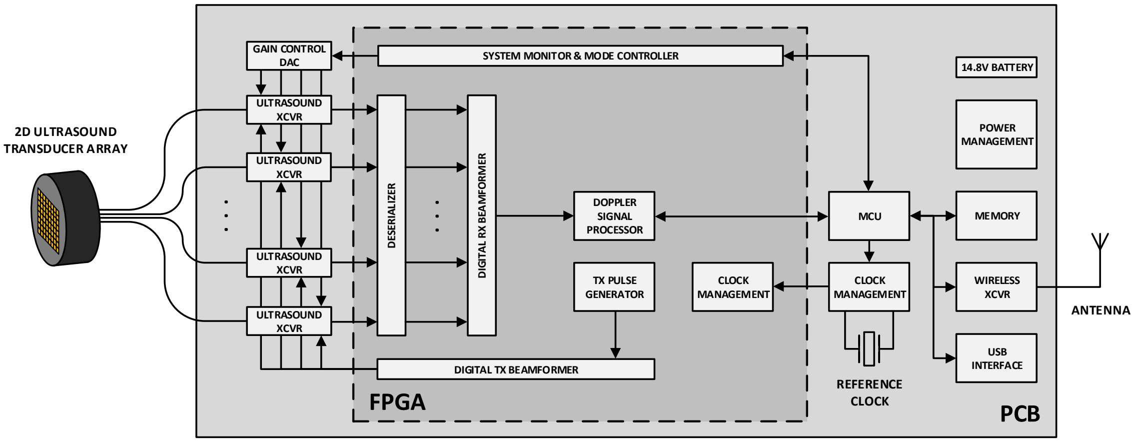

Figure 5-1: Discrete phased array system hardware block diagram.

The discrete prototype contains multi-channel transmit and receive electronics, enabling electronic beamformation via phased array operation. A two-dimensional transducer array achieves volumetric acoustic focusing. Embedded transmit and receive beamformer processing, Doppler signal processing, and vessel location and tracking algorithms facilitate real-time operation with modest remote host communication requirements and limited operator interaction. Digitally configurable power management circuitry for battery powered operation and wireless remote host communication interfaces permit untethered operation of the discrete prototype system.

5.2 Transducer Array Design

During transmission, transducer elements convert electrical excitation waveforms into acoustic perturbations via the piezoelectric effect. During reception, transducer elements reciprocally convert acoustic vibrations at the transducer surface into low-level electrical signals. Specifics of this conversion are highly dependent on transducer design parameters, with transducer array implementations conforming to the desired measurement application.

For insonation of the MCA through the temporal acoustic window (TAW), a maximum sample depth up to 70mm is required. From Equation 2.39, the maximum focal length $l_{f,\max}$ achievable is approximated by the transducer aperture transition distance z_r. To support focusing at greater insonation depths, a larger equivalent aperture is necessary.

In acoustic imaging applications, synthetic beamforming techniques – notably synthetic aperture sonography – rely on stationary media for focal superposition, which permits the time-multiplexing of transceiver electronics among multiple transducer elements. Doppler sonography applications, however, involve the characterization of scatterer motion, which significantly diminishes scene coherence between adjacent pulse transmissions and therefore greatly constrains the use of synthetic aperture beamformation and electronic channel multiplexing. Synthetic aperture velocity estimation has been demonstrated, but is limited in maximum sample volume and scatterer velocity and is therefore not considered in TCD sonography applications [93].

This work employs per transducer element transceiver electronics for a fully parallel and discretely practicable implementation of TCD sonography. Complexity of transceiver electronics, transducer cabling, and power dissipation in battery powered operation – among other concerns – therefore severely constrain transducer element count.

Operating at an acoustic frequency of 2MHz requires approximately 1024 transducer elements to satisfy grating lobe pitch limits – given in Equation 2.51 – and a desired maximum focal length $l_{f,\max} \approx 70\text{mm}$. Beamformation capabilities – particularly, steering angle magnitude, focal length, and element directivity – therefore yield conflicting requirements for minimization of transducer element count.

Limiting steering angle magnitude to $< 15°$ in both azimuth and elevation permits a 64 element (i.e., 8 by 8) two-dimensional transducer array with $L_x = L_y = 1.6\text{mm}$, $\text{kerf}_x = \text{kerf}_y = 0.1\text{mm}$, resulting in equivalent aperture dimensions $L_{x,eq} = L_{y,eq} = 13.5\text{mm}$, to achieve sufficient focal pressures for transtemporal insonation of the MCA.

At the steering angle limit of 15° and maximum focal length ($l_f = 70\text{mm}$), the steered aperture achieves focal pressure above that of an on-axis (i.e., manually steered) single element transducer – with 13mm diameter (circular) planar (unfocused) radiating surface, as commonly used in commercial TCD instrumentation [17, 23]. Although not imperative for the spectral envelope method described in

Section 4.2.1, relatively uniform vessel insonation is generally desired in velocimetry applications. For given equivalent aperture dimensions, half-power spot width ranges from 2 to 3.5mm over focal length extent, which is consistent with the expected MCA diameter of $\approx$ 3mm.

Figure 5-2 displays the relative acoustic pressure envelope of the phased array and single element apertures for fixed acoustic output power.

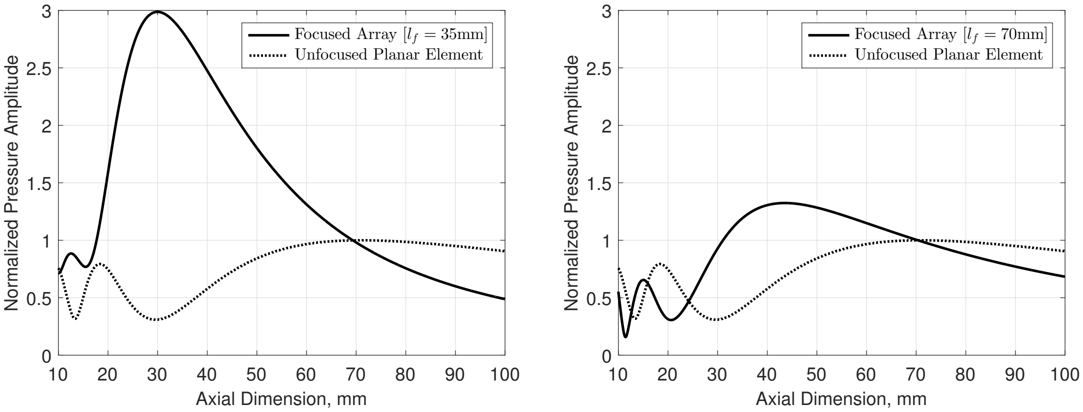

(a) Array focal length $l_f = 35$mm and steering angle $\phi_x = 0°$.

(b) Array focal length $l_f = 70$mm and steering angle $\phi_x = 15°$.

Figure 5-2: Comparison of acoustic pressure envelope for focused phased array and unfocused planar element apertures.

As predicted by acoustic theory, notably Equations 2.38 and 2.37, phased array operation yields reduced focal pressures at off-axis steering angles – due largely to limited element directivity – and increased focal lengths – due largely to limited focal gain. By restricting operation to modest steering angles (i.e., $|\phi_x|, |\phi_y| < 15°$), the prototype system provides decreased robustness to anatomic variation – particularly regarding positioning of the acoustic window relative to the underlying cerebrovasculature. However, maintaining realistic bounds on discrete hardware complexity facilitates *in vivo* human validation of the concepts presented in this work – albeit in a subset population.

Designed transducer array dimensions do not satisfy the grating lobe inequalities given in Equations 2.49 and 2.50. Therefore, the emergence of grating lobes is anticipated, as observed in the simulated results presented in Figure 5-3. The existence of grating lobes produces spatial aliasing that may alter perceived volumetric position and combine backscattering from multiple regions at the same depth. These effects, however, have minimal influence on the accuracy of MCA spectral envelope generation when the MCA is the dominant source of positive volumetric flow within the sample volume. Such nonidealities in phased array beamformation will, nonetheless, increase system dynamic range and clutter filter requirements – due to additional received spectral energy from stationary scatterers.

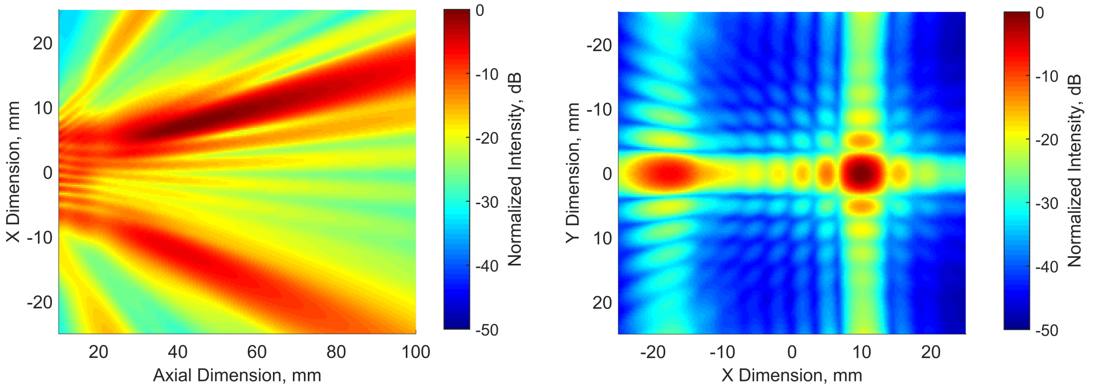

(a) Intensity variation in the xz-plane at $y = 0$mm.

(b) Intensity variation in the xy-plane at $z = 60$mm.

Figure 5-3: Simulated intensity beam pattern in the xy and xz-planes for the designed 64 element transducer array with an intended $(10, 0, 60)$mm focus.

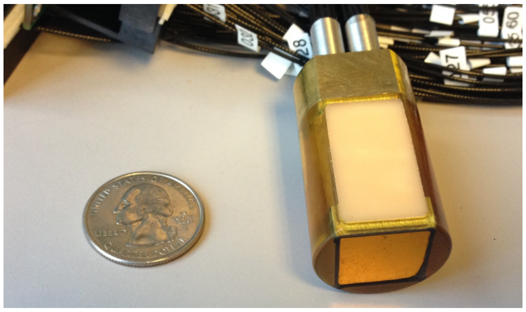

Figure 5-4: Custom two-dimensional transducer array for TCD instrumentation.

A custom two-dimensional 64 (i.e., 8 by 8) element ultrasound transducer array was fabricated (XDR055, Sonic Concepts, Bothell, WA) according to the preceding design parameters. The transducer array is shown in Figure 5-4, with array enclosure dimensions of 2.5cm in diameter and 4.5cm in height.

5.3 Electrical Hardware Implementation

The discrete prototype electrical hardware consists of interconnected circuit subsystems, which are classified as:

- Power management and high voltage (HV) supply generation circuits
- Ultrasound transceiver (XCVR) and control circuits
- Field programmable gate array (FPGA)
- Microcontroller (MCU)
- Data storage and memory
- Communication interfaces
- Clock generation and management circuits

5.3.1 Power Management

The power management and HV supply generation circuity consist of a set of linear and switching regulators. The linear regulators, TPS73701, TL1963A, LM2991SX, TPS7A4701, TPS7A3301 (Texas Instruments, Dallas, TX), and MAX6126BASA25 (Maxim Integrated, San Jose, CA), are used to provide filtered, low-noise, and stable operating voltages to electrical components. Analog components supplied by the linear regulator outputs generally provide significant power supply rejection ratio (PSRR) and power supply modulation ratio (PSMR) – on the order of > 40dB. Therefore, moderate supply noise and spurious content can be accommodated with minimal effect on system performance. Switched level implementation of the transmit pulsers (i.e., explicit switching of the transmit node to the HV supply rails), however, directly amplitude modulates HV supply noise into the signal path. Proper regulation and filtering of the HV power supply rails (i.e., HVP and HVN) is therefore critical to the realization of high signal-to-noise and distortion ratio (SNDR) system operation.

Switching regulators – LM2588SX, TPS54821, LM21215, and LM25576 (Texas Instruments, Dallas, TX) – are used to increase supply voltages, invert supply voltages, and power efficiently convert to reduced supply voltages. Digital potentiometers AD5248 and AD5245 (Analog Devices, Norwood, MA) in the HV regulator feedback paths enable digitally adjustable control of bipolar HV output levels according to measurement conditions and predetermined transducer dependent acoustic limits.

Nominal switching regulator operating frequencies are selected to minimize fundamental and harmonic spectral content in the analog frequency band of interest ($\approx 1.8 - 2.2$MHz). Switching regulator designs also support frequency synchronization from a common clock. Power connections into to the power management subsystem require a single 12 to 17V (nominally 14.8V) source, facilitating battery powered operation.

A block diagram of the power management subsystem is given in Figure 5-5.

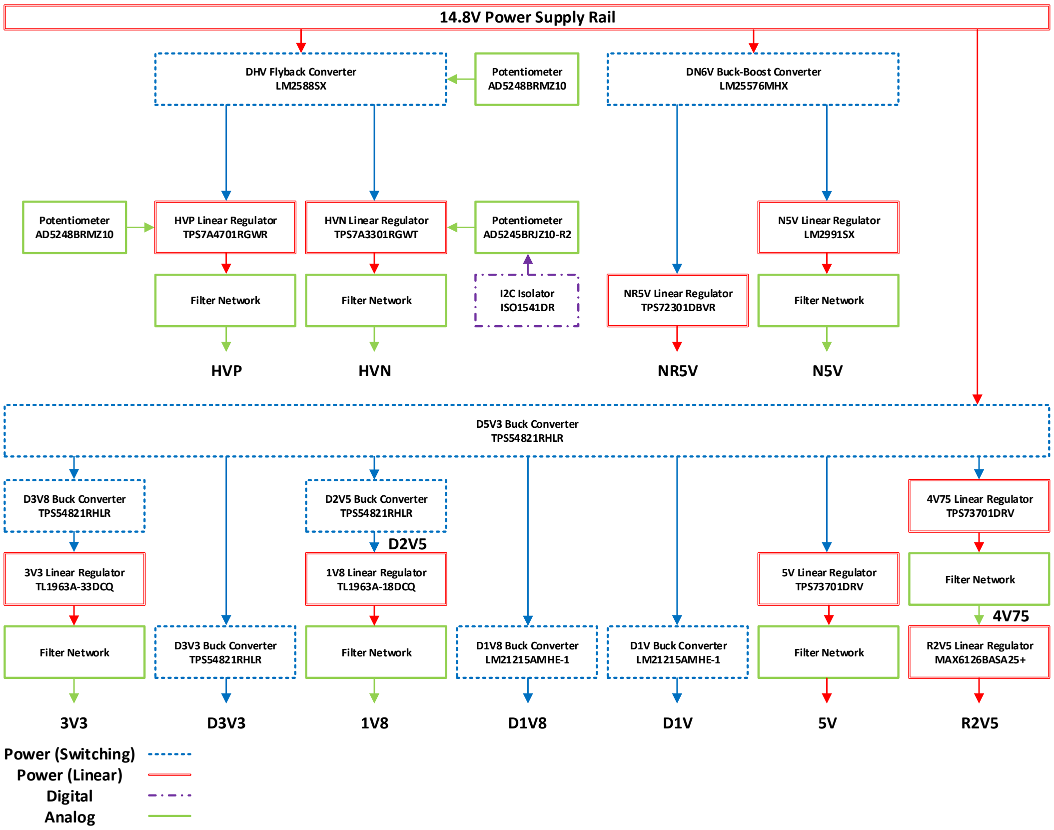

Figure 5-5: Discrete phased array power management subsystem.

5.3.2 Ultrasound Transceivers

A set of octal ultrasound transceivers (MAX2082, Maxim Integrated, San Jose, CA) provides 64 channels of HV pulsers on transmit and 64 channels of transmit/receive (T/R) switches, low-noise amplifiers (LNAs), variable gain amplifiers (VGAs), anti-aliasing filters (AAFs), and analog-to-digital converters (ADCs) on receive. The HV pulsers level shift digital excitation pulses from the FPGA output level to the HV supply rails (i.e., HVP and HVN). These HV excitation waveforms are the electrical driving signals for the ultrasound transducer array. Within the transducer array, each element is connected to an independent HV pulser channel. The piezoelectric transducer elements convert HV transmit pulses into acoustic energy, which is radiated into the propagating medium. During transmit, the T/R switches – one per transducer element – are open to protect sensitive receive electronics from HV pulser signals.

During receive mode, acoustic energy is converted into a low-level electrical signal at each transducer element. The T/R switches close, providing a low impedance path to receiver electronics. LNA gain, filtering bandwidth, and ADC parameters are configured for application specific functionality via a serial peripheral interface (SPI) bus from the MCU. Analog gain blocks, specifically the LNA and VGA, help to limit noise contributions – attaining a cascaded noise figure of 4dB – and realize sufficient signal levels prior to digitization. Low-pass filtering in the AAF attenuates high frequency noise and interferers such that frequency aliasing is minimized during data conversion. ADCs transform analog signals into a 12-bit serialized low-voltage differential signaling (LVDS) waveform for each channel. Serialized LVDS bitstreams are transferred to the FPGA for further processing.

For single channel operation, a signal-to-quantization noise ratio (SQNR) of $\approx$ 70dB is expected. Correlation of quantization noise between channels is dependent on channel-to-channel signal correlation. A common underlying acoustic energy distribution defines the analog input to all channels of receiver electronics, receive waveforms – and thereby quantization noise – are therefore expected to be highly correlated between channels. Thermal noise generated during energy transduction and analog processing (i.e., amplification, filtering) is expected to be largely uncorrelated between channels.

Auxiliary gain control circuitry enables a wide range system gains, from 0 to +45dB; VGA gain is set through a differential control voltage. Digital adjustment of VGA gain – via an SPI bus from the MCU – is achieved using a digital-to-analog converter (MAX5214, Maxim Integrated, San Jose, CA) and op-amp (MAX4477AUA, Maxim Integrated, San Jose, CA) based single-ended to differential translation circuit.

5.3.3 Field Programmable Gate Array

The FPGA (XC7A200T-1FFG1156C, Xilinx, San Jose, CA) acts as an embedded processing and control unit within the TCD ultrasound system. Pulse excitation waveforms are generated in the FPGA transmit beamformer and relayed to the transmit pulsers. Following signal conditioning and digitization, echo data is received and deserialized by the FPGA. Receive beamforming is achieved in the FPGA via variable length delay buffers and channel summation. Doppler signal processing is largely realized in the FPGA due to high input and intermediate (i.e., after delay and sum beamformation) data rates – >20Gb/s and >1Gb/s, respectively.

FPGA firmware is implemented using the Verilog hardware description language. A block diagram of the FPGA digital processing subsystem is given in Figure 5-6.

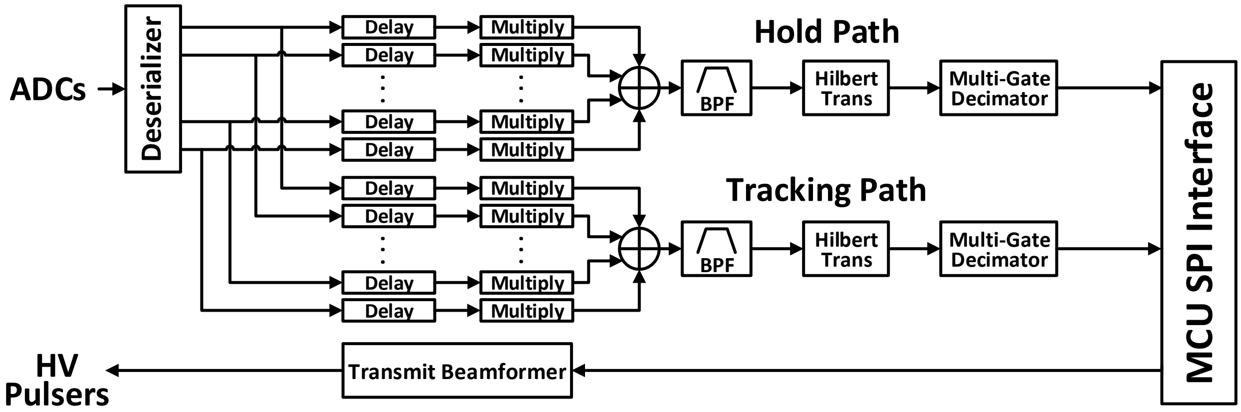

Figure 5-6: Discrete phased array digital processing subsystem.

Multiplier blocks permit receive apodization, but are used solely for programmable receive channel selection in this work. As discussed in Section 4.3.2, hold and tracking receive paths are defined to facilitate real-time vessel tracking. Multi-gate decimation for up to 8 range gates is employed to improve vessel search and tracking performance.

Following decimation, baseband data rates ($\sim$ 5Mb/s) are amenable to communication with the MCU. A SPI interface between the FPGA and MCU allows for sufficient bidirectional data transfer rates, up to 15Mb/s. A command interpreter is designed within the FPGA to decode SPI commands from the MCU and appropriately set operating coefficients within the transmit beamformer, delay, multiplier, and decimator modules. Data transfer commands received by the FPGA initiate memory buffer reading within the SPI interface module and output baseband data to the MCU. FPGA and MCU timing domains are connected using a first-in, first-out (FIFO) memory structure with independent write and read clock domains.

5.3.4 Microcontroller

The MCU (LPC4357, NXP, Eindhoven, Netherlands) acts as a high-level controller for the embedded system, determining acoustic focal points and beam steering coefficients, configuration settings (e.g., HV power supply level, transmit pulser current limits, VGA gain control, switching regulator operating frequencies), and modes of operation. MCU firmware is implemented in the C programming language and utilizes the LPCOpen driver libraries.

Processing of baseband Doppler data – including clutter reject filtering, Fourier transformation, spectral envelope generation, and Doppler power ratio computation – is divided between the embedded MCU and a remote host (i.e., server or personal computer). During development, raw data is generally transferred to the remote host for post-processing and algorithm refinement. As processing implementations become stable, embedded computation is expanded and data transfer rates to the remote host are reduced. To achieve sufficient data throughput, the LPC4357 MCU contains an ARM Cortex-M4 central processing unit (CPU) for signal computations and an ARM Cortex-M0 coprocessor for data transfer and low-level input/output (I/O) operations.

An interface between the prototype system and a remote host is also necessary for real-time data display and operator control of the system. A command interpreter is implemented on the MCU to manage and respond to communication with the remote host.

5.3.5 Data Storage and Memory

Data from the MCU can be stored to volatile SDRAM (MT48LC4, Micron Technology, Boise, ID), non-volatile flash memory (S25FL256S, Spansion, Sunnyvale, CA), or a removable secure digital (SD) memory card. Additionally, the MCU contains both SRAM (136kB) and flash memory (1MB). During typical operating modes, data is output to a remote host for display and is stored in the host system. For such streaming modes, on-board SRAM and SDRAM provide adequate bandwidth and data capacity to achieve real-time operation. Future modes of operation – such as exclusion of the remote host and embedded data capture – can utilize the on-board large capacity SD memory format.

Additional flash memory (N25Q128, Micron Technology, Boise, ID) is required to store the FPGA binary file. During system initialization, the FPGA loads its configuration settings from the non-volatile flash memory. Firmware updates are achieved by overwriting the MCU and FPGA flash memories through separate programming interfaces.

5.3.6 Communication Interfaces

Communication between hardware subsystems spans a wide range of complexity and throughput. Low-level control of components is achieved using inter-integrated circuit (I2C), universal asynchronous receiver/transmitter (UART), and SPI buses. As detailed in Section 5.3.3, an application specific SPI bus achieves sufficient bidirectional transfer of operating coefficients and baseband data between the FPGA and MCU.

A high-speed USB 2.0 interface exists between the MCU and remote host, which supports data rates over 50Mb/s. During development, this interface enables raw data capture at the remote host – although requiring a wired interface.

For expanded functionality, a wireless Bluetooth low energy (BLE) interface (CC2541, Texas Instruments, Dallas, TX) is also provided for communication to a remote host or mobile device. Because the BLE interface supports significantly lower data rates ($\leq$ 2Mb/s), complete embedded processing is required to reduce data rates to acceptable levels. Wireless data transfer is necessary for fully portable operation.

5.3.7 Clock Generation and Management Circuits

Phase noise performance is critically important in PW Doppler systems. The presence of excessive phase noise results in spectral spreading of high-level tones from stationary scatterers, thereby obscuring low-level spectral energy (generally < -50dBc) from moving scatterers. Phase noise – and its integrated representation, jitter – are often dominated by clock generation and distribution circuitry.

Jitter is largely introduced into the system presented in Figure 5-1 at the ADC sampling clock and transmit pulse generation clock. Root mean square (RMS) jitter – generally the parameter of interest – accumulates, to first order, as the root sum square of component jitter sources in a cascade. System clock management must therefore minimize the largest contributing jitter sources and number of significant jitter sources.

The clock distribution scheme – presented in Figure 5-7 – originates at a 32MHz crystal oscillator (ASFL3-32.000MHZ, Abracon, Irvine, CA), which generates the underlying ADC sampling clock. The sampling clock path also contains a clock distribution buffer (Si5330F-B00216, Silicon Labs, Austin, TX) to reduce clock loading and skew between channels. Additional clocks (e.g., SPI interface clock, USB clock) are generated within the FPGA or MCU via phase-locked loops (PLLs) and clock divider logic.

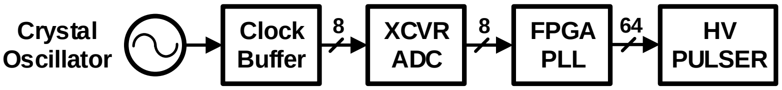

Figure 5-7: Clock generation and distribution subsystem.

For pulse-echo operation, the receive signal contains jitter contributions from both transmit pulsing and receiver sampling. Inclusion of FPGA logic in the signal path generally severely degrades jitter performance. However, separate clock routing structures in modern FPGAs can lead to tolerable jitter I/O values. Analysis of the pulse-echo signal path results in RMS jitter $t_J \approx 30\text{ps}$. Absolute frequency error and clock drift have limited impact on system performance – since transmission and reception timing are derived from a common clock source.

Total RMS jitter results in an upper bound on realizable carrier signal-to-noise ratio (SNR_c), defined in Equation 5.1.

$$\text{SNR}_{\text{c,max}} = 20\log\left(\frac{1}{2\pi f_{\text{max}} t_J}\right) \tag{5.1}$$

where f_{max} is the maximum spectral tone present. For the clock generation presented, this yields $\text{SNR}_{\text{c,max}} = 68\text{dBc}$ – where dBc emphasizes power level relative to a carrier spectral tone (i.e., generally due to stationary tissue scattering). Although basic, the preceding analysis suggests that jitter performance may have a moderate – but limited – impact on system noise performance. Single channel operation is described in the preceding analysis. Correlation of jitter sources between channels is expected due to a single PLL employed within the FPGA, but differences in routing and sensitivity to switching noise is not easily assessed.

5.4 System Integration

Electrical hardware is interconnected on a 10 layer printed circuit board (PCB) with dimensions of 16.5 x 14.5 x 2.5cm. The custom two-dimensional transducer array is connected to the PCB via coaxial cabling, shown in Figure 5-8(a).

The electrical hardware PCB is housed in a plastic enclosure – with dimensions of 18 x 16 x 7 cm – that prevents contact to any electrical signal by the operator and measurement subject. For wearable operation, the system electronics enclosure includes a harness and is worn at the chest. The enclosure also incorporates a battery pack (Li-ion 18650 14.8V pack, AA Portable Power Corp, Richmond, CA) compartment. The wearable TCD instrumentation system is presented in Figure 5-8(b).

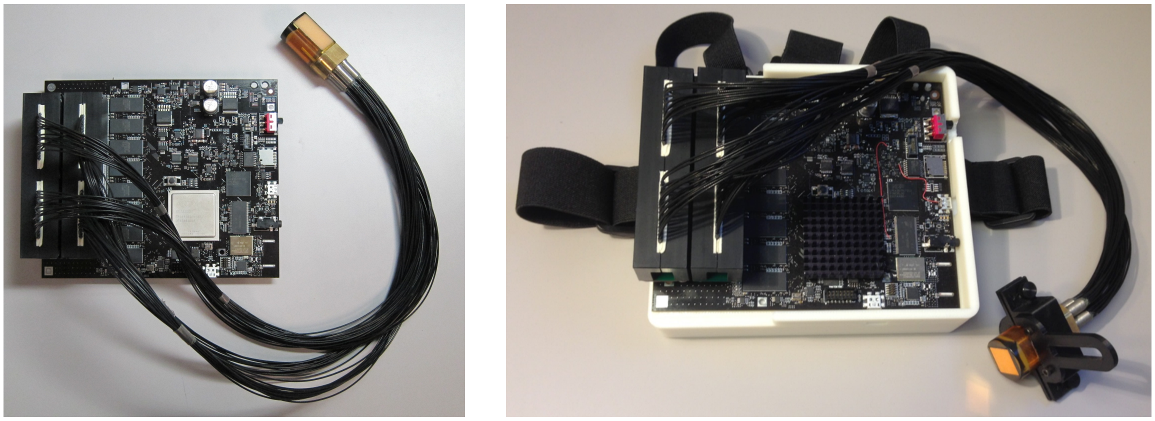

(a) Electrical hardware and custom transducer array.

(b) Wearable prototype system.

Figure 5-8: Discrete phased array prototype system hardware (with plastic enclosure lid removed).

The transducer array is affixed to the measurement subject using a headframe and translation stage, as shown in Figure 5-9.

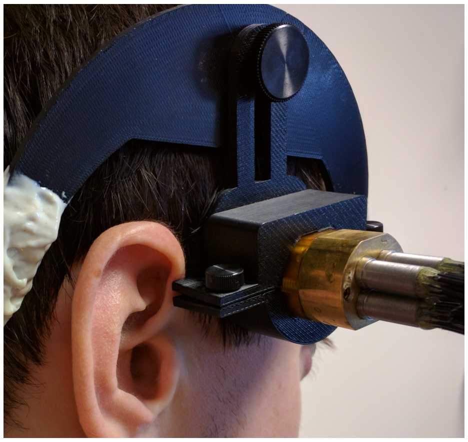

Figure 5-9: Headframe with transducer array translation stage.

5.5 Summary

This chapter introduces a discrete phased array system architecture for TCD velocimetry applications. A custom two-dimensional transducer array is designed to support insonation of the MCA through the TAW at azimuth and elevation steering angle magnitudes $< 15°$. Implementation of electrical hardware supports 64 channels of digital transmit and receive beamformation, untethered (i.e., wireless, battery powered) operation, and is realized in a compact form factor. A wearable prototype system with electrical hardware and battery enclosure, headframe, and transducer array translation stage is presented.

Chapter 6

Discrete Phased Array System Characterization

Although theoretical analysis and simulations are crucial during the design process, experimentation is needed to characterize and validate the electrical and acoustic performance of prototype TCD instrumentation. Specifically, the discrete phased array system described in Sections 5.2 and 5.3 will be experimentally evaluated. The transmit and receive signal paths are initially assessed separately. Functionality and accuracy of the TCD sonography system are then characterized for pulse-echo operation by employing a water tank and Doppler flow phantom.

6.1 Transducer Electrical Characterization

The Butterworth Van-Dyke (BVD) model, presented in Figure 6-1, is used to characterize the operation of a piezoelectric transducer near resonance, where C_0 is a parasitic electrical capacitance and C_m, L_m, and R_m model the motional impedance of piezoelectric resonance [94].

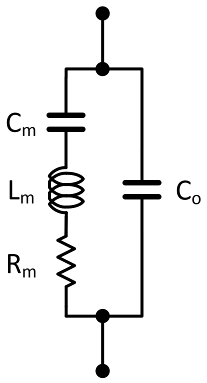

Figure 6-1: Butterworth Van-Dyke (BVD) lumped element circuit model.

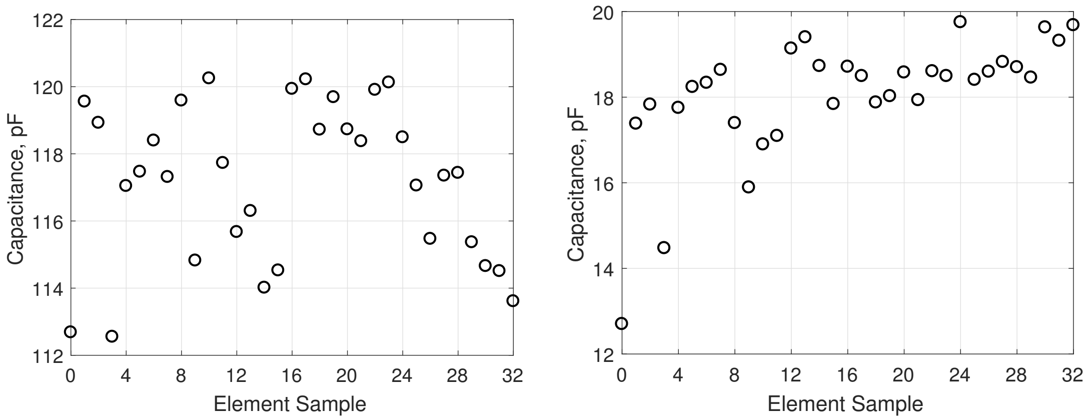

(a) Extracted parasitic capacitance C_0.

(b) Extracted motional capacitance C_m.

Figure 6-2: Transducer element extracted BVD capacitances.

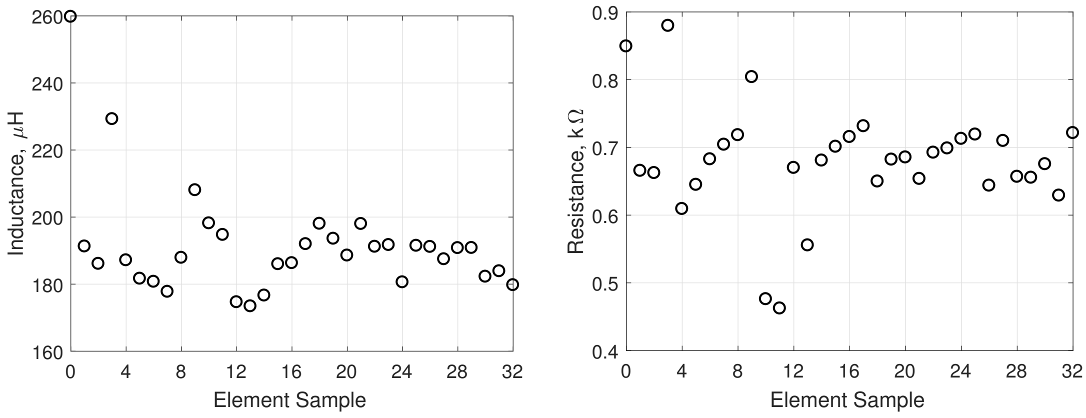

(a) Extracted motional inductance L_m.

(b) Extracted motional resistance R_m.

Figure 6-3: Transducer element extracted BVD motional inductance and resistance.

Using electrical impedance measurements – in a water medium – and least-squares numerical fitting, the BVD element model parameters can be extracted for each physical element in the transducer array – including coaxial cable loading. Figure 6-2 displays the extracted electrical parasitic and motional capacitance values for 32 elements in the two-dimensional transducer array. Measured elements are randomly chosen among two different physical arrays, with element samples 1 through 16 corresponding to unit XDR055-007 and element samples 17 through 32 corresponding to unit XDR055-008. Similarly, Figure 6-3 displays the extracted motional inductance and resistance values.

For measured transducer elements, model parameter values were moderately consistent. Statistical characterization of the extracted BVD model parameters yields:

$$\begin{aligned} \mu_{C_0} &= 117\text{pF} & \sigma_{C_0} &= 2.3\text{pF} \\ \mu_{C_m} &= 18.1\text{pF} & \sigma_{C_m} &= 1.4\text{pF} \\ \mu_{L_m} &= 191\mu\text{H} & \sigma_{L_m} &= 16\mu\text{H} \\ \mu_{R_m} &= 679\Omega & \sigma_{R_m} &= 82\Omega \end{aligned}$$

Acoustic resonance occurs when the reactance of the motional inductance L_m and capacitance C_m are equal in magnitude. Resonant frequency f_0 and half-power bandwidth BW_{3dB} are given by Equations 6.1 and 6.2.

$$f_0 = \frac{1}{2\pi\sqrt{L_m C_m}} \tag{6.1}$$

$$BW_{3dB} = \frac{R_m}{2\pi L_m} \tag{6.2}$$

Variation of resonant frequency and half-power bandwidth are shown for measured transducer elements in Figure 6-4. Statistical characterization of the extracted frequency parameters yields:

$$\begin{aligned} \mu_{f_0} &= 2.7\text{MHz} & \sigma_{f_0} &= 45\text{kHz} \\ \mu_{BW_{3dB}} &= 566\text{kHz} & \sigma_{BW_{3dB}} &= 60\text{kHz} \end{aligned}$$

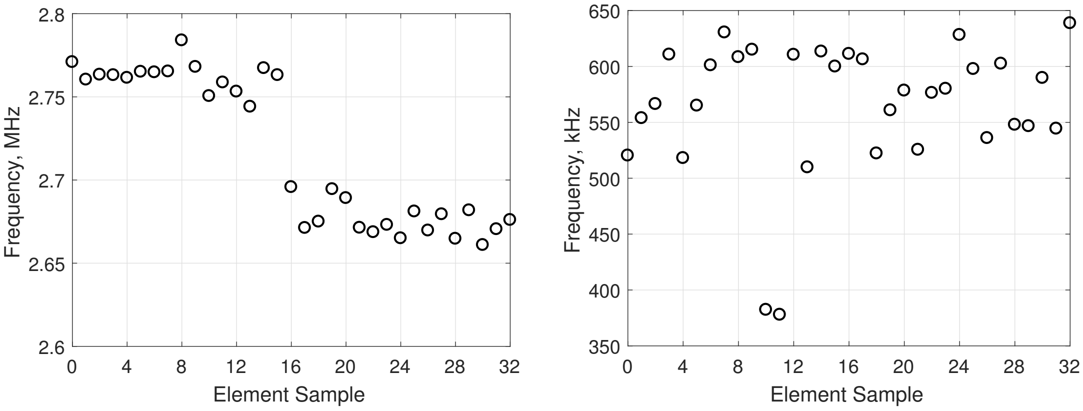

(a) Extracted resonant frequency f_0.

(b) Extracted half-power bandwidth BW_{3dB}.

Figure 6-4: Transducer element frequency characteristics.

Figure 6-5 compares the transducer element impedance magnitude for measured and extracted BVD model data. Agreement between measured data and the BVD model is observed.

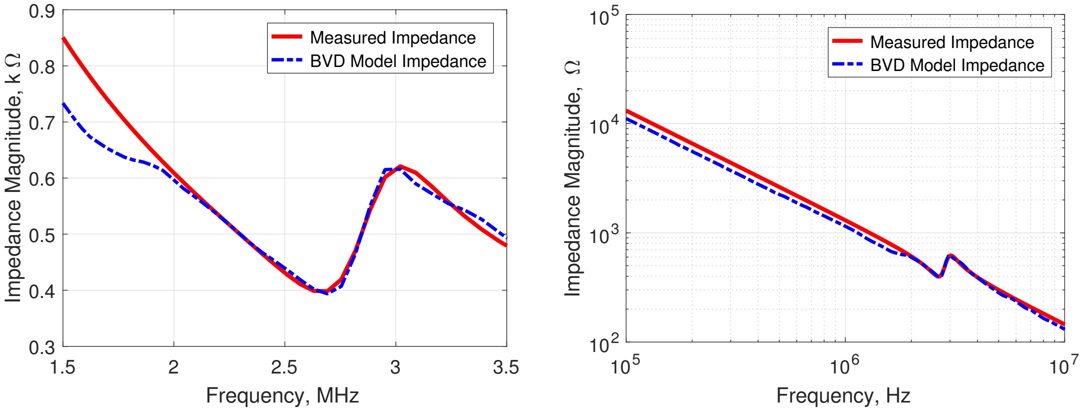

(a) Impedance near resonance.

(b) Wideband impedance.

Figure 6-5: Comparison of measured and extracted BVD model transducer element impedance.

Incorporating the effect of transceiver interface impedance, a normalized receive transfer function magnitude $|H_{RX}|$ is shown in Figure 6-6. For the frequencies of interest (i.e., $\approx$ 1.8 – 2.2MHz) and assuming single resonance, this results in signal attenuation of roughly 6dB relative to operation near the resonant frequency ($\approx$ 2.7MHz) – yielding considerable degradation in received signal level. The observed deviation in resonant frequency from the specified 2MHz value is presumably the result of improper consideration of acoustic loading effects – that is, air versus water acoustic media properties – during fabrication. Although nonideal, acceptable operation for TCD sonography applications is nevertheless achievable.

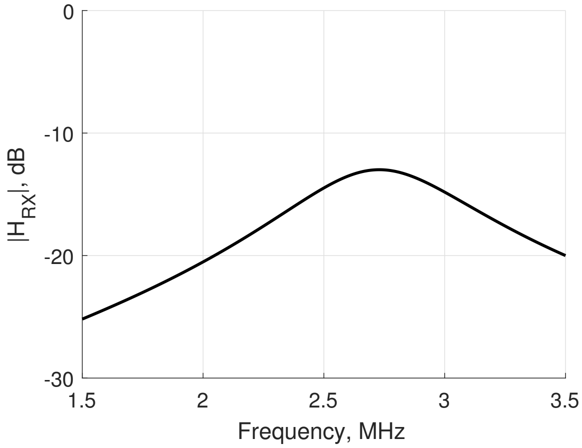

Figure 6-6: Normalized receive transfer function magnitude for extracted BVD model transducer element with single resonant frequency.

6.2 Electrical Hardware Characterization

6.2.1 Power Management

Although mode dependent, power dissipation of the prototype TCD system is ∼20W during typical operation, resulting in maximum battery powered operation of about 90 minutes. Power dissipation among electrical hardware subsystems is given in Figure 6-7 – where analog front-end (AFE) includes the transmit/receive (T/R) switch, low-noise amplifier (LNA), variable gain amplifier (VGA), and anti-aliasing filter (AAF). Digital power is largely dissipated by the field-programmable gate array (FPGA) and microcontroller (MCU).

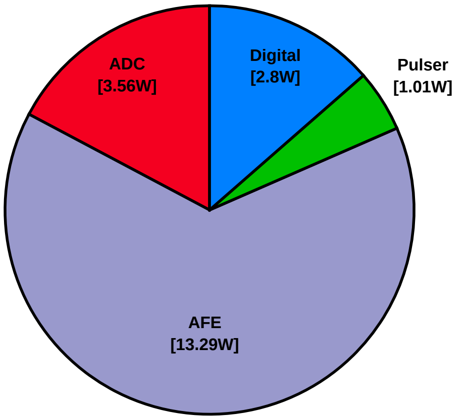

Figure 6-7: Discrete phased array system power dissipation.

Digital control of high-voltage (HV) power supply generation from ±6V to ±25V is demonstrated in Figure 6-8. A minimum dropout voltage of 1.5V is maintained over the entire range of HV supply settings to improve power supply rejection for HV linear regulation.

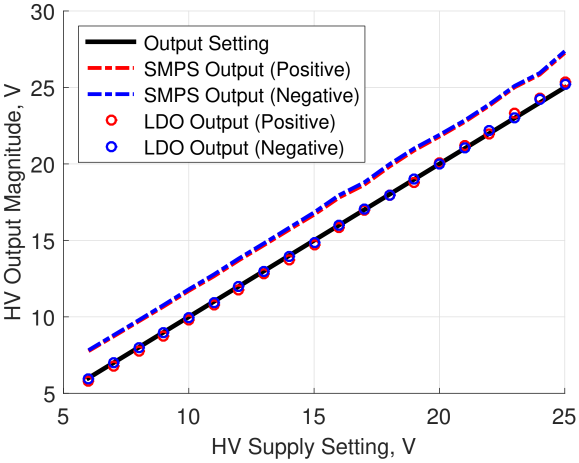

Figure 6-8: HV power supply rail digital control.

Despite consideration of free-running switching regulator operation, appreciable baseband spectral energy – presumably due to nonlinear mixing of multiple independent switching frequencies – severely degrades system operation. Through supply synchronization via division of the underlying ADC sampling clock, spurious content accumulates as a DC offset and is therefore attenuated by the clutter reject filter. Compared to free-running switching regulation, implementation of synchronous supply switching decreases integrated noise and distortion power by 37dB and reduces the spurious-free noise floor by 50dB – as shown in Figure 6-9.

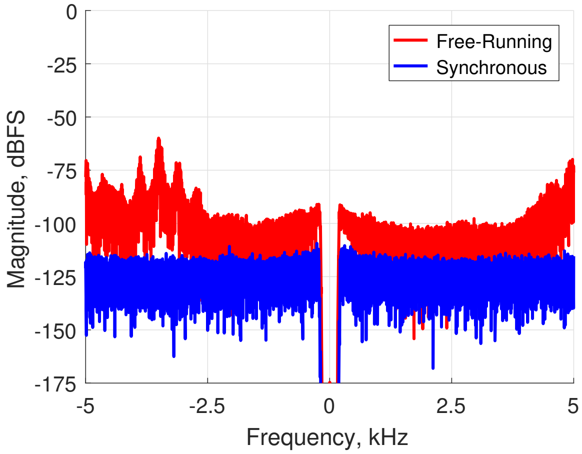

Figure 6-9: Effect of switching regulator synchronization on baseband receive spectra.

6.2.2 Receive Path

An excitation frequency f_e of 2MHz with six cycle gate period (i.e., $M = 6$), results in a matched radio frequency (RF) bandpass filter (BPF) bandwidth of $BW_{BPF,3dB} = \frac{f_e}{M} \approx$ 350kHz. Although the presence of interferers can be detrimental to Doppler velocimetry accuracy, interferers occurring outside the bandwidth of the matched BPF are highly attenuated and – assuming receiver saturation is avoided – have minimal effect on system performance. The RF BPF impulse response can be modified to further attenuate interferers by realizing higher order filtering.

The receive signal spectrum is given in Figure 6-10 for a -3dBFS (i.e., 3mV amplitude for +45dB gain) sinusoidal input – with pulsing disabled and fixed low impedance T/R switching. Integration of noise and distortion power over the BPF bandwidth yields a carrier signal-to-noise and distortion ratio (SNDR_c) of 62dBFS – significantly lower than implied for 12-bit quantization and suggesting AFE output noise degradation at high analog gain.

In this text, dBc designates spectral power relative to a specific carrier signal and dBFS designates spectral power relative to a full-scale carrier tone. Values of SNDR_c and spurious-free dynamic range (SFDR_c) can be quantified in units of dBFS and dBc and physically pertain to the relative power of high-level carrier tones – from stationary scatterers, known as clutter – to noise power. Backscattered Doppler power from moving scatterers is generally < -50dBc relative to these high-level carrier tones. In constrast, values of system signal-to-noise ratio (SNR) quantify the relationship between integrated Doppler power – due to moving scatterers – and integrated noise power. System SNR during flow velocimetry is therefore typically several orders of magnitude less than $\mathrm{SNDR_c}$ measurements.

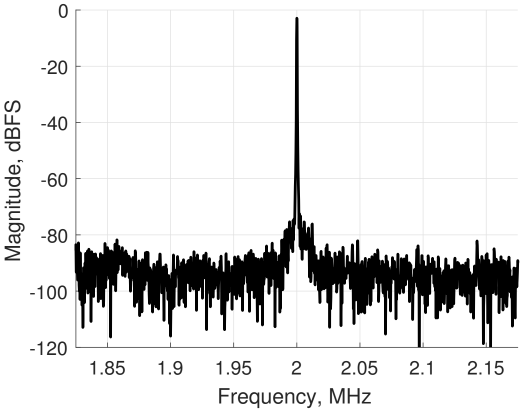

Figure 6-10: Single channel receiver frequency spectrum for a -3dBFS amplitude, 2MHz frequency sinusoidal input.

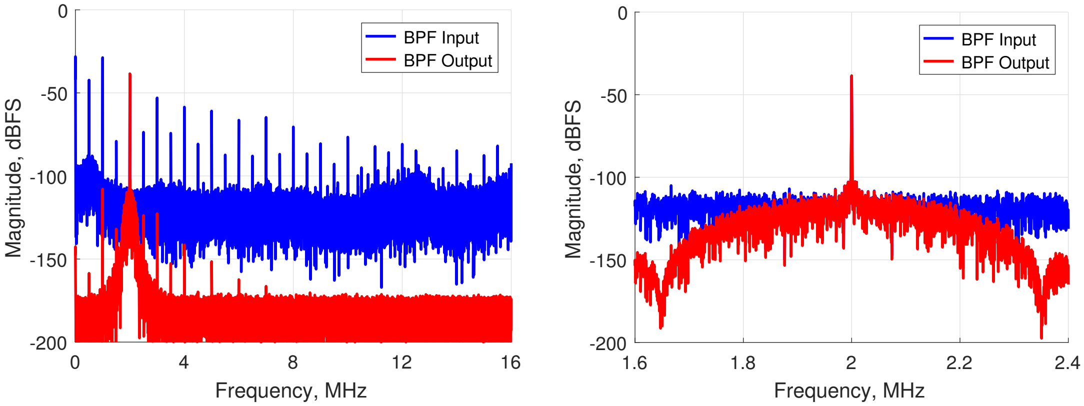

(a) Nyquist frequency spectrum.

(b) RF filter bandwidth spectrum.

Figure 6-11: RF receive beamformation frequency spectra for a -3dBFS amplitude, 2MHz sinusoidal single channel input.

Following receive beamformation, a single channel -3dBFS input signal yields a combined signal power of -39dBFS – due to 36dB beamformer gain for 64 channel operation. Figure 6-11 presents the combined RF spectrum and demonstrates satisfactory BPF performance – resulting in > 60dB rejection of out-of-band interferers. Spectral integration of the filter output over Nyquist-band yields an SNDR_c of 87dBFS (i.e., 51dBc), which has been established as adequate in commercial TCD sonography systems [17].

Validation of analog gain control via digital-to-analog converter (DAC) output to differential voltage translation is shown in Figure 6-12. For fixed LNA gain of 18.5dB, total AFE gain is adjustable from +5dB to +45dB – yielding 40dB of gain control.

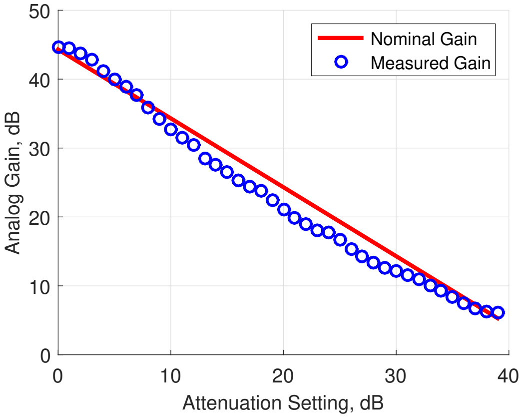

Figure 6-12: Discrete phased array system AFE gain control.

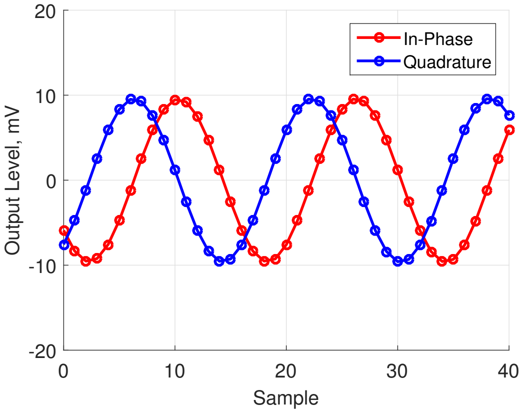

Figure 6-13: Discrete phased array system Hilbert transform delay.

Functionality of the Hilbert transform implementation is demonstrated in Figure 6-13. For a 2MHz sinusoidal input, Fourier analysis of the Hilbert transform output yielded $< 0.001°$ deviation from the nominal 90° phase shift. Accurate realization of the Hilbert transform results in minimal spectral leakage within the analytical output signal.

Receive beamformer timing delay is assessed by comparing a variable delay output signal to a fixed (i.e., undelayed) reference. The receive beamformer supports delays up to 160 samples at a resolution of 31.25ns – due to the underlying 32MHz ADC sampling clock.

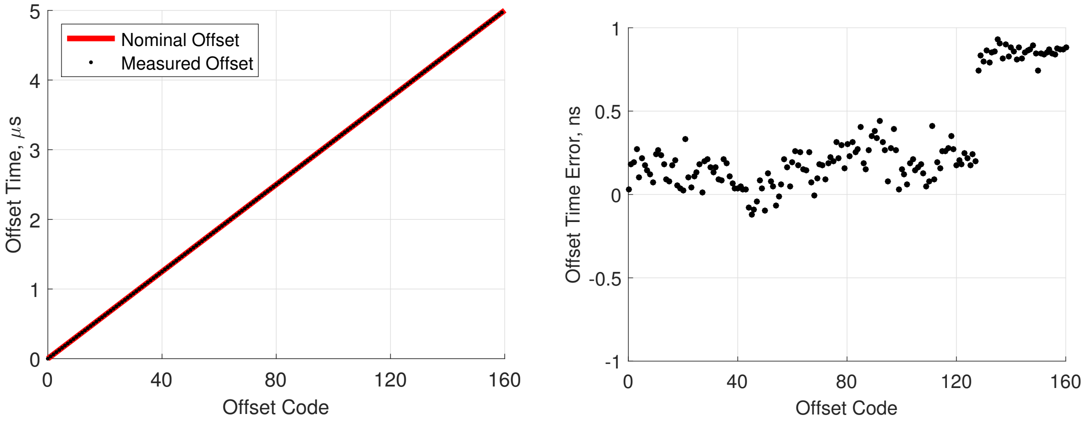

(a) Relative receive beamformer delay.

(b) Receive beamformer delay error.

Figure 6-14: Characterization of receive beamformer timing delay.

Offset codes 0 to 128 were measured by iterating through adjacent channel pairs. Offset codes 129 to 160 were measured between fixed channels with maximum separation (i.e., channels 1 and 64). Repeated measurements were highly consistent, suggesting root mean square (RMS) jitter less than the resolution of the measurement system ($\approx$ 100ps) – as concluded in Section 5.3.7. Timing errors are predominately due to printed circuit board (PCB) and FPGA routing skew. All measured delay errors were $<$ 5% delay resolution and therefore have negligible effect on system performance.

6.2.3 Transmit Path

Similarly, transmit beamformer timing delay is assessed by comparing a variable delay output signal to an undelayed reference. The transmit beamformer supports delays up to 160 samples at a resolution of 31.25ns.

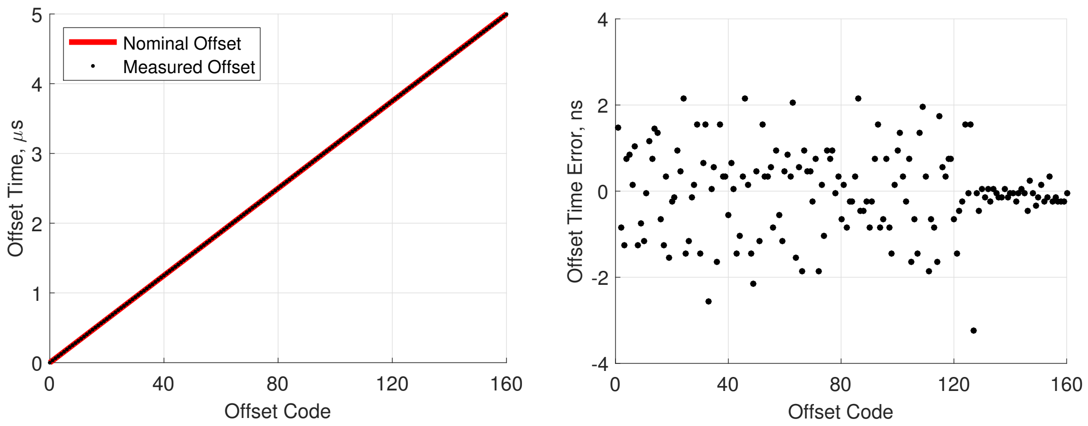

(a) Relative transmit beamformer delay. (b) Transmit beamformer delay error.

Figure 6-15: Transmit beamformer timing delay characterization.

Offset codes 0 to 128 were measured with a constant reference (channel 1) and iterating through all system channels. Offset codes 129 to 160 were measured between channels 1 and 2. As in Section 6.2.2, repeated measurements were highly consistent and suggest RMS jitter $<$ 100ps within the TCD sonography system. Timing errors are predominately due to PCB and FPGA routing skew. All measured delay errors were $<$ 10% delay resolution and therefore have minimal expected impact on system performance.

6.2.4 Pulse-Echo Operation

Pulse-echo operation is validated for the complete instrumentation system using a water tank and stationary acoustic reflector. Noise and distortion effects are most pronounced in pulse-echo operation, since numerous additional mechanisms exist – including Brownian motion associated with acoustic propagation and electromechanical transduction, pulser output noise, and interferer coupling. Figure 6-16 presents the baseband echo signal and resulting clutter reject high-pass filter (HPF) output.

Marked attenuation ($>$ 90dB) of the stationary echo data is achieved via clutter reject filtering. Integration of the baseband spectrum yields moderate $\mathrm{SNDR_c}$ of 70dBFS (i.e., 45dBc) and exceptional $\mathrm{SFDR_c}$ of $>$ 105dBFS (i.e., $>$ 80dBc).

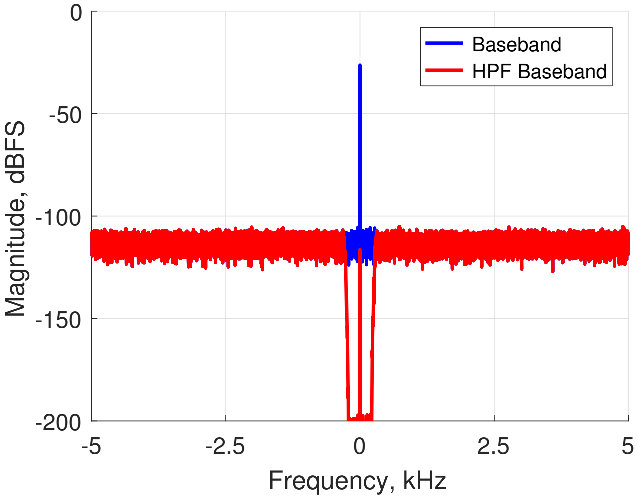

Figure 6-16: Baseband pulse-echo frequency spectra and clutter reject filtering.

Pulse-echo operation produced greater integrated baseband noise than initially predicted. Assuming noise generation is dominated by transducer element motional resistance and AFE electronics results in per channel AFE RMS output noise voltage of 400μV for 350kHz bandwidth, which yields SNDR_c of 70dBFS per channel and 88dBFS for the 64 channel system – assuming uncorrelated noise sources. Several explanations for these discrepancies are probable – including significant noise correlation between channels due to a common underlying transmit source, inadequate modeling of physical noise processes (i.e., acoustic propagation and transduction), insufficient power supply noise rejection, and signal attenuation due to off-resonance transducer operation. High spectral purity of the low frequency energy in Figure 6-13 is indicative that jitter related performance limitations are minimal.

6.3 Acoustic Characterization

By employing a hydrophone (HNC-0400, ONDA, Sunnyvale, CA) and preamplifier (AH-2010, ONDA, Sunnyvale, CA), acoustic pressures and their spatiotemporal dependence can be evaluated. A three-dimensional hydrophone translation stage and water tank with transducer bottom mount are utilized for experimental measurements, as shown in Figure 6-17.

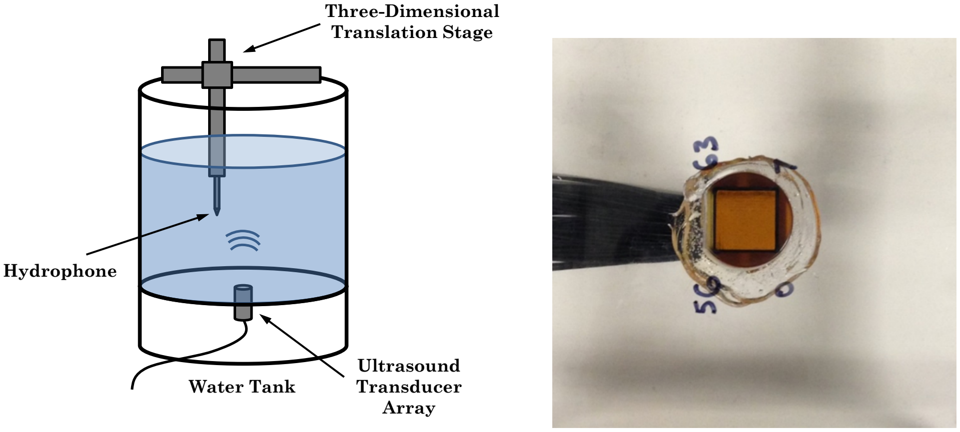

(a) Diagram of hydrophone setup. (b) Transducer array mount.

Figure 6-17: Hydrophone pressure measurement experimental setup.

Figure 6-18 displays the simulated and measured on-axis temporal-peak acoustic pressures for the transducer aperture during unfocused and focused operation. Focusing achieves a 5-fold increase in acoustic pressure at the focal point – compared to the unfocused pressure value. Pressure measurement trends agree well with simulation values and suggest correct implementation of transmit beamformation. In certain measurements, multiple hydrophone units are used to ensure measurement accuracy.

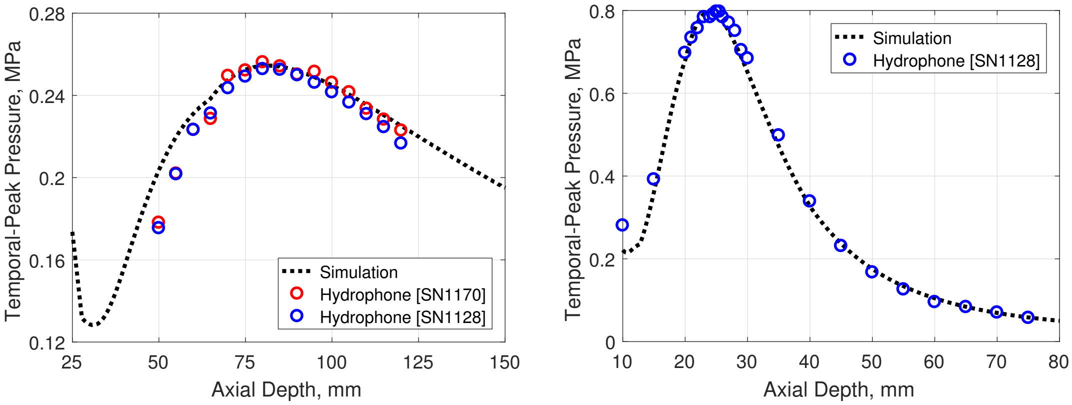

(a) Unfocused pressure. (b) Pressure with (0, 0, 25)mm focal point.

Figure 6-18: Variation of simulated and measured on-axis temporal-peak acoustic pressures for ±6V HV supply level.

Pressure magnitude at the last axial maximum p_{LAM} facilitates evaluation of temporal-average acoustic output power $P_{OUT,TA}$. For ±6V HV supply level, pulse repetition frequency $f_{PRF} = 10\text{kHz}$, and pulse duration $M = 6$ cycles, yields temporal-average acoustic output power $P_{OUT,TA} = 31\text{mW}$. From Section 3.2, these operating parameters result in a thermal cranial index (TIC) of 0.5 – well below upper TIC safe operating limit (TIC$<$ 2.0).

Assuming on-axis focusing yields maximal focal pressure, hydrophone testing facilitates assessment of spatial-peak-temporal-average intensity (I_{SPTA}) and mechanical index (MI). Using a standard derating factor of $0.3\text{dB} \cdot \text{cm}^{-1} \cdot \text{MHz}^{-1}$, Figure 6-19 presents on-axis I_{SPTA} and MI variation for focused operation.

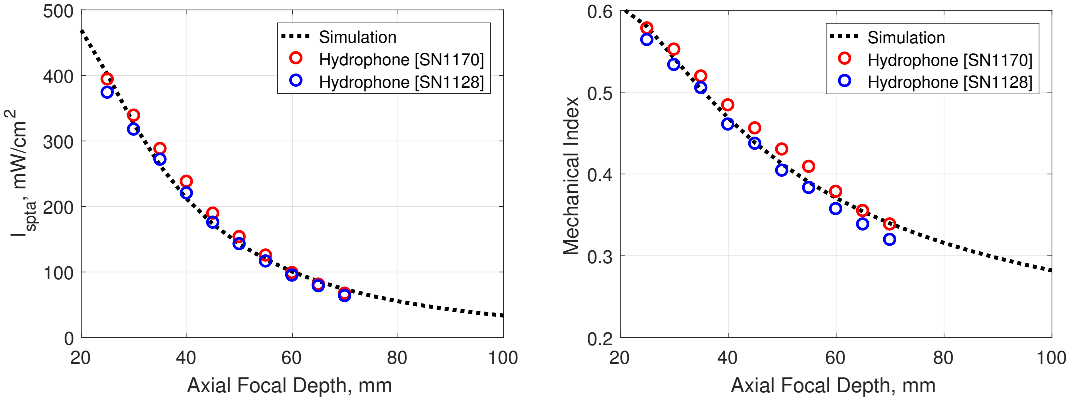

(a) Variation of I_{SPTA}.

(b) Variation of MI.

Figure 6-19: Comparison of simulated and measured on-axis I_{SPTA} and MI for ±6V HV supply level, $f_{PRF} = 10\text{kHz}$, $M = 6$ cycles.

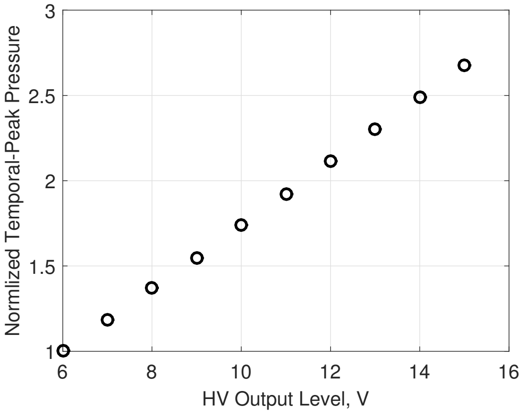

Figure 6-20: Dependence of HV supply level on normalized temporal-peak pressure.

Dependence of temporal-peak pressure on HV supply level is given in Figure 6-20. To maintain operation within acoustic safety limits, HV output level is limited to ±9V for focal depths > 35mm, $f_{PRF} = 10$kHz, and $M = 6$ cycles.

Hydrophone testing is also used to evaluated acoustic output pressure due to individually excited transducer elements. Figure 6-21 displays the on-axis temporal-peak pressure of 16 transducer elements. Measurement values yielded more gradual depth dependence than predicted by simulation, an effect likely due to adjacent element coupling under physical single element operation. In contrast, simulation data assumes a rigid baffle surrounding the radiating element. As established in Section 6.1, inter-element variation is reasonably moderate.

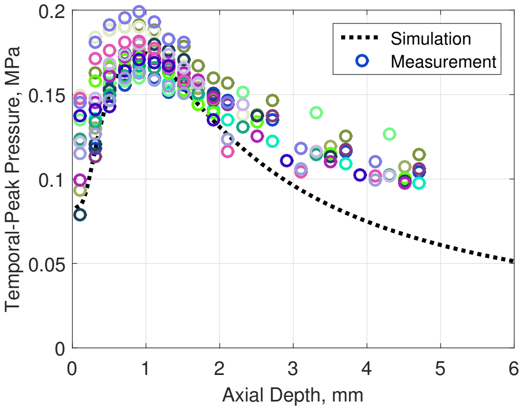

Figure 6-21: Variation of on-axis element temporal-peak pressure for ±6V HV supply level.

6.4 System Validation

6.4.1 Flow Velocimetry

Characterization of the instrumentation hardware and signal processing methods are experimentally validated for moving scatterers via flow phantom velocimetry. The experimental flow phantom setup is presented in Figure 6-22. Blood mimicking fluid is employed within the flow phantom to emulate the acoustic scattering properties of blood and is composed of water and 30μm diameter alumina powder particles (AP300-1, South Bay Technology, San Clemente, CA). The vessel phantom is constructed from

6.35mm inner diameter vinyl tubing. A diaphragm pump (4008-101-E65, Shurflo, Costa Mesa, CA) drives the blood mimicking fluid from the fluid reservoir through the flow phantom. A flow regulator is used to control the volumetric fluid flow, which is measured by an in-line flow meter (751021A08, King Instrument Company, Garden Grove, CA).

Uniform insonation of the vessel phantom can be ensured – due to visible transducer alignment and controlled vessel phantom course – and the Doppler angle and vessel phantom diameter accurately measured. Therefore, volumetric flow rate – or equivalently, mean flow velocity – can be used to determine the accuracy of the prototype TCD velocimetry system. Although *in vivo* blood flow is pulsatile in nature, the flow phantom setup of this work generates steady flow and thus prohibits evaluation of time-varying flow accuracy.

The fluid reservoir and diaphragm pump are open air systems and the blood mimicking fluid is not degassed. The flow phantom pumping action results in substantial generation of air bubbles, which likely dominate other scattering mechanisms. Therefore, due to a lack of cranial bone and increased backscattering, baseband signal levels under flow phantom testing are significantly higher ($\gtrsim$ 15dB) than expected *in vivo* levels. Nonetheless, the flow phantom is suitable for demonstrating functional system operation and validating Doppler velocity estimation techniques.

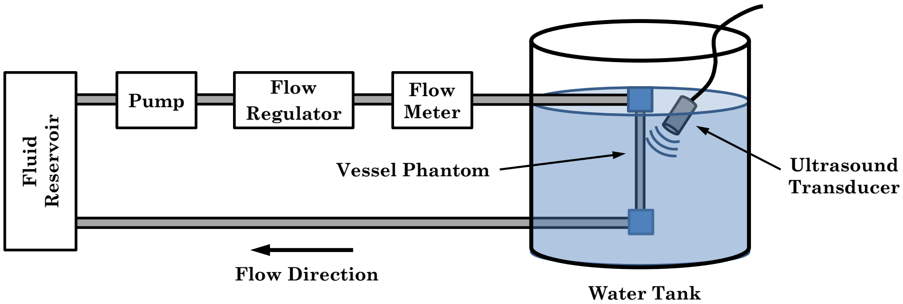

Figure 6-22: Experimental flow phantom setup for evaluation of sonographic velocimetry instrumentation [6].

Velocimetry accuracy is characterized by comparison of Doppler estimated mean flow velocities to flow meter measurements over the range of anticipated *in vivo* flow velocities in the MCA. From Figure 6-23, it is evident that Doppler mean velocity estimates are highly correlated to in-line flow meter data, which have been converted to mean velocities using known physical dimensions and measured Doppler angle. A 12th order Chebyshev HPF is used for clutter rejection with a stopband frequency corresponding to scatterer velocity of 4cm/s.

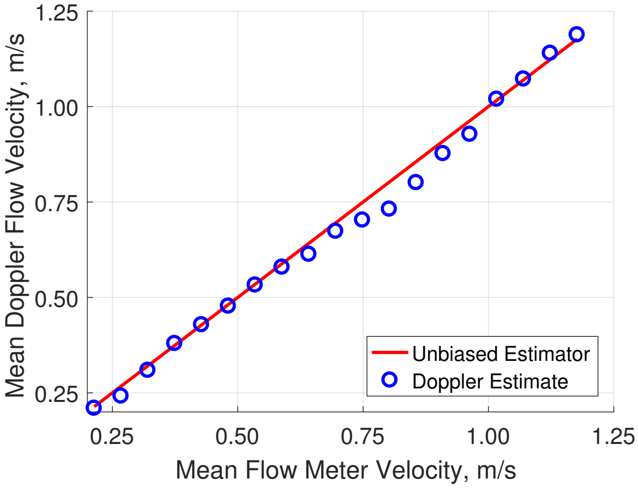

Figure 6-23: Comparison of Doppler estimated and flow meter evaluated mean flow velocities.

Normalized root-mean-square error (NRMSE) analysis is employed to assess estimator performance over the complete experimental data set, as given by:

$$NRMSE = \frac{1}{\bar{v}_{\text{obs,max}} - \bar{v}_{\text{obs,min}}} \cdot \sqrt{\frac{\sum_{i=1}^{n} \left(\bar{v}_{\text{est},i} - \bar{v}_{\text{obs},i}\right)^2}{n}} \tag{6.3}$$

where $\bar{v}_{\text{est}}$ is the Doppler estimated mean velocity at each data point, $\bar{v}_{\text{obs}}$ is the observed mean velocity obtained from flow meter data, and n is the number of experimental data points. For the given data set, NRMSE is equal to 2.95%.

Alternately, Doppler velocity estimation accuracy can be characterized using the difference parameter $\Delta\bar{v}_i = \bar{v}_{\text{est},i} - \bar{v}_{\text{obs},i}$. For the given data set, a difference mean of -1.7cm/s and difference standard deviation of 2.4cm/s were achieved. For the discrete prototype TCD system, the realized degree of measurement accuracy suggests clinically acceptable blood flow velocimetry [71].

6.5 Power Mode Doppler Signal Processing

The experimental flow phantom setup is also used to validate power mode Doppler operation – presented in Section 4.3. Figure 6-24 displays the baseband spectrum for a constant flow velocity measurement. The Doppler spectral pattern exhibited in Figure 6-24 characterizes the relative distribution of scatterer velocities – as discussed in Section 4.1.2.

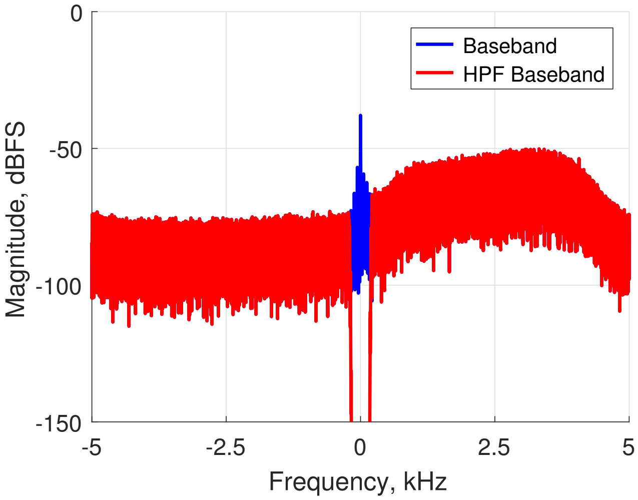

Figure 6-24: Flow phantom baseband frequency spectra and clutter reject filtering.

Analysis of the flow phantom baseband spectrum yields a Doppler power ratio P_{rel} of 21dB and resulting SNR of 18dB – considerably larger values than expected in human testing.

Validation of the Doppler power mapping technique can also be demonstrated via flow phantom testing. A dwell period of 192 samples (i.e., pulse repetitions) results in a Doppler mapping duration (i.e., coarse and fine search) of $\approx$ 15 seconds – including redundancy checks. Although interpretation of the Doppler mapping data is generally intended for algorithmic vessel localization, visualization of the coarse Doppler map – presented in Figure 6-25 – can reveal features of the underlying environment. For visual clarity, map intensity is normalized to the maximum P_{rel} value within the coarse Doppler map. Additionally, P_{rel} values below a specified percentile are set to transparent.

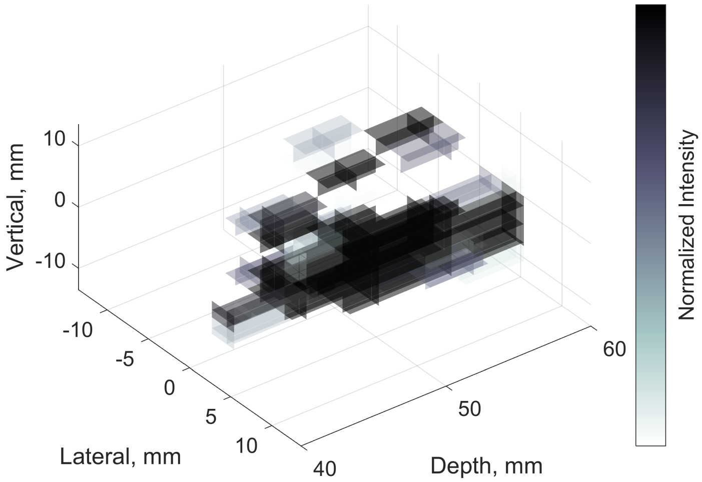

Figure 6-25: Flow phantom coarse Doppler power map.

From Figure 6-25, a contiguous, relatively straight region of elevated P_{rel} is observed – corresponding to the vessel phantom segment. As predicted, grating lobe generation yields spatial aliasing at steering angles negative to the flow region location, although at reduced intensity.

The flow phantom of this work does not support relative movement between the transducer array and vessel phantom. Doppler tracking procedures therefore were validated solely within the context of human subject testing.

6.6 Focal Correction

An acrylic reflecting layer is affixed to the flow phantom setup between the transducer array and flow region. The resulting heterogeneous media therefore facilitates validation of the focal correction methods presented in Section 4.4.

Each transducer element within the array is sequentially excited and the resulting single channel receive waveform post-processed – via bandpass filtering and Hilbert transform – to attain an amplitude mode (A-mode) scan line. Individual scan lines characterize the local degree (i.e., at each transducer element position) of acoustic scattering over axial depth. Further processing is employed to detect extrema along each scan line and thereby compute discontinuity locations within the propagating media, as displayed in Figure 6-26.

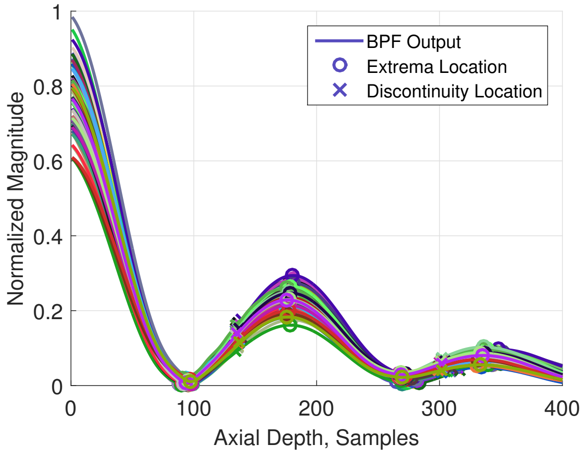

Figure 6-26: Amplitude mode characterization of acrylic reflecting layer. Each trace represents a single transducer element scan line.

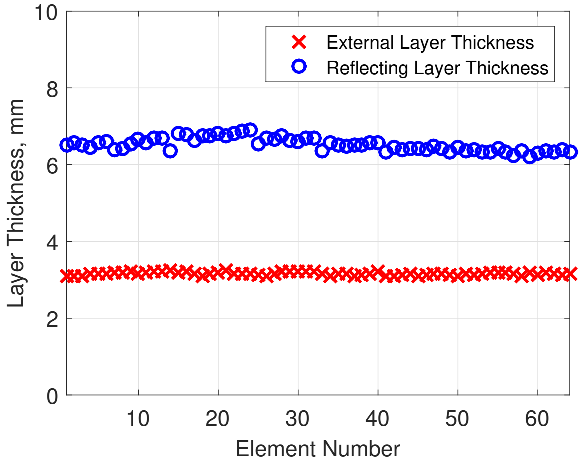

Figure 6-27: External and reflecting layer thickness at each transducer element.

From these discontinuity locations and presuming the propagation velocity within media boundaries, external layer – that is, media adjacent to the transducer array surface – and reflecting layer thickness are computed. As expected for the uniform thickness acrylic reflecting layer, Figure 6-27 reveals highly consistent thickness estimates at each transducer element location. After the geometry is known, propagation delay from the transducer element to the focal point is determined – as detailed in Section 4.4.

External layer and acrylic reflecting layer thickness are measured with calipers (01407A, Neiko Tools, Gardena, CA), yielding $Th_{\text{ext}} = 3.30\text{mm}$ and $Th_{\text{ref}} = 6.35\text{mm}$, respectively. Statistical characterization of estimated thickness values yields good agreement with conventional measurement techniques:

$$\mu_{Th_{\text{ext}}} = 3.27\text{mm} \quad \sigma_{Th_{\text{ext}}} = 0.04\text{mm}$$
$$\mu_{Th_{\text{ref}}} = 6.39\text{mm} \quad \sigma_{Th_{\text{ref}}} = 0.17\text{mm}$$

A series of fifteen data sets are measured on the flow phantom both with and without the use of focal correction methods. Focal correction gain is defined as the relative increase in Doppler power ratio P_{rel} between the focal corrected and uncorrected data segments. Positive focal correction gain directly results in increased measurement SNR, which is often a limiting factor in TCD sonography applications. Figure 6-28 demonstrates significant utility in employing focal correction – an average focal correction gain of 2.5dB is achieved over all trials. Similar focal correction gains are observed in human test subjects – although with less consistency between trials – and are presented in Section 7.5.

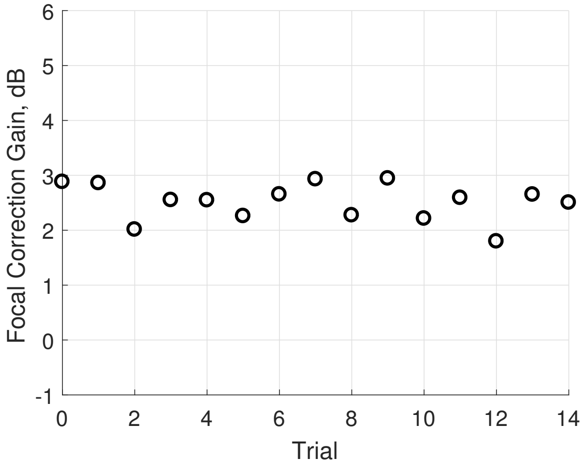

Figure 6-28: Focal correction gain over repeated flow phantom trials.

6.7 Summary

This chapter presents electrical validation of the discrete prototype TCD system. Transducer element impedance data is employed to extract an equivalent BVD element circuit model. Functionality of the analog receive path and digital signal processing blocks – including the RF bandpass filter, Hilbert transform, and beamformer delay – is demonstrated. Following electrical testing, a hydrophone is used to characterize acoustic pressures during transmit mode and ensure system operation within accepted safety limits.

Instrumentation hardware and signal processing methods are experimentally validated using a flow phantom. Doppler estimated flow velocity is shown to highly correlate with flow meter data over the range of expected *in vivo* flow velocities in the MCA. Doppler mapping is also realized and demonstrates the capability of prototype TCD instrumentation to localize regions of flow. Lastly, focal correction methods are verified using an acrylic reflecting layer; considerable increases in Doppler power ratio are achieved via focal correction techniques.

Chapter 7

Discrete Phased Array System Human Subject Validation

Human testing is performed to verify functionality of the discrete prototype system under *in vivo* conditions – notably, cranial attenuation, cerebrovascular anatomy, erythrocytic scattering, intracranial hemodynamics, and subject motion.

Testing is performed on healthy subjects with no known history of cerebrovascular pathology. Full ethical approval was granted from an affiliate ethics board (Massachusetts Institute of Technology Committee on the Use of Humans as Experimental Subjects) and informed consent obtained for all human subject volunteers.

Real-time operation of velocimetry and power mode Doppler methods is demonstrated. Velocimetric accuracy is evaluated with respect to a commercial single element TCD system.

7.1 TCD Examination Procedure

The examination procedure introduced by Aaslid has been adopted as the standard method for cerebral blood flow velocity (CBFV) evaluation using TCD sonography [12, 13]. The introduction of power motion mode (M-mode) Doppler – referred to as PMD – sonography has significantly altered the examination process due to the simultaneous display of flow intensity and direction over a wide range of insonation depths [17]. TCD examination techniques are presented in modified form to include PMD operation, thereby expediting cranial window and vessel localization via visualization rather than auditory Doppler cues [71, 95].

Clinical TCD evaluations are generally thorough and include flow velocity measurements for the entire cerebrovasculature over multiple acoustic windows. For our purposes, however, only insonation of the left and right middle cerebral artery (MCA) through the temporal acoustic window (TAW) is considered. Examination procedures are initially introduced for conventional manually steered TCD instrumentation – and later extended to incorporate distinct methods for electronic beamformation and algorithmic steering.

7.1.1 Conventional TCD Instrumentation

Conventional TCD evaluations are performed on stationary subjects in a supine or sitting position, with adequate time allowed for stabilization of the subject's heart rate and blood pressure. During prolonged TCD monitoring, a headframe can be employed to hold the transducer in position after an acceptable Doppler signal is obtained. For the limited measurement durations of this validation study ($\sim 1-5$ minutes), free-hand transducer manipulation is employed. A PMD insonation range of ≈ 20 to 70mm and moderate output power ($< 50\%$ maximum power) is selected.

To ensure sufficient acoustic coupling, the operator liberally applies ultrasound gel to the transducer surface. The transducer is then applied to the posterior TAW region, maintaining slightly upward and anterior probe angulation. Minimal force should be used to position and angle the transducer since substantial forces may cause subject discomfort and drive ultrasound gel away from the transducer surface. If no flow signals appear within the PMD display, the transducer is advanced in slow circular movements toward the anterior TAW region, changing probe angulation throughout the motion. All three common TAW regions (i.e., posterior, middle, and anterior) should be explored.

If no Doppler signal is attainable or if signals remain faint upon positioning optimization, acoustic output power can be incrementally increased until an adequate

Doppler signal is obtained or the maximum output power level is reached. In cases where Doppler signal remains absent at maximum output power following protracted investigation, the temporal window is considered nonpatent.

Once the optimal TAW region has been identified, the operator attempts to maximize signal intensity for the expected range of MCA depths through utilization of fine motor skills to incrementally adjust transducer position and angle. Transducer positioning must often be continually optimized throughout the measurement process due to slight misalignments caused by subject or operator movement. Doppler range gate depth is adjusted to the center of a contiguous, high flow intensity vessel segment within the MCA depth range [95].

Following TAW investigation and detection of flow velocity, emphasis of the TCD examination shifts toward identifying the Doppler signal source (i.e., the insonated vessel). A primary obstacle in accurate vessel identification is vast anatomical variance in cerebrovasculature structure, including variations in vessel caliber, course, and even origin. The reliability of vessel identification techniques varies among the intracranial vessels, with the highest accuracy of identification occurring for the ipsilateral MCA.

The MCA – along with its branches – is normally the only vessel perceptible from TAW insonation depths of 25 to 50mm [12]. Flow direction of the ipsiliateral MCA is generally toward the transducer, which is also observed for the posterior cerebral artery (PCA). To distinguish the MCA from the PCA, it is useful to trace the MCA extent with increasing depth to the terminal internal carotid artery (TICA) bifurcation, which is identified by bidriectional flow at an insonation depth of $55-65$mm [6]. MCA flow velocities are generally $> 25\%$ larger than PCA flow velocities. A detailed study of TCD vessel identification methods is given in [55].

7.1.2 Prototype TCD Instrumentation

Similar to conventional TCD methods, proper functionality of the prototype TCD system relies on placement of the transducer array at an appropriate acoustic window. Because the TAW region is generally associated with thinning of the cranial bone, potential locations can often be identified via palpation. The transducer array is applied to the tentative acoustic window location and Doppler power mapping – presented in Section 4.3.1 – is initialized.

After Doppler power mapping ($\approx$ 15 seconds), the maximum Doppler power ratio P_{rel} within the search volume is determined. In circumstances where adequate positive flow is not detected – resulting in $P_{rel} \lesssim 1.5$dB – the user interface indicates measurement invalidity. The transducer array is repositioned to another prospective TAW location and the Doppler mapping procedure is repeated.

The transducer array is placed flatly on the subject's temporal region and no attempt is made to manually angle the transducer surface. As discussed in Section 5.2, phased array operation of the current hardware implementation is restricted to modest steering angles ($|\phi_x|, |\phi_y| < 15°$). Operation of the prototype system therefore requires both an adequate acoustic window and favorable positioning of the underlying cerebrovasculature relative to the acoustic window. Correct functionality of the algorithmic vessel search procedure is not anticipated over the entirety of the population – and may be unattainable in certain subjects that exhibit TAW patency in evaluations employing conventional manually steered TCD instrumentation.

Following satisfactory realization of P_{rel} for Doppler power mapping at an appropriate TAW location, the coarse Doppler map and real-time Doppler spectrogram are displayed to the operator. Objective functions within the vessel search and subsequent vessel tracking processes preferentially yield ipsilateral MCA flow measurements – via maximization of P_{rel}, which favors positive (i.e., toward the transducer surface), unidirectional, high-volumetric flow within defined spatial bounds. Visual inspection of the Doppler power map and CBFV spectral envelope should be performed to ensure characteristics consistent with MCA flow.

7.2 Pulse-Echo Operation

Figure 7-1 presents the time-domain receive waveform of individual 12-bit analog-to-digital (ADC) channels (i.e., prior to receive beamformation) for transcranial pulse-echo operation. Separation of 3.2kSamples between successive transmit pulses indicates the decimation factor between ADC sampling and the pulse repetition frequency. The time-domain pulser mode waveform – with low indicating transmit mode and high indicating receive mode – emphasizes the considerable presence of receiver saturation after transmit pulsing – due to high-level reflections at the interface of soft tissue and cranial bone and finite amplifier recovery times. For maximum analog front-end (AFE) gain of 45dB, saturation is avoided for samples corresponding to depths $\gtrsim$ 20mm.

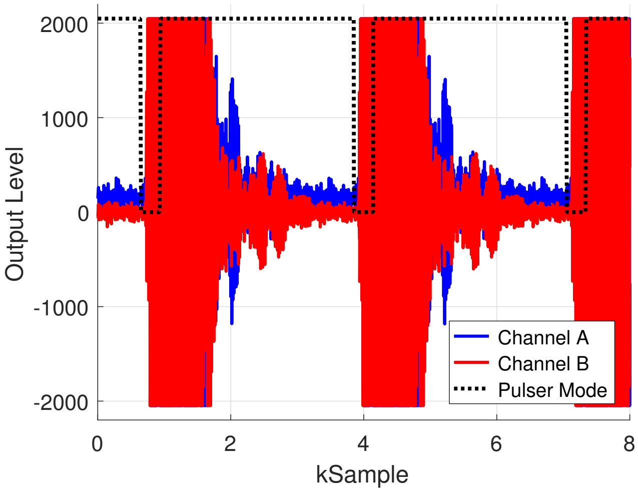

Figure 7-1: Individual ADC receive channel and pulser mode time-domain waveforms for pulse-echo operation during transcranial human testing.

Notably, signal levels for depths $\sim 40-65$mm are markedly below full-scale ($\lesssim$ 10%). Although gain control circuitry was implemented to optimize AFE signal levels, insufficient analog gain within the AFE significantly reduces available dynamic range and exacerbates ADC quantization effects.

Following receive beamformation, the combined radio frequency (RF) spectrum is presented in Figure 7-2(a) and demonstrates satisfactory bandpass filter (BPF) rejection of out-of-band spectral energy. In contrast to Figure 6-11, pulse-echo operation incorporates a highly periodic transmit excitation waveform $e_{Tn}(t)$ – as discussed in Section 2.1.3. High-level stationary tissue scattering therefore results in distinct spectral tones precisely separated by the pulse repetition frequency f_{PRF} – as shown in Figure 7-2(b). Similar to the ADC output data, receive beamformation signal levels are markedly below full-scale levels ($\lesssim -35$dBFS), despite maximum analog AFE gain.

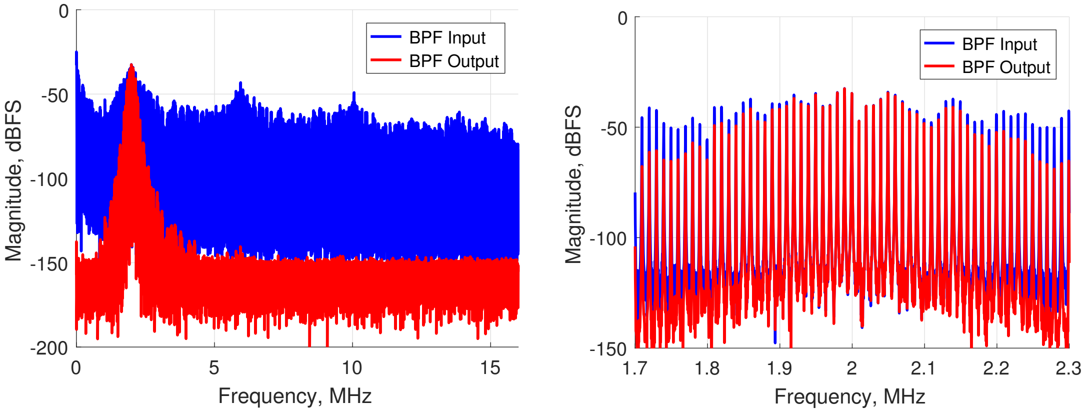

(a) Nyquist frequency spectrum. (b) RF filter bandwidth spectrum.

Figure 7-2: RF receive beamformation frequency spectra for pulse-echo operation during transcranial human testing.

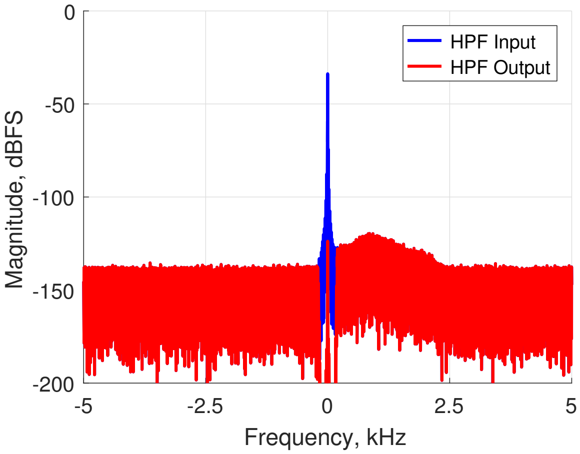

Figure 7-3: Baseband pulse-echo frequency spectra and clutter reject filtering during transcranial human testing.

Figure 7-3 presents the baseband echo signal and resulting clutter reject high-pass filter (HPF) output. Marked attenuation ($>$ 90dB) of the stationary echo data is achieved via clutter reject filtering. Doppler power is discernible for positive baseband velocities – resulting from positive blood flow velocities. Integration of the baseband spectrum yields Doppler power ratio $P_{rel} = 10.3$dB and signal-to-noise ratio SNR =

6.8dB for *in vivo* human testing. Although moderate, achieved transcranial SNR values are promising and provide some margin for variation across test subjects.

Figure 7-4 displays the Doppler spectrogram and overlaid spectral envelope for MCA flow in human subject test data, emphasizing CBFV dynamics over several cardiac cycles and over longer time-course (∼ 60 seconds). Figure 7-4(a) demonstrates the high pulsatility expected from MCA flow – due to its significant diameter and origin as a continuation of the TICA – and exhibits consistent waveform morphology between cardiac cycles. Figure 7-4(b) displays peak systolic and end diastolic values of the CBFV envelope. Considerable deviations in peak systolic and end diastolic values are observed over time, corresponding to changes in downstream metabolic demand and arterial blood pressure variation.

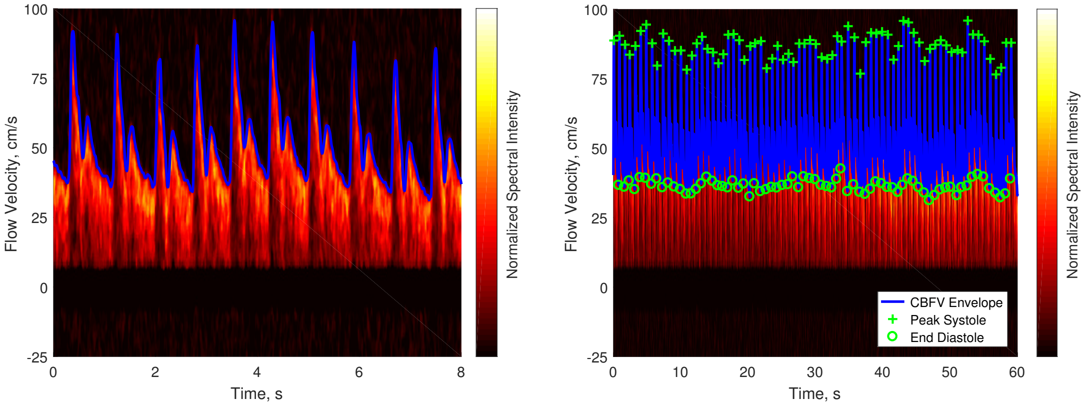

(a) Spectrogram over several cardiac cycles.

(b) Spectrogram over 60 seconds.

Figure 7-4: Doppler spectrogram and spectral envelope during transcranial human testing.

7.2.1 Graphical User Interface

A graphical user interface (GUI) is necessary to display measurement information on a remote host. The GUI is also needed to adjust instrumentation parameters, change operating modes, and control data capture. Real-time Doppler power mapping and spectrogram information are displayed to the operator, as shown in Figure 7-5.

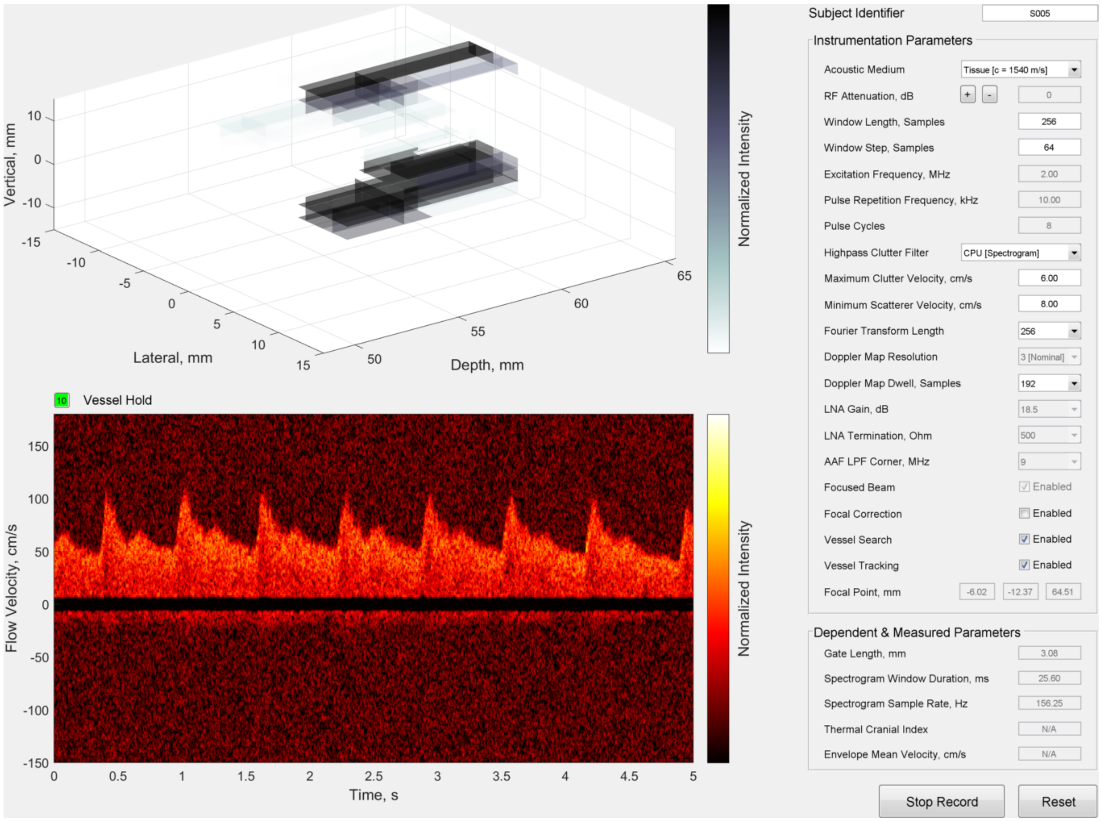

Subject Identifier	S005

Instrumentation Parameters

Acoustic Medium	Tissue [c = 1540 m/s]
RF Attenuation, dB	0
Window Length, Samples	256
Window Step, Samples	64
Excitation Frequency, MHz	2.00
Pulse Repetition Frequency, kHz	10.00
Pulse Cycles	8
Highpass Clutter Filter	CPU [Spectrogram]
Maximum Clutter Velocity, cm/s	6.00
Minimum Scatterer Velocity, cm/s	8.00
Fourier Transform Length	256
Doppler Map Resolution	3 [Nominal]
Doppler Map Dwell, Samples	192
LNA Gain, dB	18.5
LNA Termination, Ohm	500
AAF LPF Corner, MHz	9
Focused Beam	☑ Enabled
Focal Correction	☐ Enabled
Vessel Search	☑ Enabled
Vessel Tracking	☑ Enabled
Focal Point, mm	-6.02 -12.37 64.51

Dependent & Measured Parameters

Gate Length, mm	3.08
Spectrogram Window Duration, ms	25.60
Spectrogram Sample Rate, Hz	156.25
Thermal Cranial Index	N/A
Envelope Mean Velocity, cm/s	N/A

Figure 7-5: Remote host graphical interface.

7.3 Flow Velocimetry

Accuracy of velocimetry methods was validated with respect to a commercial single element TCD system (DWL Doppler-Box X, Compumedics, Singen, Germany). The single element TCD system is manually steered using the methods described in Section 7.1.1. The prototype phased array TCD system requires operator localization of an adequate TAW region and employs algorithmic vessel search and tracking to obtain velocimetry data, as described in Section 7.1.2.

The test protocol consists of three moderate length ($30 - 90$ second) CBFV envelope measurement segments on each system. The initial measurement system is randomly determined and subsequent measurements are alternated between the two TCD systems. Peak systolic CBFV envelope is computed at each cardiac cycle throughout the measurement duration. The CBFV envelope is averaged over successive periods of five adjacent cardiac cycles. Ten human subjects were recruited for the study. Sufficient measurement SNR was achieved for all ten subjects using the single element TCD system. For the prototype system, all ten subjects yielded discernible flow characteristics on the Doppler spectrogram. Measurement SNR was, however, inadequate to yield a reliable CBFV envelope for one of the test subjects using the prototype system.

Figure 7-6 presents the peak systolic CBFV envelope averaged over all data sets for the nine test subjects with adequate CBFV envelope data. Error bars are used to indicate the standard deviation of peak systolic CBFV over each subject data set.

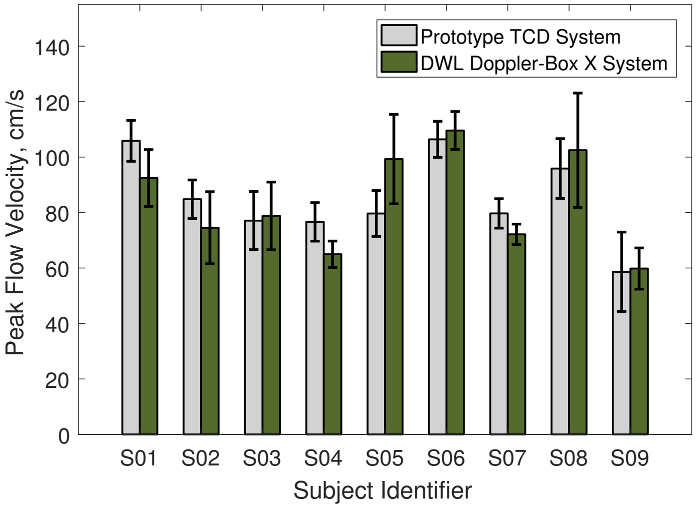

Figure 7-6: Comparison of peak systolic CBFV envelope across test subjects.

Comparison of the DWL single element and prototype TCD systems yields a peak systolic CBFV envelope difference mean of 1.2cm/s and difference standard deviation of 10.6cm/s.

Figure 7-7 presents the five cardiac cycle mean CBFV envelope averaged over all subject data sets for the nine subjects with adequate CBFV envelope data. Error bars are used to indicate the standard deviation of cycle-averaged CFBV envelope samples over each subject data set.

Comparison of the DWL single element and prototype TCD systems yields a cycle-averaged CBFV envelope difference mean of -0.66cm/s and difference standard deviation of 6.3cm/s. Peak systolic and cycle-averaged CBFV envelope difference mean values are minimal, the prototype TCD system is therefore considered a relatively unbiased measure of CBFV envelope.

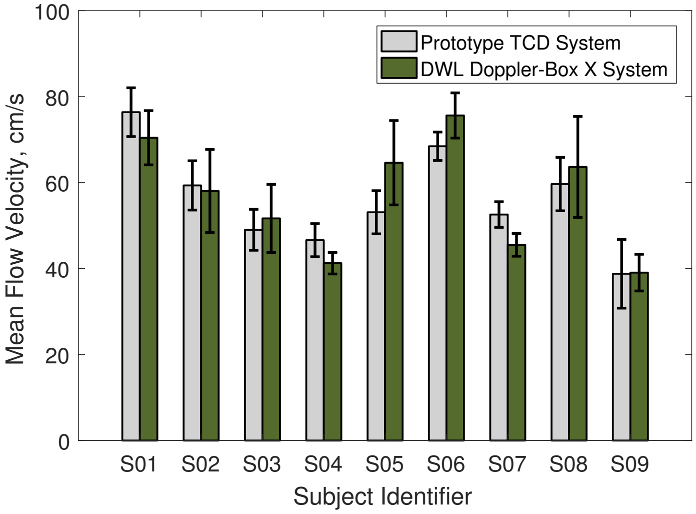

Figure 7-7: Comparison of cycle-averaged mean CBFV envelope across test subjects.

7.4 Power Mode Doppler Signal Processing

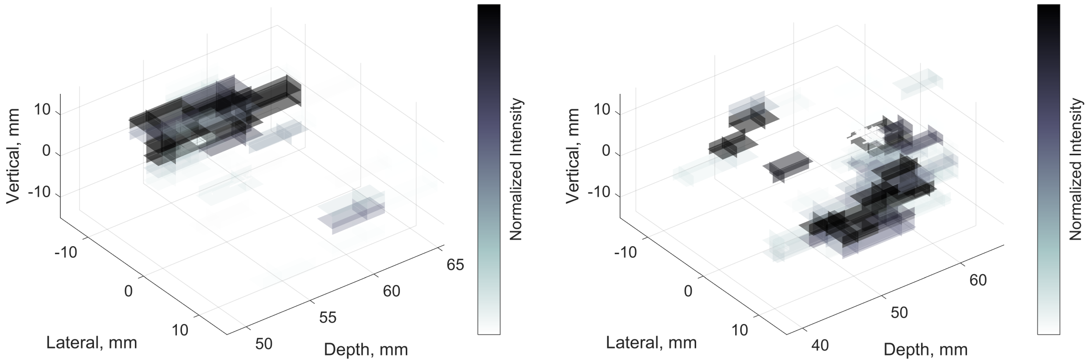

(a) Straight vessel segment.

(b) Curved vessel segment.

Figure 7-8: Human validation coarse Doppler power map.

The Doppler power mapping technique is employed by the vessel search algorithm to localize regions of maximal flow. The coarse Doppler map is also presented to the operator as a visual representation of the underlying vessel structure. Figure 7-8 displays the Doppler power map for two different test subjects. Conclusion of the mapping procedure results in sufficient P_{rel} at the focal region for spectrogram generation and also yields contiguous regions of elevated P_{rel} – corresponding to an intracranial vessel segment. Figure 7-8(a) presents a straight, but offset segment $\approx$ 12mm in length. Figure 7-8(b) presents a relatively curved vessel segment. As done in TCD color flow imaging instrumentation, relation of the focal region within the vessel segment can be used to estimate and correct for Doppler angle. As observed in Section 6.5, grating lobe generation yields spatial aliasing of the flow region at the negative steering angle, although at reduced intensity.

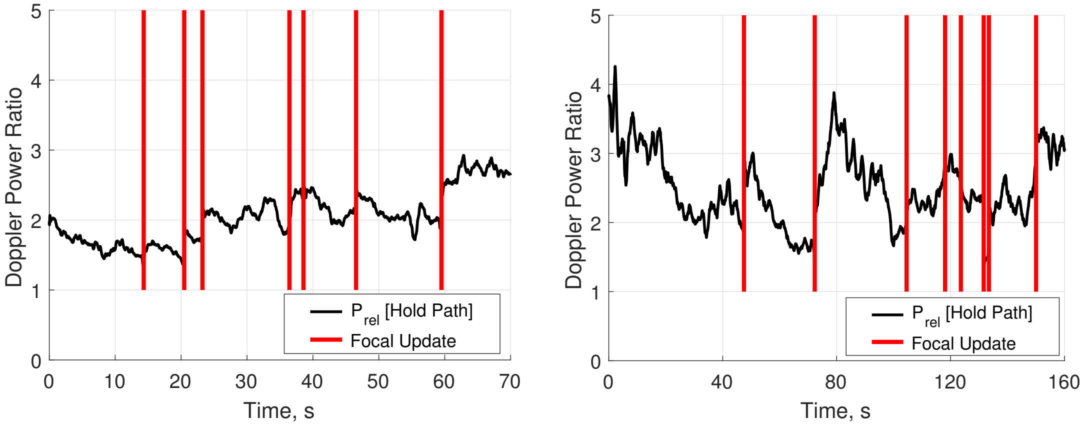

Figure 7-9: Temporal demonstration of transcranial vessel tracking functionality in two distinct human test subjects.

Doppler tracking is a background process that facilitates real-time adjustment of focusing to account for relative motion between the transducer array and intracranial vessel segment. For free-hand measurements, tracking operation proved extremely beneficial in ensuring sufficient SNR throughout the measurement duration. No attempts were made by the operator to intentionally correct for degradation in signal quality. As observed in Figure 7-9, the tracking procedure was able to maintain sufficient P_{rel} and mitigate motion induced focal offsets – where focal updates indicate adjustment to the transmit and receive hold path focal points. Although measurements employing a headframe are likely more stable than free-hand measurements, degradation of signal quality and the need for continual operator adjustment are common in a majority of TCD evaluations. Although tracking offsets are limited by beamwidth of the transmit beam pattern (∼ 4mm), tracking functionality was able to maintain adequate measurement SNR in the vast majority of free-hand human testing.

Figure 7-10 presents the spatial influence of tracking on the receive hold path focal point, where arrows indicate the progression of focal point over time.

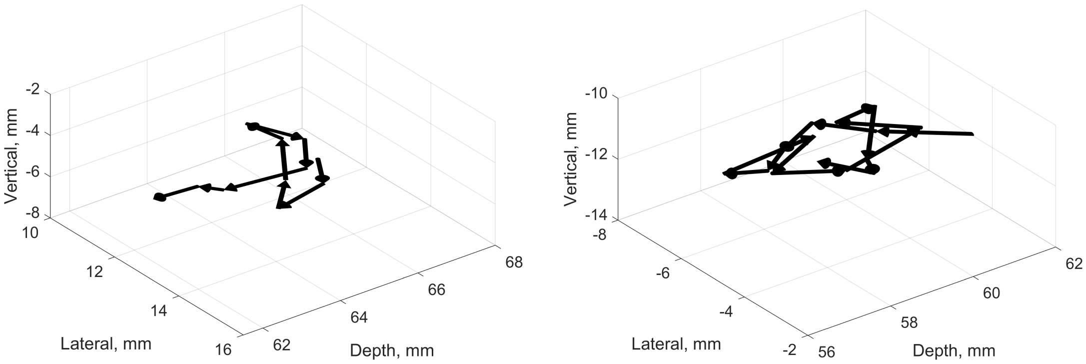

Figure 7-10: Spatial demonstration of transcranial vessel tracking functionality in two distinct human test subjects.

7.5 Focal Correction

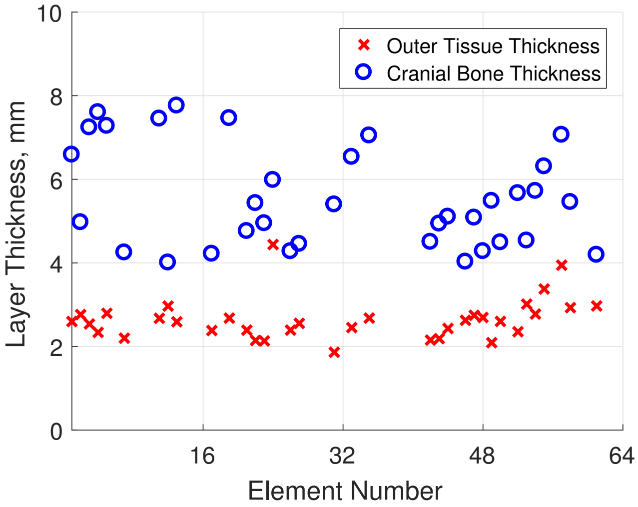

Figure 7-11: Outer tissue and cranial bone thickness at each transducer element.

As detailed in Section 6.6, each transducer element is sequentially excited and a corresponding amplitude mode scan line is generated. External layer and reflecting layer (i.e., cranial bone) thickness are computed from the resulting amplitude mode data, as presented in Figure 7-11.

Statistical characterization of estimated thickness values yields considerable variation:

$$\mu_{Th_{\text{ext}}} = 2.61\text{mm} \quad \sigma_{Th_{\text{ext}}} = 0.53\text{mm}$$
$$\mu_{Th_{\text{ref}}} = 5.48\text{mm} \quad \sigma_{Th_{\text{ref}}} = 1.30\text{mm}$$

Causes of variation may be partially physical – that is, non-uniform tissue and cranial bone thickness. Practical human data, however, is often complicated by degraded acoustic coupling – including insufficient ultrasound gel and the presence of air bubbles and hair. For certain elements, adequate extrema locations are not present and therefore thickness estimates cannot be computed. Due to this high degree of variability, mean thickness values are used for human focal correction methods – rather than local thickness values at each transducer element.

A series of fifteen data sets are measured on a single human test subject both with and without the use of focal correction. As observed in Figure 7-9, Doppler power ratio can varying significantly during human testing. Variability of focal correction gain is therefore significant between trials. Mean focal correction gain of 2.7dB was, however, achieved over all trials.

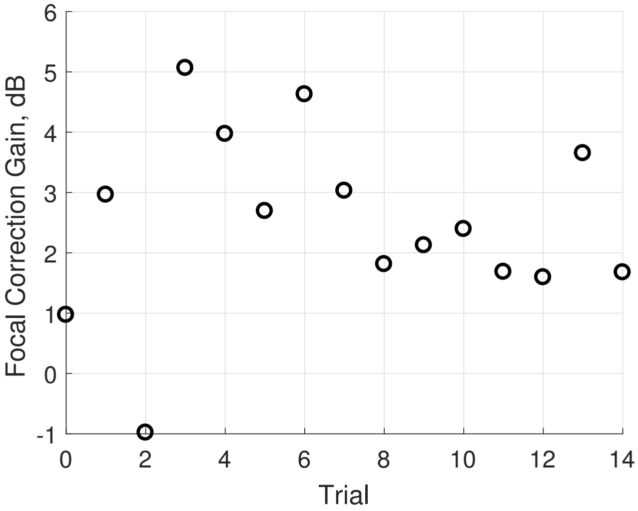

Figure 7-12: Focal correction gain over repeated trials on a single human subject.

7.6 Summary

This chapter introduces standard TCD examination techniques and describes necessary modifications to these techniques for the prototype TCD instrumentation of this work. A GUI is presented, which aids the operator in adjusting instrumentation parameters, operating modes, and data capture. CBFV envelope data from the prototype TCD system is compared to a commercial TCD system over nine human test subjects and minimal bias is achieved. Functionality of Doppler mapping and vessel tracking algorithms is demonstrated on human test subjects in the presence of subject motion. Lastly, focal correction methods are validated under human testing and considerable improvement to the Doppler power ratio – and therefore measurement SNR – is observed.

Chapter 8

Integrated Phased Array System Design

Application specific integrated circuit (ASIC) design is explored to moderate exceedingly complex and power inefficient discrete electrical hardware implementations, thereby considerably decreasing system dimensions and improving device wearability for continuous monitoring applications. Review of Figure 6-7 reveals a significant portion of system power ($> 80\%$) is dissipated solely in the transceiver analog front-end (AFE) and analog-to-digital converter (ADC) circuitry.

Commercially available discrete transceivers must provide sufficient performance for a variety of operating modalities – including brightness mode (B-mode) imaging. Mixed modality transceiver specifications are markedly distinct from transcranial Doppler (TCD) sonography specifications – particularly regarding linearity, high-voltage (HV) supply levels, transmit recovery, and gain control.

Disparate requirements greatly constrain general purpose transceiver design and result in added hardware complexity and power consumption. ASIC design specific to the demands of TCD sonography facilitates the introduction of novel circuit topologies and consolidates functionality objectives to a highly definable framework. Integrated transceiver design and relevant extensions to phased array system implementation are examined in this chapter.

8.1 System Architecture

Leveraging efforts from discrete hardware development, an ASIC-based Doppler velocimetry architecture – referred to as the integrated phased array system – is presented in Figure 8-1.

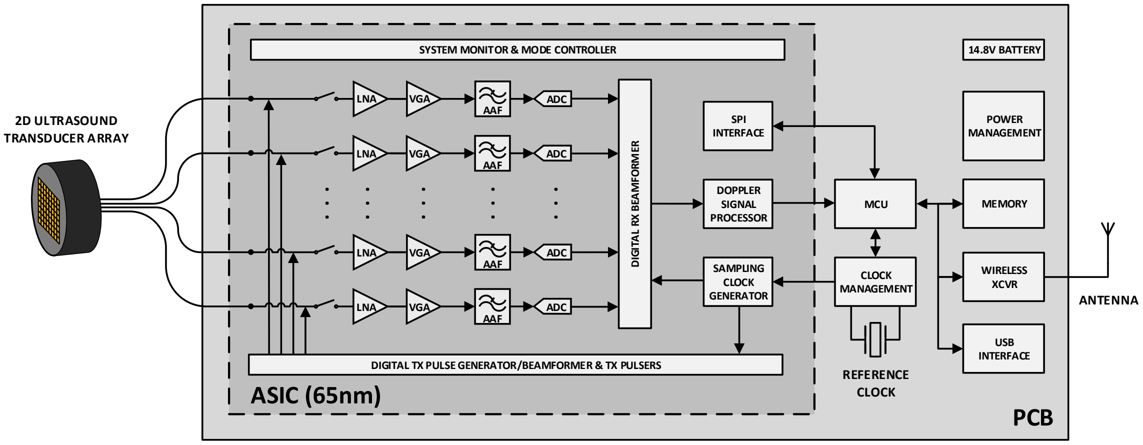

Figure 8-1: Integrated phased array system hardware block diagram.

Analog, mixed-signal, and low-level digital signal processing are achieved within the ASIC – replacing the transceiver, field programmable gate array (FPGA), gain control, and digital interfacing hardware. Microcontroller (MCU), memory, and external communication interfaces (i.e., USB and Bluetooth low energy) are retained from the existing discrete system implementation described in Chapter 5. Power management circuitry is greatly simplified for the integrated architecture since polarity inversion and boost conversion of power supplies are not required.

8.2 Integrated Circuit Design

ASIC implementation is designed in a standard 65nm complementary metal oxide semiconductor (CMOS) process. For single die ASIC operation, per-channel transceiver area is highly constrained and flip-chip bonding is necessary to achieve adequate input/output (I/O) interfacing. Per-channel transceiver dimensions $< 350\mu$m x $< 350\mu$m and flip-chip ball pitch $\approx 275\mu$m facilitates 144 I/O signal, 64 channel operation occupying less than 4mm x 4mm die area – including biasing and digital processing circuitry.

The proposed ASIC design incorporates the transmit pulser, transmit/receive (T/R) switch, low-noise amplifier (LNA), variable gain amplifier (VGA), anti-aliasing filter (AAF), and analog-to-digital converter (ADC). Figure 8-2 presents a block diagram of the ASIC architecture.

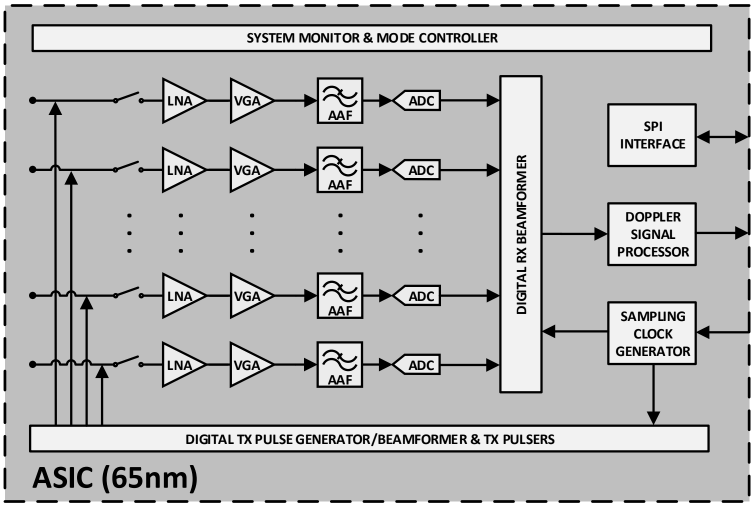

Figure 8-2: Integrated circuit block diagram.

Digital logic for beamformation, system control, Doppler signal processing, and data communication is included in assessment of ASIC functionality, but is not directly implemented. Register-transfer level (RTL) synthesis from FPGA-based designs are utilized for gross estimation of ASIC area and power consumption. Optimization of digital circuitry can further reduce hardware resources and power requirements, but is not considered in this work.

8.2.1 Transmit Pulser and Impedance Matching Network

Transceiver integration is often complicated by the need for HV components – particularly, transmit pulser, T/R switch, and protection circuitry. Because imaging modes employ short pulse duration and limited focal dwelling, acoustic safety indices – especially spatial-peak-temporal-average intensity (I_{SPTA}) – permit increased

HV supply levels. Discrete ultrasound transceivers therefore generally accommodate HV supply levels up to ±100V, placing considerable limitations on analog front-end circuitry. Non-standard process technologies with high breakdown voltage devices – such as laterally diffused metal oxide semiconductor (LDMOS) devices – are therefore required and often result in multi-chip transceiver implementations.

In Doppler sonography, a standard CMOS process can be employed to achieve sufficient acoustic output power via 3.3V I/O devices and transducer element impedance matching techniques. Figure 8-3(a) presents the transmit pulser and T/R switch schematic, where switches S_0 through S_3 are implemented with 3.3V I/O transistors, V_{IO} is the ASIC output node, and V_{RX} is the LNA input node. Sizable transistors – with lengths of $\sim$ 500nm and widths of several 100μm – are utilized to achieve switch impedances of $\sim 10 - 50\Omega$. Bipolar pulsing is achieved through pull-up (to $TV_{DD} = 3.3$V) and pull-down (to ground) switching about the steady-state common mode ($TV_{CM} = 1.65$V). Transmission gate structures are employed to implement intermediate voltage switching (i.e., S_0 and S_3), such that switch impedance variation is minimized.

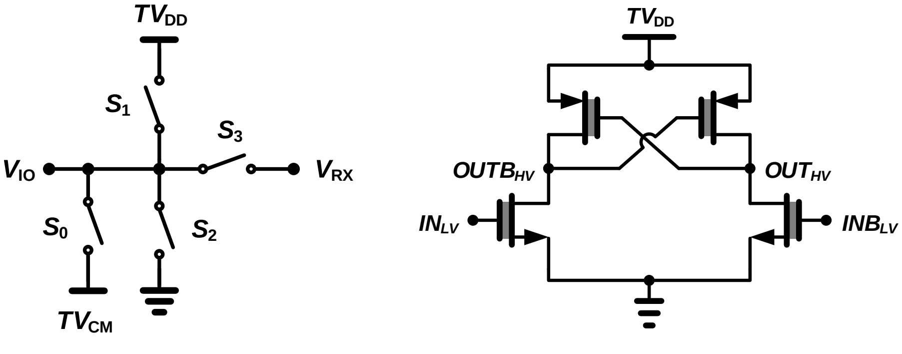

(a) Pulser and T/R switch schematic.

(b) Level translation schematic.

Figure 8-3: Transmit pulser and T/R switch schematics, including level translation.

CMOS logic signals ($V_{DD} = 1.2$V) from the transmit beamformer are translated to the I/O domain ($TV_{DD} = 3.3$V) to control transmit pulser switch state. A standard cross-coupled topology is employed for level translation, as shown in Figure 8-3(b) –

where shaded gate dielectric emphasizes I/O domain devices [96]. Level translation devices are properly sized to achieve comparable rise and fall times, thereby reducing second-order harmonic generation.

Discrete (i.e., off-chip) series (L_S) and parallel (L_P) inductors form the transducer element matching network, as displayed in Figure 8-4(a). Impedance matching yields a significant increase in transducer element driving voltage (V_{EL}) – and thereby increased acoustic output power – for fixed 0 to 3.3V transmit supply levels, as shown in the time-domain waveform in Figure 8-4(b). Using extracted Butterworth VanDyke (BVD) model parameters from Section 6.1, transducer element driving voltage $V_{EL} > \pm 10V$ and time-average radiated power $P_{OUT,TA} > 30\text{mW}$ are realized.

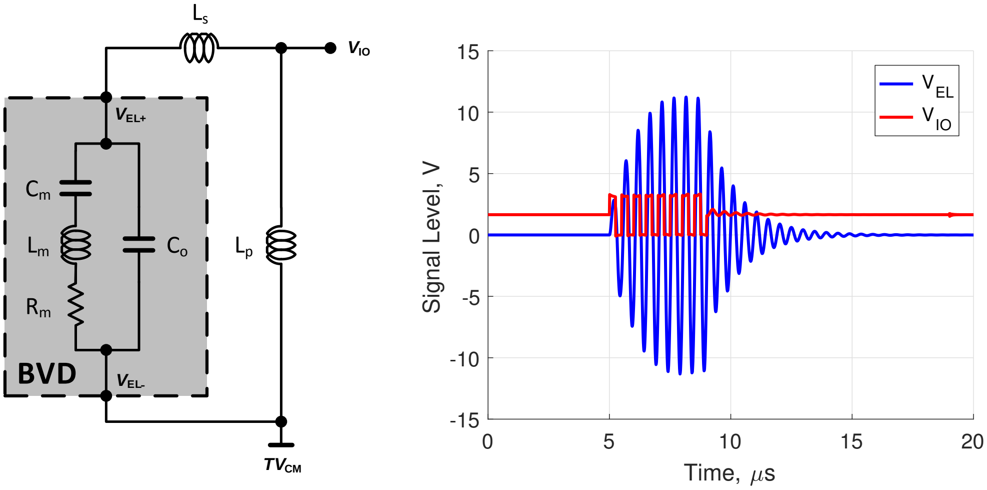

(a) Matching network schematic. (b) Time-domain transmit waveform.

Figure 8-4: Effect of transducer element matching network on transmit waveform.

Parallel inductance L_P is employed to absorb charge injection from the common-mode clamp (i.e., S_0) and T/R switch (i.e., S_3) prior to signal reception. Matching network component selection markedly influences transmit and receive transfer function magnitude – $|H_{TX}|$ and $|H_{RX}|$, respectively. Inductor values are chosen to maximize pulse-echo transfer function magnitude $|H_{PE}| = |H_{TX} \cdot H_{RX}|$ over the relevant frequency band (i.e., $\approx 1.8 - 2.2\text{MHz}$), yielding $L_S = 33\mu\text{H}$ and $L_P = 15\mu\text{H}$ – as shown in Figure 8-5(a).

Figure 8-5(b) illustrates the significance of impedance matching on $|H_{RX}|$, yielding a 12dB improvement relative to the unmatched case. Impedance matching, however, results in increased sensitivity to component and transducer element tolerances. Monte-Carlo analysis yields ≈ 1.2dB standard deviation of $|H_{PE}|$ within the band of interest under expected parameter variation. To achieve inter-channel gain matching of < 0.25dB, per-channel gain calibration via low-precision ($\leq$ 8-bit) multiplication is therefore likely desirable prior to receive beamformation. Additionally, transducer impedance matching yields considerable out-of-band interferer rejection, minimizing saturation and linearity concerns for spurious tones.

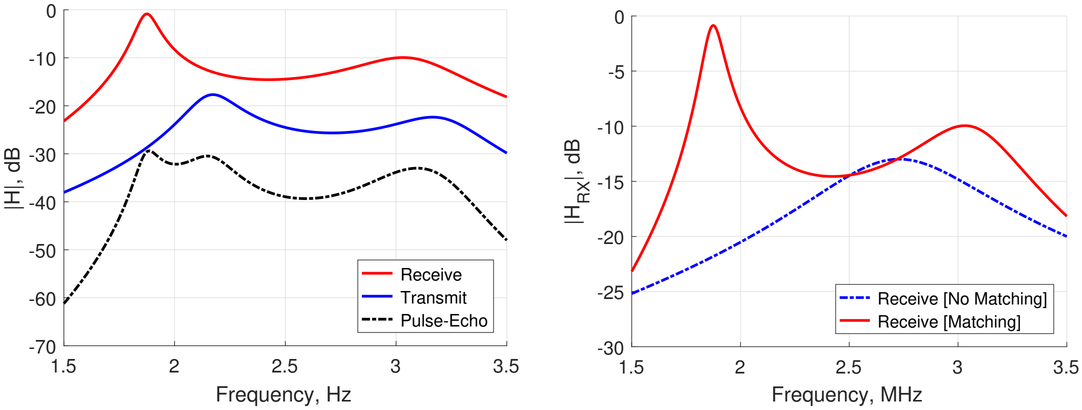

(a) Transfer function magnitude.

(b) Receive gain enhancement.

Figure 8-5: Effect of matching network on pulse-echo operation.

Compact layout of the transmit pulser, T/R switch, level translation, and switch control logic is given for a single channel in Figure 8-6. Active power dissipation in the transmit pulser is highly dependent on transducer loading and pulse duration characteristics; static power dissipation is negligible.

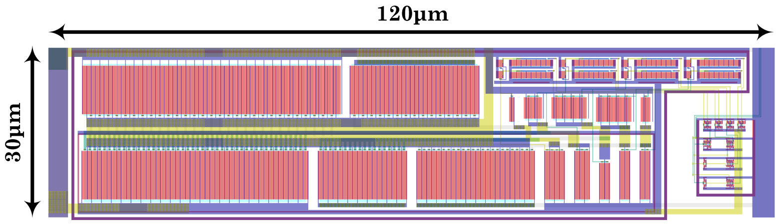

Figure 8-6: Layout of transmit pulser, T/R switch, and associated circuitry.

8.2.2 Low-Noise Amplifier

The primary objective of LNA design is to provide moderate gain with minimal noise contribution, power dissipation, gain variation, and die area. Fixed gain is realized by means of a transconductance amplifier G_m and capacitive feedback, as shown in Figure 8-7(a). C_S and C_F are implemented as metal-oxide-metal (MOM) capacitors and are ratioed as an array of equal dimension unit capacitors – thereby minimizing fabrication tolerance effects on gain.

The transconductance amplifier G_m is realized as a common-source amplifier with cascoded active load, as shown in Figure 8-7(b). Biasing of the G_m stage is achieved during transmit operation using a reset device (i.e., M_4), which – unlike resistive biasing – has minimal effect on noise and amplifier area. Over pulse repetition periods generally employed in TCD sonography ($\sim 50 - 100\mu$s), bias drift of $\approx$ 20mV is observed at the LNA output node. Low frequency ($\lesssim$ 100kHz) attenuation is therefore needed in subsequent amplifier stages.

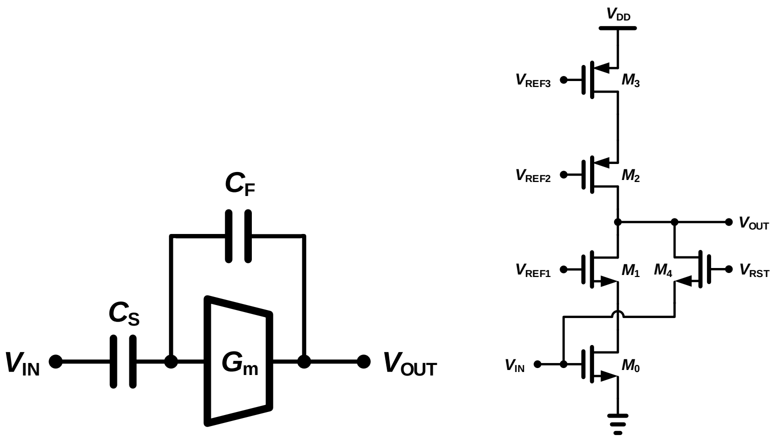

(a) LNA schematic.

(b) Transcondutance amplifier schematic.

Figure 8-7: LNA schematic with transconductance amplifier and capacitive feedback.

Small-signal gain and noise circuit models for the proposed LNA implementation are given in Figure 8-8, where C_P is parasitic input capacitance, transconductance $G_m = g_{M0}$, r_0 is cascoded output impedance, C_L is load capacitance, and i_n is a current noise source.

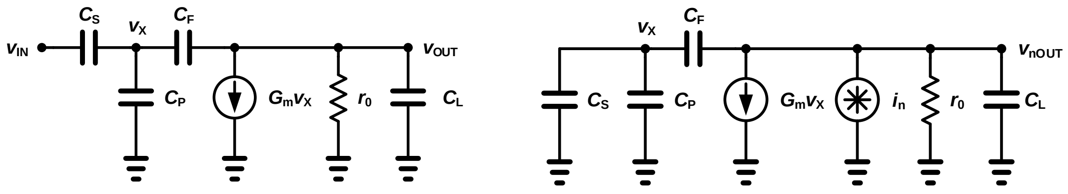

(a) Gain model.

(b) Noise model.

Figure 8-8: LNA small-signal equivalent gain and noise schematics.

At frequencies considerably below the 3dB frequency ($f_{\text{LNA,3dB}} \gtrsim 100\text{MHz}$), gain of the LNA is expressed as:

$$A_{\text{LNA}} \approx \frac{-G_m C_S r_0}{G_m C_F r_0 + C_F + C_P + C_S} \approx -\frac{C_S}{C_F} \tag{8.1}$$

Assuming sufficient device dimensions to limit flicker noise at MHz frequencies, noise analysis yields input-referred noise voltage per unit bandwidth $\overline{v_{n,\text{IN}}^2}$.

$$\overline{v_{n,\text{IN}}^2} \approx \frac{4kT(C_F + C_S + C_P)^2}{C_S^2} \left(\frac{\gamma_N}{g_{m0}} + \frac{\gamma_P g_{m3}}{g_{m0}^2} \right) \tag{8.2}$$

In Equation 8.2, k is the Boltzmann constant, T is absolute temperature, γ_N and γ_P are technology dependent noise coefficients ($\gamma_N, \gamma_P \sim 1 - 3$), and g_{m0}, g_{m3} are the transconductance of devices M_0 and M_3, respectively.

Device parameter characterization and basic relational models facilitate constrained optimization (MATLAB, Mathworks, Natick, MA) of design values under a variety of specifications. Effects of feedback capacitance and input device (i.e., M_0) width on input-referred voltage noise are shown in Figure 8-9.

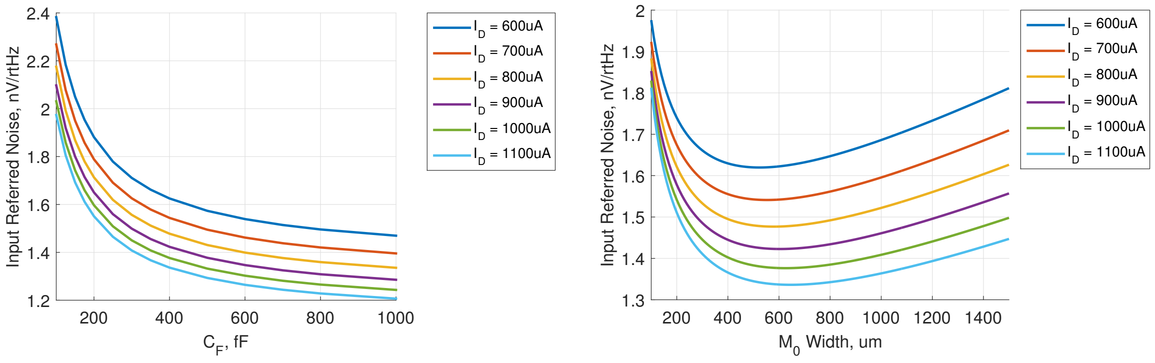

(a) Influence of C_f.

(b) Influence of M_0 width.

Figure 8-9: Effect of selected design parameters on input-referred voltage noise.

Post-extraction simulation (i.e., accounting for layout parasitics) results for LNA gain and input-referred voltage noise are given in Figure 8-10 with $C_S = 5.5$pF and $C_F = 390$fF. For the frequencies of interest (i.e., $\approx 1.8 - 2.2$MHz), gain of ≈ 21.5dB, input-referred voltage noise $< 1.1\text{nV}/\sqrt{\text{Hz}}$, and input impedance $> 15\text{k}\Omega$ are achieved with power dissipation of 1.1mW. Gain matching between channels cannot be assessed directly, but is expected to be < 0.25dB due moderate sized unit capacitance ($\approx$ 400fF) and layout symmetry.

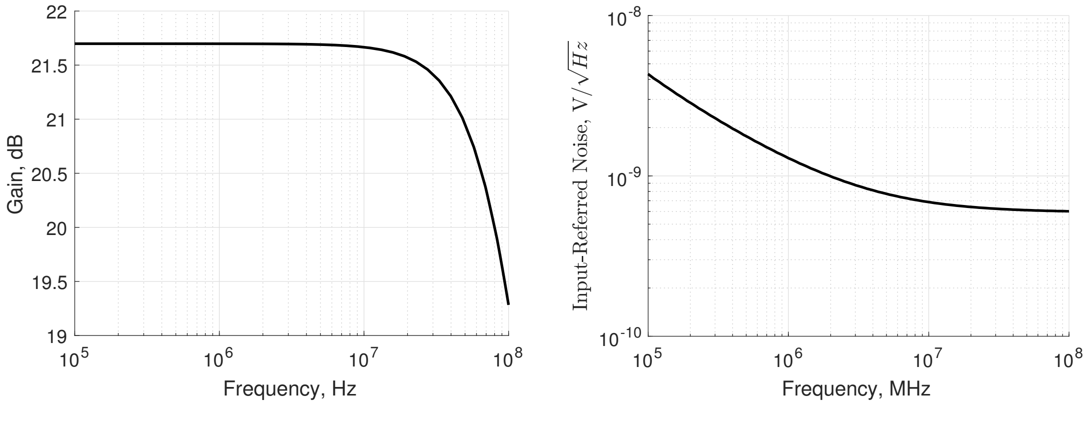

(a) LNA gain.

(b) LNA input-referred noise voltage.

Figure 8-10: Post-extraction LNA gain and noise simulation.

A compact, single channel layout of the integrated LNA is shown in Figure 8-11. Single-ended topologies are desirable for power and area efficient design, but result in increased sensitivity to power supply noise and substrate-coupling. Power supplies and bias references – particularly, V_{REF1}, V_{REF2}, and V_{REF3} – are common for all LNA channels and therefore realistic assessment of power supply filtering and interferer coupling is problematic. Deep N-well isolation is employed to diminish substrate-coupling, but substrate effects cannot generally be evaluated without physical testing.

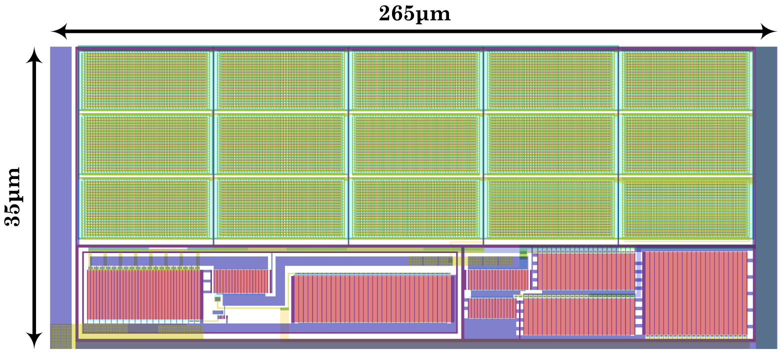

Figure 8-11: LNA layout.

8.2.3 Variable Gain Amplifier

VGA design is less constrained by transceiver noise requirements due to significant preceding LNA gain. However, noise generation within the VGA must be appropriately considered to ensure minimal impact on cascaded input-referred noise. For TCD sonography applications, considerable digital gain control must be provided with moderate gain resolution. Single-ended to differential conversion is realized to improve power supply and interferer rejection within the VGA and the subsequent differential signal path. A cascaded operational-amplifier (op-amp) network with configurable feedback factor is employed to achieve variable gain – as presented in Figure 8-12.

Resistors within the feedback path – $\mathrm{R_{F1}}$ and $\mathrm{R_{F2}}$ – yield increased feedback factor for low frequency signals. The resulting high-pass VGA gain characteristic thereby reduces the effects of LNA bias drift and physical device mismatch – notably, input offset voltage.

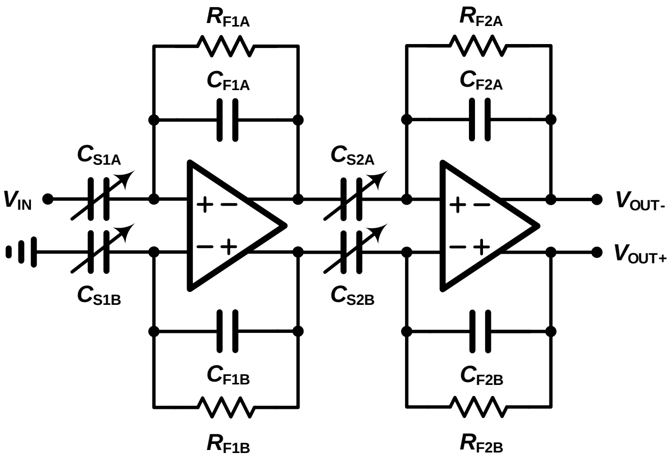

Figure 8-12: VGA schematic utilizing cascaded closed-loop op-amp networks.

For $C_F = 50\text{fF}$, significant resistance ($\sim 4\text{M}\Omega$) is required to achieve the desired high-pass corner frequency of $\sim$ 1MHz. By utilizing non-silicide polysilicon resistors, total resistor area is manageable, but strongly influences VGA dimensions. Active techniques may be employed to reduce feedback resistor area; such techniques, however, are not considered in this work.

Capacitors C_{S1} and C_{S2} are realized as binary weighted capacitor arrays. Each variable capacitor is digitally configurable from 100fF to 1.6pF, resulting in total VGA gain of 10dB to 58dB with 6dB steps.

A fully-differential two-stage op-amp with Miller compensation is employed to provide high open-loop gain and near rail-to-rail swing, as shown in Figure 8-13(a). Appropriate cancellation of the right half-plane zero is achieved using a digitally configurable nulling resistor R_0 [97].

An auxiliary amplifier is utilized to establish output node (i.e., V_{OUT+} and V_{OUT-}) biasing using common-mode feedback (CMFB), as detailed in Figure 8-13(b). Compensation of the CMFB loop is required for stable operation and is largely achieved through proper sizing of C_1. V_{CM} is an external reference generally set to $V_{DD}/2$ to maximize output swing.

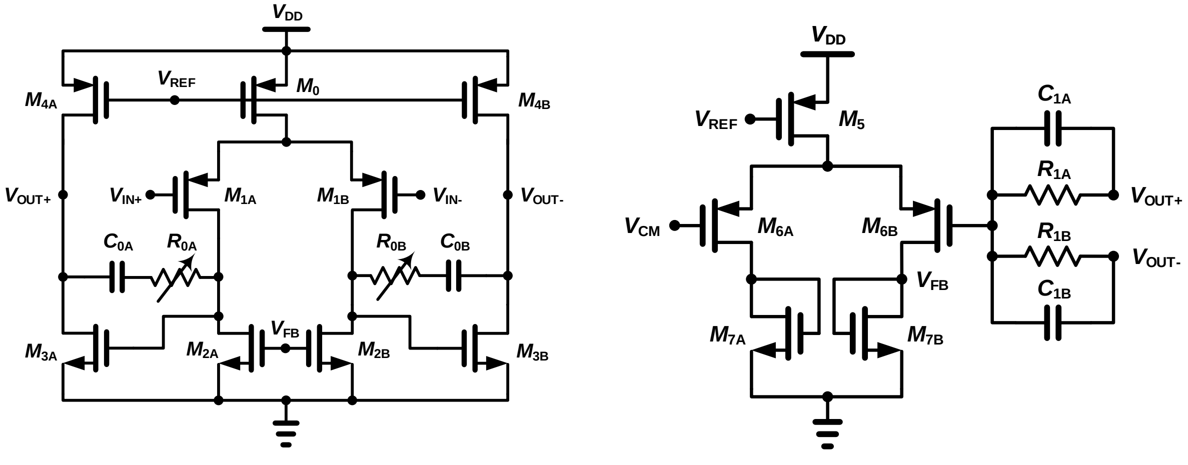

(a) Two-stage op-amp schematic. (b) CMFB auxiliary amplifier schematic.

Figure 8-13: Op-amp schematic with CMFB biasing network.

Post-extraction simulation of VGA gain is presented in Figure 8-14 for all gain settings. Within the frequency band of interest, gain variation is < 0.5dB at each gain setting. Analogous to the LNA design, inter-channel mid-band gain variation is expected to be < 0.25dB due to relatively process independent MOM capacitor matching for moderately sized capacitors ($\gtrsim$ 100fF). VGA power dissipation of 1mW and output swing amplitude > 1.0V is achieved.

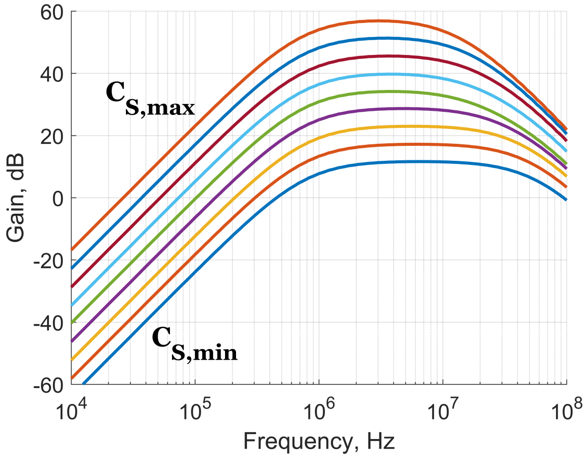

Figure 8-14: VGA gain for various gain settings.

At 2MHz, post-extraction gain and input-referred noise are presented in Figure 8-15 for all gain settings. Linear-in-dB gain control with 6dB step size is attained. For

VGA gains > 25dB, noise generation within the VGA circuitry has negligible influence on input-referred transceiver noise. At low gain settings, however, VGA generated noise increases markedly and strongly influences cascaded noise levels. Operation in low gain settings is appropriate only for elevated input signal levels, thereby yielding adequate measurement signal-to-noise ratio (SNR) despite augmented noise power. VGA gain control settings are typically common to all channels and provide gross adjustment of receive gain. As discussed in Section 8.2.1, modest gain adjustment to correct for inter-channel and inter-transducer mismatch is realized after signal digitization.

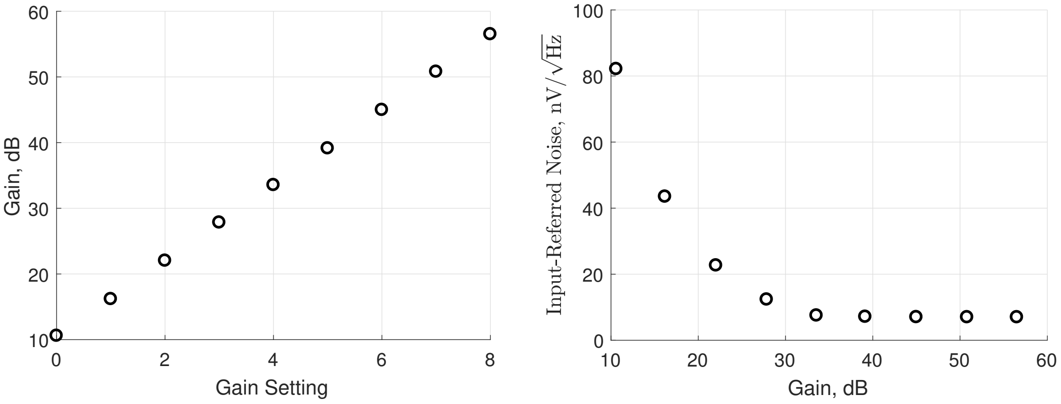

(a) Gain at 2MHz.

(b) Input-referred noise at 2MHz.

Figure 8-15: Effect of VGA gain setting on mid-band gain and input-referred noise.

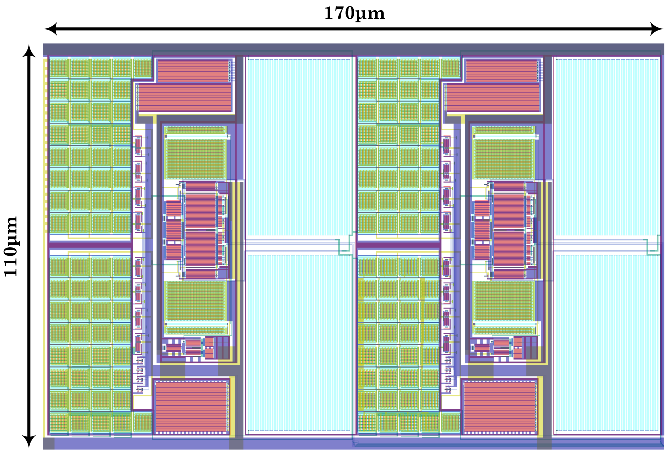

Figure 8-16: VGA layout.

Single channel layout of the integrated VGA is shown in Figure 8-16. Despite sizable feedback resistor area, VGA dimensions of 110μm x 170μm are nonetheless compatible with per-channel transceiver area requirements (i.e., $< 350\mu$m x $< 350\mu$m).

8.2.4 Anti-Aliasing Filter

Analog low-pass filtering is required before sampling to minimize discrete-time aliasing. General purpose AAF architectures must sufficiently reject all spectral content above the Nyquist frequency to ensure minimal degradation of signal-to-noise and distortion ratio (SNDR_c). As observed in Figure 6-11, device nonlinearities and synchronous power supply switching result in harmonic tone generation. Due to underlying coherence, harmonic tones ultimately yield baseband spectral energy within the clutter reject filter stopband and are attenuated in the digital processing domain.

Low-pass filtering for pulsed wave Doppler systems therefore only requires attenuation of non-coherent spectral energy (i.e., noise and external interferers) above the Nyquist frequency. Due to significant attenuation of out-of-band interferers by impedance matching and VGA frequency characteristics, AAF minimum stopband rejection of > 15dB is considered adequate. Due to large combined gain from the LNA and VGA components, noise generation within the AAF is largely irrelevant.

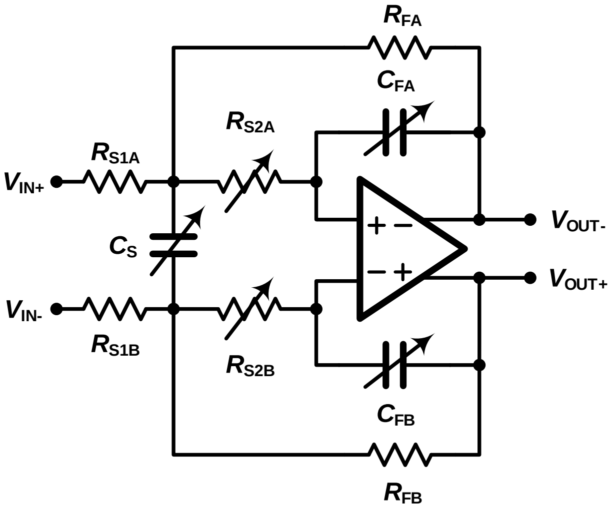

Figure 8-17: Multi-feedback AAF schematic.

The multi-feedback (MBF) AAF architecture shown in Figure 8-17 facilitates configurability of characteristic frequency f_0 and quality factor Q. MFB architectures are commonly preferable over Sallen-Key topologies for AAF design as a result of decreased stop-band rejection sensitivity to op-amp bandwidth, ensuring acceptable attenuation at high frequencies.

Neglecting op-amp nonidealities (i.e., finite gain and bandwidth), the MFB filter transfer function $H_{\text{MFB}}(j\omega)$ is given in Equation 8.3.

$$H_{\text{MFB}}(j\omega) = \frac{\left(\frac{1}{2C_S C_F R_{S1} R_{S2}}\right)}{-\omega^2 + \frac{j\omega}{2C_S R_{S1} R_{S2}}\left[R_{S1} + R_{S2}\left(1 + \frac{R_{S1}}{R_F}\right)\right] + \frac{1}{2C_S C_F R_F R_{S2}}} \tag{8.3}$$

Expressions for characteristic frequency f_0 and quality factor Q are presented in Equations 8.4 and 8.5, respectively.

$$f_0 = \frac{1}{2\pi}\sqrt{\frac{1}{2C_S C_F R_F R_{S2}}} \tag{8.4}$$

$$Q = \frac{\sqrt{\frac{2C_S}{C_F}}}{\sqrt{\frac{R_F}{R_{S2}}} + \sqrt{\frac{R_{S2}}{R_F}} + \frac{\sqrt{R_F R_{S2}}}{R_{S1}}} \tag{8.5}$$

A common resistance value is employed for R_F and R_S, yielding unity gain at low frequencies. Op-amp implementation leverages existing designs from Section 8.2.3. AAF power dissipation of 0.5mW and output swing amplitude > 1.0V is achieved. Post-extraction simulation of AAF gain is given over all frequency and quality factor control settings in Figure 8-18.

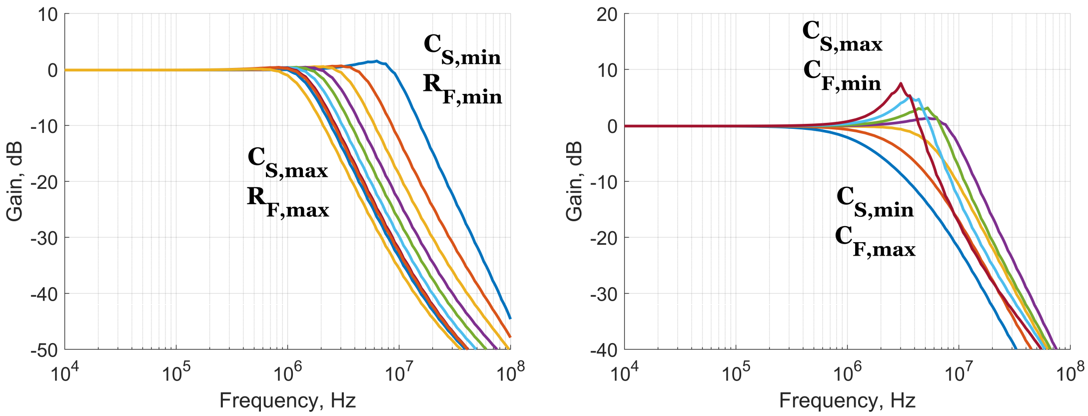

(a) Frequency control settings.

(b) Quality factor control settings.

Figure 8-18: AAF gain for various frequency and quality factor control settings.

Because the AAF proceeds significant amplification within the LNA and VGA, sufficient input compression characteristics are critical to ensure full-scale driving of the ADC input. Figure 8-19 displays AAF gain compression at various 2MHz input signal amplitudes. Near full-scale (i.e., $V_{DD} = 1.2\text{V}$) inputs result in marginal gain compression.

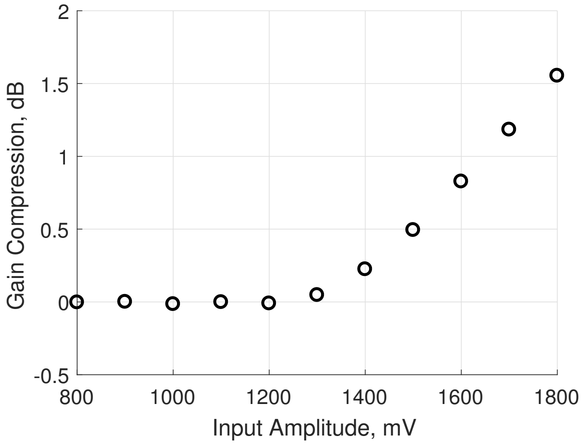

Figure 8-19: AAF gain compression.

For sampling at 8MS/s, spectral energy above > 5.8MHz aliases into the signal band of interest. Figure 8-20(a) presents minimum AAF stopband rejection – relative to gain at 2.2MHz – for all frequency control settings. Similarly, Figure 8-20(b) shows the 1dB attenuation frequency – relative to mid-band gain – for all frequency control settings. Configurable characteristic frequency and quality factor are desirable both for adjustable filter response and to counteract fabrication tolerances associated with integrated passive components.

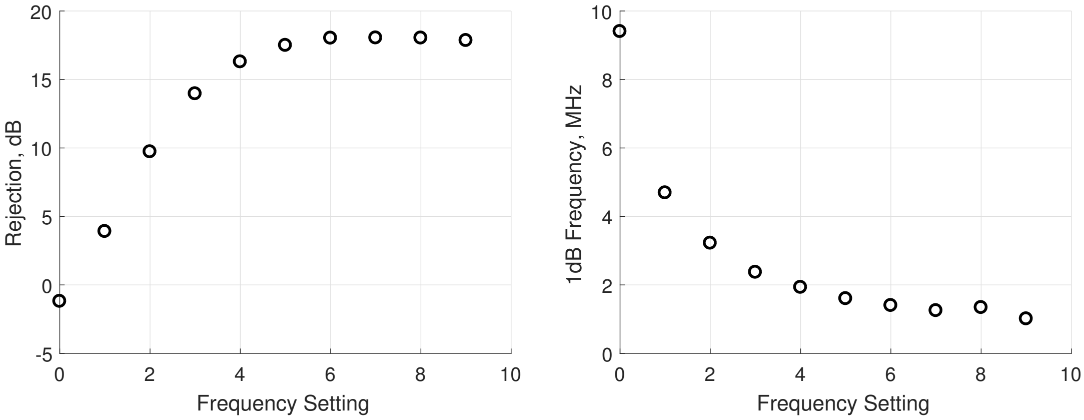

(a) Rejection at 5.8MHz.

(b) 1dB attenuation frequency.

Figure 8-20: AAF frequency control setting effect on stopband rejection and 1dB attenuation frequency.

Layout of the AAF integrated circuit is presented in Figure 8-21. AAF I/O routing is intentionally placed to reduce overall integrated transceiver layout area.

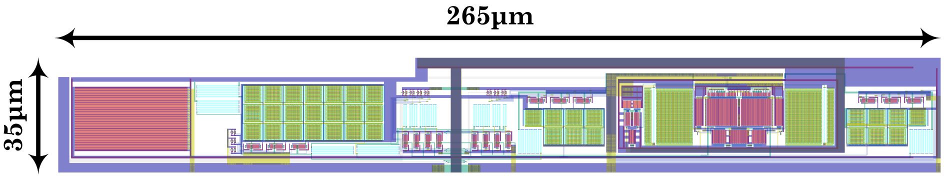

Figure 8-21: AAF layout.

8.2.5 Analog-to-Digital Converter

Successive approximation register (SAR) ADC architectures are appropriate for low power, moderate resolution, and area constrained per-channel signal digitization [98]. To achieve necessary receive beamformer delay timing resolution of 31.25ns, a sampling rate of 8MS/s with quadrature phase clock select is employed. ADC schematic designs were completed by Dante Muratore at the Unversity of Pavia [99].

Acceptable quantization noise is attained for 12-bit SAR operation, where a combined 7-bit capacitive digital-to-analog converter (DAC) and 5-bit resistive DAC architecture is devised to moderate implementation area – as shown in Figure 8-22. Calibration techniques are not considered in this work, but may be necessary for robust, process tolerant ADC implementation.

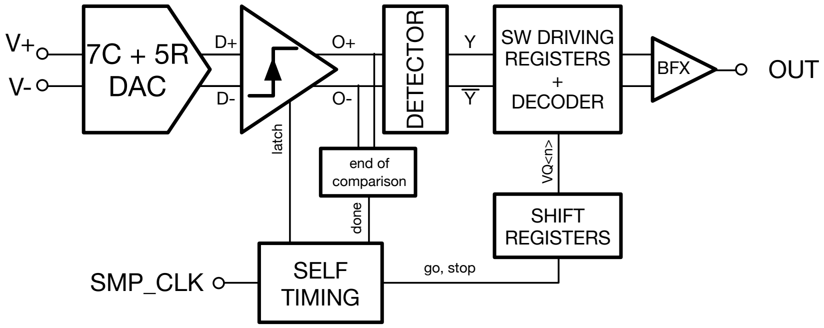

Figure 8-22: Block diagram of area constrained SAR ADC. Adapted from [99].

Metal-insulator-metal (MIM) capacitors are chosen due to reduced parasitics, high density capacitance, and improved mismatch characteristics – relative to commonly available integrated capacitor alternatives. Because harmonic distortions have minimal significance in pulsed Doppler architectures, unit capacitance of the capacitive DAC structure is therefore determined by $\frac{kT}{C}$ noise requirements [97]. MIM unit capacitance of 9.5fF yields 1.2pF total sampling capacitance, resulting in $\frac{kT}{C}$ noise of $\approx 60\mu$V – well below the least-significant bit (LSB) of the ADC. In-depth analysis of the SAR ADC design is presented in [99].

Self-timing logic controls the shift registers and optimizes phase generation within the converter. Coupling between asynchronous digital logic and analog circuitry thereby introduces non-harmonic spectral tones. Interactions between analog and digital signal paths within the ADC – via kickback, capacitive coupling, or other mechanisms – should be minimized to ensure spectral integrity.

Implementation of the SAR ADC occupies $\approx 200\mu$m x 200μm and dissipates 200μW for 8MS/s sampling. Post-extraction simulation of the ADC output spectrum for a 2.21MHz full-scale input is presented in Figure 8-23. For inputs within the relevant frequency band (i.e., $\approx 1.8 - 2.2$MHz), non-harmonic spurious-free dynamic range $\mathrm{SFDR_c} > 75$dBFS and $\mathrm{SNDR_c} > 68$dBFS are obtained over the Nyquist bandwidth.

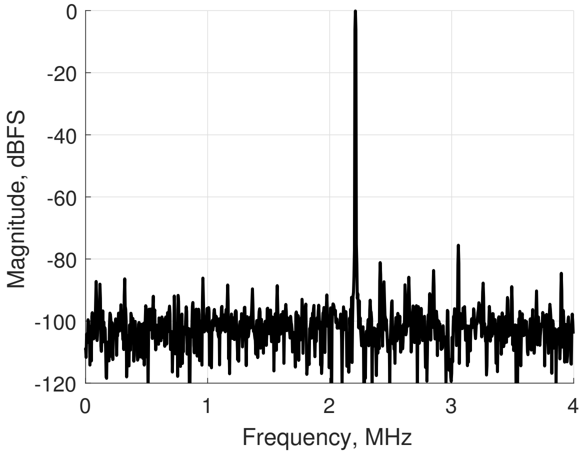

Figure 8-23: ADC spectrum for 2.21MHz full-scale input.

Spectral content within the radio frequency (RF) digital filter passband is displayed in Figure 8-24; no distortion tones are observed for either input signal.

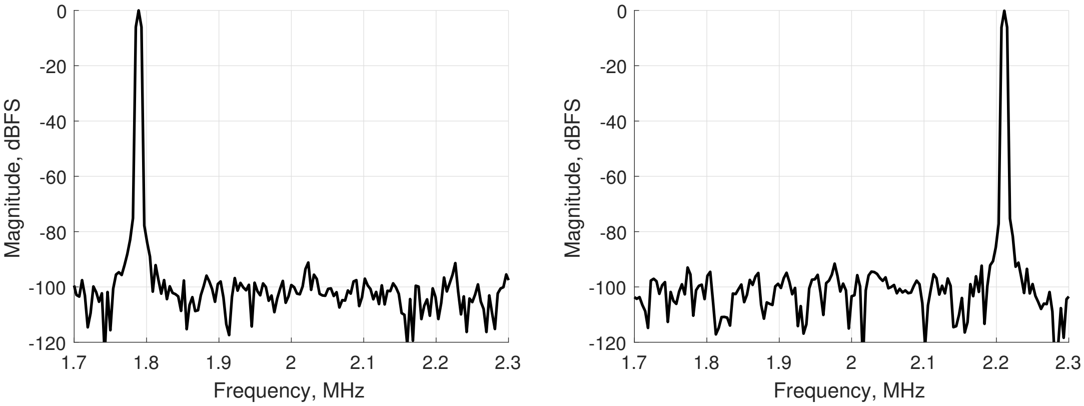

(a) 1.79MHz input frequency.

(b) 2.21MHz input frequency.

Figure 8-24: ADC spectrum of digital filter passband for full-scale inputs.

Layout of the 12-bit SAR ADC implementation is given in Figure 8-25. Despite efforts to severely limit ADC hardware resources, area occupied by the ADC and associated circuitry is the major contributor of total transceiver dimensions.

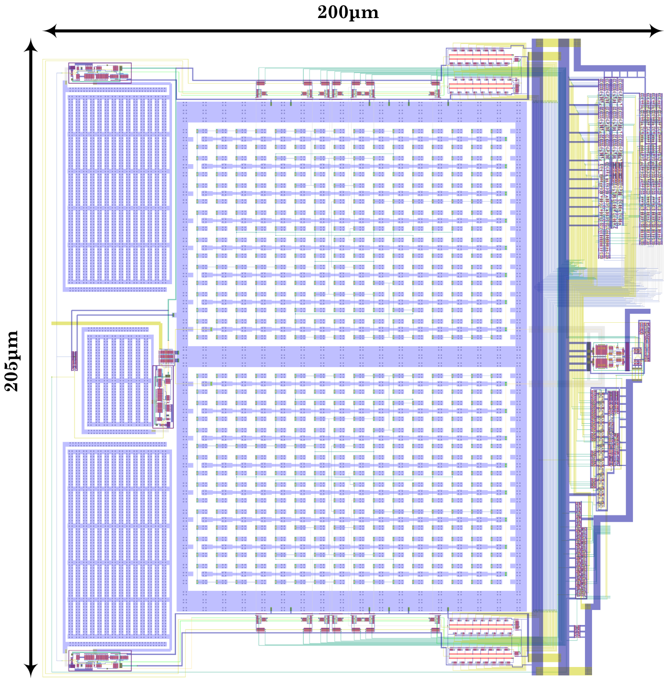

Figure 8-25: 12-bit SAR ADC layout.

The integrated ADC implementation of this work leverages a reduced sample rate of 8MS/s with sampling clock quadrature phase select to achieve necessary timing resolution (i.e., 31.25ns). Because delay coefficient realization is partially embedded within the clock phase select, this technique is only practical for single focus receive beamformation. For multi-focal receive beamformation – notably, hold and tracking methods detailed in Section 4.3.2 – time-interleaving of receive foci between adjacent pulse repetitions is required, thereby reducing maximum detectable blood flow velocity (by the interleaving factor).

Alternately, assuming relatively linear scaling of SAR power dissipation with sampling frequency – for rates $<$ 50MS/s – implementation of 32MS/s SAR conversion has only moderate impact on system power consumption – including corresponding scaling of RF digital signal processing power – and enables independent multi-focal receive beamformation. Although not detailed in this work, complex per-channel phase multiplication – rather than direct sample offsets – can be implemented to realize receive beamformer delays at reduced sampling rates.

8.3 Transceiver and System Integration

An annotated layout of the complete integrated transceiver channel is given in Figure 8-26. Separate deep N-wells and dual substrate guard rings are defined for each subcircuit to reduce substrate coupling. The integrated transceiver consumes 3.5mW – including transmit power supplies under transducer element loading – and occupies a die area of 275μm x 320μm. Integration of 64 channels of transceiver electronics – and relevant digital circuitry – within a 4mm x 4mm die area is established. Parasitics due to flip-chip interconnection between the ASIC and phased array system are expected to have minimal effect on signal path impedance for analog I/O frequencies (i.e., $\lesssim$ 10MHz).

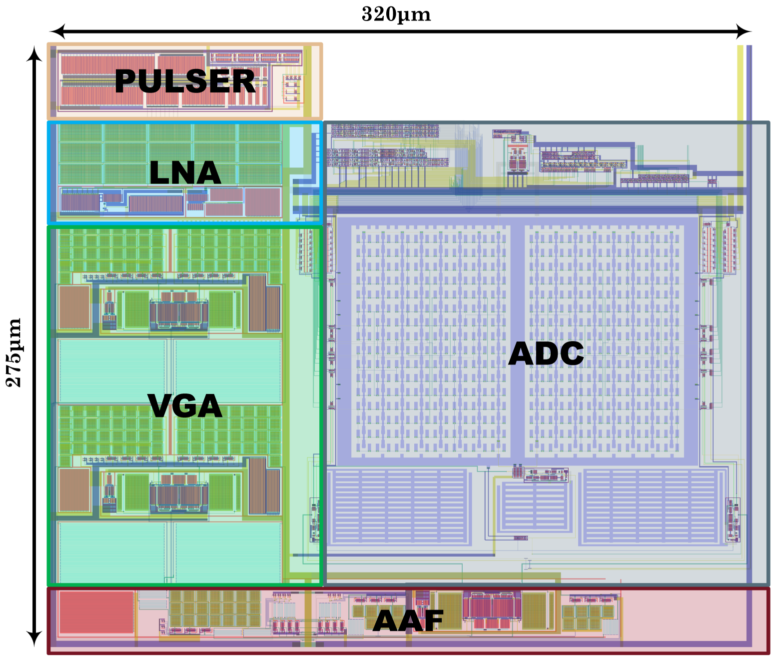

Figure 8-26: Annotated transceiver channel layout.

Analog gain of the integrated transceiver is presented in Figure 8-27 over various gain and frequency control settings, yielding combined mid-band gain from 27dB to 75dB with 6dB resolution.

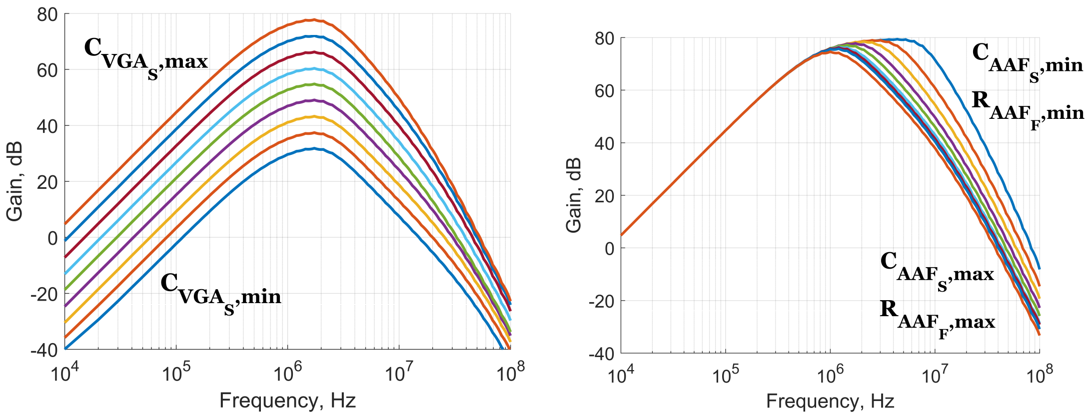

(a) Gain control settings.

(b) Frequency control settings.

Figure 8-27: Transceiver gain and frequency control effect on receive characteristics.

Inclusion of the impedance matching network and transducer element loading alters the receive path characteristics. Figure 8-28 exhibits these effects on gain and input-referred voltage noise – where ASIC data corresponds solely to the integrated transceiver and element data includes thermal noise due to transducer motional resistance and voltage division within the matching network.

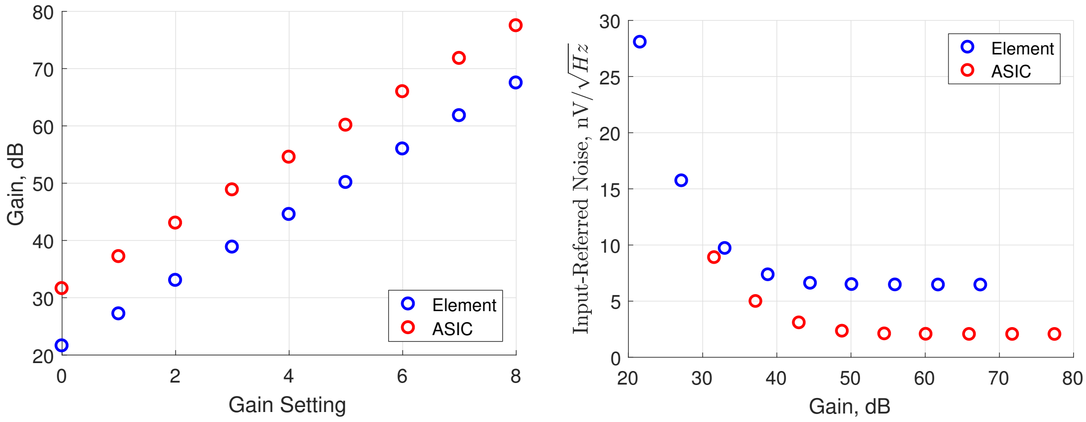

(a) Gain at 2MHz.

(b) Input-referred noise at 2MHz.

Figure 8-28: Effect of transceiver gain setting on mid-band gain and input-referred noise, including transducer element and impedance matching network loading.

Inclusion of the ASIC in the integrated phased array system – shown in Figure 8-1 – results in 64 channels of transceiver and beamforming electronics on a single die, with baseband signal processing and high-level control maintained within the MCU.

Gross estimation of power consumption for the integrated phased array system is given in Figure 8-29; considerable overhead is allocated to account for power regulation, voltage references, clock management, and output drivers within the ASIC. MCU operation is largely responsible for the significant proportion of digital power consumption within the integrated system.

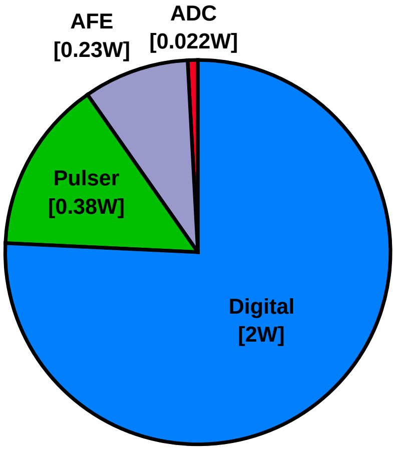

Figure 8-29: Estimated integrated prototype power consumption.

Although approximate, a pronounced decrease in phased array system power – from 21W to ≈ 2.6W (≈ 12%) – is achieved via integrated circuit design specific to the requirements of TCD sonography. Notably, ADC and AFE power dissipation is 0.6% and 1.7% compared to values attained for discrete system hardware, respectively. Vast reductions in system power demands and electrical hardware resources enable significant miniaturization of prototype system form factor. Such improvements – in addition to refinements in transducer array design and system interconnections – facilitate highly-wearable implementations of TCD velocimetry instrumentation.

8.4 Summary

This chapter presents an ASIC-based Doppler velocimetry system architecture. An ASIC is designed in a standard 65nm CMOS process and achieves 64 channel transceiver operation in a 4mm x 4mm die area. Transistor level designs for the transmit pulser, T/R switch, LNA, VGA, AAF, and ADC are given. Post-extraction simulations achieve comparable performance to the existing discrete prototype system with significant reductions in hardware dimensions and system power consumption.

Chapter 9

Conclusion

9.1 Summary

Monitoring of cerebrovascular state is an essential element in the clinical care of cerebrovascular pathologies. Transcranial Doppler (TCD) sonography is a noninvasive method that enables measurement of blood flow velocities from the basal intracerebral vessels and is clinically indicated in a variety of diagnostic and prognostic cerebrovascular applications [2]. Although TCD sonography provides several considerable advantages when compared to other measurement modalities – notably safety in prolonged studies, relatively modest system dimensions and equipment costs, and high temporal resolution – the widespread clinical acceptance and adoption of TCD sonography in both conventional (e.g., identification of intracranial vasospasm and stenosis, cerebral embolism detection) and emerging (e.g., intracranial pressure estimation) applications has been hindered by numerous limitations [10, 11]. Among these impediments are the need for an experienced operator, velocimetry accuracy and signal integrity concerns, and severe patient movement restrictions.

In an effort to mitigate these constraints, this work details the development of a compact, wearable TCD ultrasound system for autonomous and continuous measurement of cerebral blood flow velocity (CBFV). To facilitate development, this work concentrates on unilateral insonation of the middle cerebral artery (MCA).

Relevant theoretical considerations and design of a discrete prototype phased array system were presented in Chapters 2 to 5. The 64 channel discrete prototype was experimentally characterized in Chapter 6 and validated under human testing in Chapter 7. An investigation into integrated circuit design for reduced power dissipation and decreased system dimensions was presented in Chapter8.

A wearable, extended monitoring TCD system concept is presented in Figure 9-1. Practical realization of this conceptual system requires further refinement of electrical hardware, improvements to algorithmic operation, miniaturization of transducer array hardware and interconnections, and significant improvements to system mechanical designs to ensure sufficient acoustic coupling and transducer array positioning.

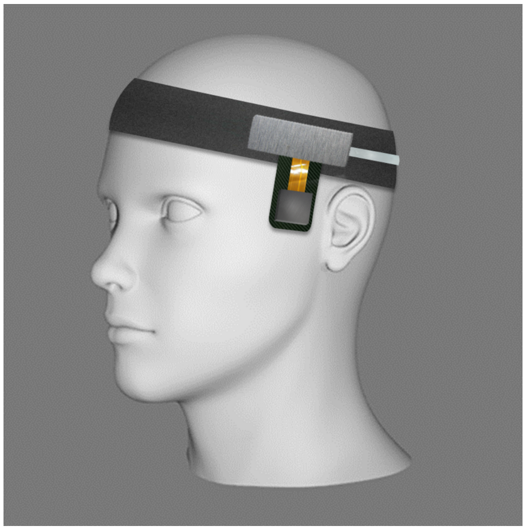

Figure 9-1: Wearable TCD monitoring concept.

9.2 Future Work

The following items are anticipated next steps related to wearable TCD monitoring systems with limited operator interaction:

- **Development of increased channel count systems**
  A 64 channel TCD architecture was chosen primarily to limit electrical hardware resources to a reasonably compact form factor. This decision imposed significant limitations on acoustic beamformation and thereby on vessel search and tracking functionality. Extension to higher channel count systems – ≈ 256 to 512 ele-

ments – will allow for increased beam steering angles and further improvements to autonomous system functionality. Achieving higher channel count operation under acceptable power dissipation ($\lesssim$ 5W) and wearable size constraints likely requires application specific circuit integration.

- **Development of improved acoustic window finding methods**
  Although vessel search and tracking algorithms enabled reductions in TCD operator interaction, significant effort was nonetheless needed to locate an acceptable acoustic window. Using ultrasonic methods to directly estimate skull thickness – as is done for the focal correction methods presented in Chapter 4 – may lead to rapid determination of optimal transducer placement. The window finding method of this work – which requires volumetric Doppler mapping at each potential acoustic window location – proved burdensome, especially in subjects where an appropriate acoustic window could not be approximately determined via palpation.

- **Use case refinement**
  Further exploration into potential use cases of autonomous TCD sonography may lead to system level modifications in future prototype development. Such revisions may include the need for bilateral insonation modes, extension to insonation of additional cerebral vessels, modification of the operator interface and mechanical construction, motorized transducer array positioning, and methods of radio-based data transmission. Input from clinicians, sonographers, and other potential users is necessary.

The successful execution of our current objectives and future work has potential to profoundly alter the current clinical approach to cerebrovascular diagnostics, especially in cases where the role of diagnostic tools has not been clearly established (e.g., emergency assessment of head trauma and stroke, ambulatory intracranial pressure monitoring for cases of moderate traumatic brain injury, home monitoring of hydrocephalus shunt function, long-term monitoring cerebral embolization).

Bibliography

[1] R. W. Baumgartner, "Transcranial color-coded duplex sonography," *Journal of Neurology*, vol. 246, no. 8, pp. 637–647, 1999.

[2] M. A. Sloan, A. V. Alexandrov, C. Tegeler, *et al.*, "Transcranial Doppler ultrasonography in 2004: a comprehensive evidence-based update," *Neurology*, vol. 62, no. 9, pp. 1468–1481, 2004.

[3] S.-C. Tang, J.-S. Jeng, P.-K. Yip, C.-J. Lu, B.-S. Hwang, W.-H. Lin, and H.-M. Liu, "Transcranial color-coded sonography for the detection of middle cerebral artery stenosis," *Journal of Ultrasound in Medicine*, vol. 24, no. 4, pp. 451–457, 2005.

[4] P. Hanlo, R. Peters, R. Gooskens, R. Heethaar, R. Keunen, A. Van Huffelen, C. Tulleken, and J. Willemse, "Monitoring intracranial dynamics by transcranial Dopplera new Doppler index: trans systolic time," *Ultrasound in Medicine & Biology*, vol. 21, no. 5, pp. 613–621, 1995.

[5] N. A. Martin, K. M. Thomas, and M. Caron, "Transcranial Doppler–techniques, application, and instrumentation," *Neurosurgery*, vol. 33, pp. 761–764, Oct. 1993.

[6] S. J. Pietrangelo, "An electronically steered, wearable transcranial Doppler ultrasound system," Master's thesis, Massachusetts Institute of Technology, 2013.

[7] A. V. Alexandrov, V. L. Babikian, R. J. Adams, C. H. Tegeler, L. R. Caplan, M. P. Spencer, N. S. A. P. on Transcranial Doppler, *et al.*, "The evolving role of transcranial Doppler in stroke prevention and treatment," *Journal of Stroke and Cerebrovascular Diseases*, vol. 7, no. 2, pp. 101–104, 1998.

[8] M. Saqqur, D. Zygun, and A. Demchuk, "Role of transcranial Doppler in neurocritical care," *Critical Care Medicine*, vol. 35, no. 5, pp. S216–S223, 2007.

[9] H. S. Markus, "Transcranial Doppler ultrasound," *British Medical Bulletin*, vol. 56, no. 2, pp. 378–388, 2000.

[10] Q. Shen, J. Stuart, B. Venkatesh, J. Wallace, and J. Lipman, "Inter observer variability of the transcranial Doppler ultrasound technique: Impact of lack of practice on the accuracy of measurement," *Journal of Clinical Monitoring and Computing*, vol. 15, pp. 179–184, 1999.

[11] B. Venkatesh, Q. Shen, and J. Lipman, "Continuous measurement of cerebral blood flow velocity using transcranial Doppler reveals significant moment-to-moment variability of data in healthy volunteers and in patients with subarachnoid hemorrhage," *Crit Care Med*, vol. 30, pp. 563–569, Mar. 2002.

[12] R. Aaslid, *Transcranial Doppler sonography.* Wien, Austria: Springer-Verlag, first ed., 1986.

[13] H. White and B. Venkatesh, "Applications of transcranial Doppler in the ICU: a review," *Intensive Care Medicine*, vol. 32, pp. 981–994, 2006.

[14] C. J. McMahon, P. McDermott, D. Horsfall, J. R. Selvarajah, A. T. King, and A. Vail, "The reproducibility of transcranial Doppler middle cerebral artery velocity measurements: implications for clinical practice," *Br J Neurosurg*, vol. 21, pp. 21–27, Feb. 2007.

[15] M. Corriveau and K. Johnston, "Interobserver variability of carotid Doppler peak velocity measurements among technologists in an ICAVL- accredited vascular laboratory," *Journal of Vascular Surgery*, vol. 39, no. 4, pp. 735–741, 2004.

[16] L. R. Wechsler and V. L. Babikian, "Transcranial Doppler sonography: Clinically useful," *Arch Neurol*, vol. 51, pp. 1054–1056, Oct. 1994.

[17] M. A. Moehring and M. P. Spencer, "Power M-mode Doppler (PMD) for observing cerebral blood flow and tracking emboli," *Ultrasound Med Biol*, vol. 28, pp. 49–57, Jan. 2002.

[18] P. Martin, D. Evans, and A. Naylor, "Measurement of blood flow velocity in the basal cerebral circulation: Advantages of transcranial color-coded sonography over conventional transcranial doppler," *Journal of Clinical Ultrasound*, vol. 23, no. 1, pp. 21–26, 1995.

[19] H. S. Markus, "Transcranial Doppler ultrasound," *Journal of Neurology, Neurosurgery & Psychiatry*, vol. 67, no. 2, pp. 135–137, 1999.

[20] M. Marinoni, A. Ginanneschi, P. Forleo, and L. Amaducci, "Technical limits in transcranial Doppler recording: Inadquate acoustic windows," *Ultrasound in Medicine & Biology*, vol. 23, no. 8, pp. 1275–1277, 1997.

[21] T. Gerriets, G. Seidel, I. Fiss, B. Modrau, and M. Kaps, "Contrast-enhanced transcranial color-coded duplex sonography: efficiency and validity," *Neurology*, vol. 52, pp. 1133–1137, Apr. 1999.

[22] H. S. Markus and A. MacKinnon, "Asymptomatic embolization detected by Doppler ultrasound predicts stroke risk in symptomatic carotid artery stenosis," *Stroke*, vol. 36, no. 5, pp. 971–975, 2005.

[23] A. D. Mackinnon, R. Aaslid, and H. S. Markus, "Ambulatory transcranial Doppler cerebral embolic signal detection in symptomatic and asymptomatic carotid stenosis," *Stroke*, vol. 36, no. 8, pp. 1726–1730, 2005.

[24] C. S. Kidwell, N. A. Martin, and J. L. Saver, "A new pocket-sized transcranial ultrasound device (neurodop): Comparison with standard tcd," *Journal of Neuroimaging*, vol. 10, no. 2, pp. 91–95, 2000.

[25] R. W. Baumgartner, ed., *Handbook on neurovascular ultrasound*, vol. 21 of *Frontiers of neurology and neuroscience.* Basel, Switzerland: Karger, first ed., 2006.

[26] A. D. Mackinnon, R. Aaslid, and H. S. Markus, "Long-term ambulatory monitoring for cerebral emboli using transcranial Doppler ultrasound," *Stroke*, vol. 35, no. 1, pp. 73–78, 2004.

[27] G. T. Clement, J. White, and K. Hynynen, "Investigation of a large-area phased array for focused ultrasound surgery through the skull," *Phys Med Biol*, vol. 45, pp. 1071–1083, Apr. 2000.

[28] S. Deverson, D. H. Evans, and D. Bouch, "The effects of temporal bone on transcranial Doppler ultrasound beam shape," *Ultrasound in Medicine & Biology*, vol. 26, no. 2, pp. 239–244, 2000.

[29] J. Jensen, "Field: A program for simulating ultrasound systems," *Medical and Biological Engineering and Computing*, vol. 34, Supplement 1, pp. 351–353, 1996.

[30] J. Jensen and N. Svendsen, "Calculation of pressure fields from arbitrarily shaped, apodized, and excited ultrasound transducers," *Ultrasonics, Ferroelectrics and Frequency Control, IEEE Transactions on*, vol. 39, no. 2, pp. 262–267, 1992.

[31] B. E. Treeby and B. T. Cox, "k-wave: Matlab toolbox for the simulation and reconstruction of photoacoustic wave fields," *Journal of Biomedical Optics*, vol. 15, no. 2, pp. 021314–021314, 2010.

[32] T. L. Szabo, *Diagnostic ultrasound imaging: inside out.* Academic Press Series in Biomedical Engineering, Burlington, MA: Elsevier Academic Press, first ed., 2004.

[33] J. A. Jensen, *Estimation of blood velocities using ultrasound: a signal processing approach.* New York, NY: Cambridge University Press, first ed., 1996.

[34] D. A. Christensen, *Ultrasonic bioinstrumentation.* New York, NY: John Wiley & Sons, first ed., 1988.

[35] F. T. Ulaby, *Fundamentals of applied electromagnetics.* Upper Saddle River, NJ: Pearson Prentice Hall, fifth ed., 2007.

[36] D. Evans and W. McDicken, *Doppler ultrasound: physics, instrumentation, and signal processing.* New York, NY: Wiley, second ed., 2000.

[37] D. K. Nassiri and C. R. Hill, "The differential and total bulk acoustic scattering cross sections of some human and animal tissues," *The Journal of the Acoustical Society of America*, vol. 79, no. 6, pp. 2034–2047, 1986.

[38] T. Duck, A. Baker, and H. Starritt, eds., *Ultrasound in medicine.* Medical science series, Bristol, UK: Institute of Physics Publishing, first ed., 1998.

[39] K. K. Shung and G. Thieme, eds., *Ultrasonic scattering in biological tissues.* Boca Raton, FL: CRC, first ed., 1993.

[40] Y. W. Yuan and K. K. Shung, "Ultrasonic backscatter from flowing whole blood – I: Dependence on shear rate and hematocrit," *The Journal of the Acoustical Society of America*, vol. 84, no. 1, pp. 52–58, 1988.

[41] A. Oliner, R. Li, and H. Bertoni, "Catalog of acoustic equivalent networks for planar interfaces," *Proceedings of the IEEE*, vol. 60, pp. 1513–1518, Dec. 1972.

[42] M. Hayner and K. Hynynen, "Numerical analysis of ultrasonic transmission and absorption of oblique plane waves through the human skull," *The Journal of the Acoustical Society of America*, vol. 110, no. 6, pp. 3319–3330, 2001.

[43] G. T. Clement, P. J. White, and K. Hynynen, "Enhanced ultrasound transmission through the human skull using shear mode conversion," *The Journal of the Acoustical Society of America*, vol. 115, no. 3, pp. 1356–1364, 2004.

[44] G. Tupholme, "Generation of acoustic pulses by baffled plane pistons," *Mathematika*, vol. 16, pp. 209–224, 1969.

[45] P. R. Stepanishen, "Transient radiation from pistons in an infinite planar baffle," *The Journal of the Acoustical Society of America*, vol. 49, no. 5B, pp. 1629–1638, 1971.

[46] J. A. Jensen, "A model for the propagation and scattering of ultrasound in tissue," *The Journal of the Acoustical Society of America*, vol. 89, no. 1, pp. 182–190, 1991.

[47] P. Stepanishen, "Pulsed transmit/receive response of ultrasonic piezoelectric transducers," *The Journal of the Acoustical Society of America*, vol. 69, pp. 1815–1827, 1981.

[48] B. D. Steinberg, "Digital beamforming in ultrasound," *IEEE Trans Ultrason Ferroelectr Freq Control*, vol. 39, no. 6, pp. 716–721, 1992.

[49] U. Vyas and D. Christensen, "Ultrasound beam simulations in inhomogeneous tissue geometries using the hybrid angular spectrum method," *IEEE Trans Ultrason Ferroelectr Freq Control*, vol. 59, pp. 1093–1100, Jun. 2012.

[50] F. M. Kashif, *Modeling and estimation for non-invasive monitoring of intracranial pressure and cerebrovascular autoregulation.* PhD thesis, Massachusetts Institute of Technology, 2011.

[51] E. Kandel, J. Schwartz, T. Jessell, *et al.*, *Principles of neural science*, vol. 4. McGraw-Hill New York, 2000.

[52] M. de Boorder, J. van der Grond, A. van Dongen, C. Klijn, L. Jaap Kappelle, P. Van Rijk, and J. Hendrikse, "Spect measurements of regional cerebral perfusion and carbondioxide reactivity: Correlation with cerebral collaterals in internal carotid artery occlusive disease," *Journal of Neurology*, vol. 253, no. 10, pp. 1285–1291, 2006.

[53] H. Gray, *Anatomy of the human body.* Lea & Febiger, 1918.

[54] Wikipedia, "Circle of Willis — Wikipedia, the free encyclopedia," 2012. [Online; accessed 3 November 2012].

[55] D. Newell and R. Aaslid, *Transcranial Doppler.* New York, NY: Raven Press, first ed., 1992.

[56] T. JF, *Cerebrovascular disorders.* New York, NY: Raven Press, third ed., 1984.

[57] T. Gabrielsen and T. Greitz, "Normal size of the internal carotid, middle cerebral and anterior cerebral arteries," *Acta Radiologica: Diagnosis*, vol. 10, no. 1, pp. 1–10, 1970.

[58] K. K. Jain, "Some observations on the anatomy of the middle cerebral artery," *Canadian Journal of Surgery*, vol. 7, pp. 134–139, 1964.

[59] A. Comerota, M. Katz, J. Hosking, H. Hashemi, R. Kerr, and A. Carter, "Is transcranial Doppler a worthwhile addition to screening tests for cerebrovascular disease?," *Journal of Vascular Surgery*, vol. 21, no. 1, pp. 90–97, 1995.

[60] A. Harders and J. Gilsbach, "Transcranial Doppler sonography and its application in extracranial-intracranial bypass surgery," *Neurol Res*, vol. 7, pp. 129–141, Sep. 1985.

[61] E. Bartels and K. Flügel, "Quantitative measurements of blood flow velocity in basal cerebral arteries with transcranial duplex color-flow imaging: A comparative study with conventional transcranial doppler sonography," *Journal of Neuroimaging*, vol. 4, no. 2, pp. 77–81, 1994.

[62] K. A. Fujioka, D. T. Gates, and M. P. Spencer, "A comparison of transcranial color doppler imaging and standard static pulsed wave doppler in the assessment of intracranial hemodynamics," *Journal of Vascular Technology*, vol. 18, no. 1, pp. 29–35, 1994.

[63] B. M. Eicke, C. H. Tegeler, G. Dalley, and L. G. Myers, "Angle correction in transcranial doppler sonography," *Journal of Neuroimaging*, vol. 4, no. 1, pp. 29–33, 1994.

[64] A. Lupetin, D. Davis, I. Beckman, and N. Dash, "Transcranial Doppler sonography. part 1. principles, technique, and normal appearances," *Radiographics*, vol. 15, no. 1, pp. 179–191, 1995.

[65] A. A. Jarquin-Valdivia, J. McCartney, D. Palestrant, S. C. Johnston, and D. Gress, "The thickness of the temporal squama and its implication for transcranial sonography," *Journal of Neuroimaging*, vol. 14, no. 2, pp. 139–142, 2004.

[66] T. Postert, J. Federlein, H. Przuntek, and T. Büttner, "Insufficient and absent acoustic temporal bone window: potential and limitations of transcranial contrast-enhanced color-coded sonography and contrast-enhanced power-based sonography," *Ultrasound in Medicine & Biology*, vol. 23, no. 6, pp. 857–862, 1997.

[67] U. Bogdahn, G. Becker, R. Schlief, J. Reddig, and W. Hassel, "Contrast-enhanced transcranial color-coded real-time sonography. results of a phase-two study.," *Stroke*, vol. 24, no. 5, pp. 676–684, 1993.

[68] U.S. Department of Health and Human Services, *Guidance for industry and FDA staff - information for manufacturers seeking marketing clearance of diagnostic ultrasound systems and transducers.* U.S. Department of Health and Human Services, Rockville, MD, 2008.

[69] AIUM, *Bioeffects and safety of diagnostic ultrasound.* Laurel, MD: AIUM Publications, 1998.

[70] British Medical Ultrasound Society, *Guidelines for the safe use of diagnostic ultrasound equipment.* British Medical Ultrasound Society, London, UK, 2009.

[71] Spencer Technologies, *ST3 Digital Transcranial Doppler System Model PMD150 Operator's Manual.* Spencer Tecchnologies, Seattle, WA, 2009.

[72] K. Lindegaard, T. Lundar, J. Wiberg, D. Sjøberg, R. Aaslid, and H. Nornes, "Variations in middle cerebral artery blood flow investigated with noninvasive transcranial blood velocity measurements," *Stroke*, vol. 18, no. 6, pp. 1025–1030, 1987.

[73] O. Bonnefous, P. Pesque, and X. Bernard, "A new velocity estimator for color flow mapping," in *IEEE 1986 Ultrasonics Symposium*, pp. 855–860, IEEE, 1986.

[74] C. Kasai, K. Namekawa, A. Koyano, and R. Omoto, "Real-time two-dimensional blood flow imaging using an autocorrelation technique," *IEEE Trans. Sonics Ultrason*, vol. 32, no. 3, pp. 458–464, 1985.

[75] P. Magnin, "A review of Doppler flow mapping techniques," in *IEEE 1987 Ultrasonics Symposium*, pp. 969–978, IEEE, 1987.

[76] A. Oppenheim and R. Schafer, *Discrete-time signal processing.* Upper Saddle River, NJ: Prentice Hall, third ed., 2010.

[77] P. Keeton and F. Schlindwein, "Spectral broadening of clinical Doppler signals using FFT and autoregressive modelling," *European Journal of Ultrasound*, vol. 7, no. 3, pp. 209–218, 1998.

[78] D. H. Evans, *Doppler ultrasound: Physics, instrumentation, and clinical applications.* John Wiley & Sons, 1989.

[79] W. Nichols, M. O'Rourke, and C. Vlachopoulos, *McDonald's blood flow in arteries: theoretical, experimental and clinical principles.* CRC Press, 2011.

[80] J. Womersley, "Oscillatory motion of a viscous liquid in a thin-walled elastic tube – I: The linear approximation for long waves," *Philosophical Magazine*, vol. 46, no. 373, pp. 199–221, 1955.

[81] D. Evans, "Some aspects of the relationship between instantaneous volumetric blood flow and continuous wave Doppler ultrasound recordings – III," *Ultrasound in Medicine & Biology*, vol. 8, no. 6, pp. 617–623, 1982.

[82] T. DAlessio, "objectivealgorithm for maximum frequency estimation in doppler spectral analysers," *Medical and Biological Engineering and Computing*, vol. 23, no. 1, pp. 63–68, 1985.

[83] L. Allard, Y. E. Langlois, L.-G. Durand, G. O. Roederer, M. Beaudoin, G. Cloutier, P. Roy, and P. Robillard, "Computer analysis and pattern recognition of doppler blood flow spectra for disease classification in the lower limb arteries," *Ultrasound in Medicine & Biology*, vol. 17, no. 3, pp. 211–223, 1991.

[84] Z. Guo, L.-G. Durand, L. Allard, G. Cloutier, H. Lee, and Y. Langlois, "Cardiac doppler blood-flow signal analysis," *Medical and Biological Engineering and Computing*, vol. 31, no. 3, pp. 242–248, 1993.

[85] P. Keeton and F. Schlindwein, "Application of wavelets in Doppler ultrasound," *Sensor Review*, vol. 17, no. 1, pp. 38–45, 1997.

[86] I. A. Wright, N. A. Gough, F. Rakebrandt, M. Wahab, and J. P. Woodcock, "Neural network analysis of Doppler ultrasound blood flow signals: A pilot study," *Ultrasound in Medicine & Biology*, vol. 23, no. 5, pp. 683–690, 1997.

[87] G. Cloutier, F. Lemire, L.-G. Durand, Y. Latour, and Y. E. Langlois, "Computer evaluation of Doppler spectral envelope area in patients having a valvular aortic stenosis," *Ultrasound in Medicine & Biology*, vol. 16, no. 3, pp. 247–260, 1990.

[88] L. Y. Mo, L. C. Yun, and R. Cobbold, "Comparison of four digital maximum frequency estimators for Doppler ultrasound," *Ultrasound in Medicine & Biology*, vol. 14, no. 5, pp. 355–363, 1988.

[89] H. Akaike, "A new look at the statistical model identification," *IEEE Transactions on Automatic Control*, vol. 19, no. 6, pp. 716–723, 1974.

[90] K. Hynynen and F. Jolesz, "Demonstration of potential noninvasive ultrasound brain therapy through an intact skull," *Ultrasound in Medicine & Biology*, vol. 24, no. 2, pp. 275–283, 1998.

[91] G. T. Clement and K. Hynynen, "A non-invasive method for focusing ultrasound through the human skull," *Phys Med Biol*, vol. 47, pp. 1219–1236, Apr. 2002.

[92] F. Fry and J. Barger, "Acoustical properties of the human skull," *The Journal of the Acoustical Society of America*, vol. 63, no. 5, pp. 1576–1590, 1978.

[93] J. A. Jensen and Y. Li, "Imaging blood's velocity using synthetic aperture ultrasound," in *Synthetic Aperture Radar, 2012. EUSAR. 9th European Conference on*, pp. 42–45, VDE, 2012.

[94] A. Arnau *et al.*, *Piezoelectric transducers and applications*, vol. 2004. Springer, 2004.

[95] G. Tsivgoulis, V. Sharma, and A. Alexandrov, "Multi-depth power M-mode Doppler in the evaluation of acute cerebral ischemia," in *Science Innovation Synergy Symposiums in Cardiac and Vascular Medicine 2007 Yearbook*, pp. 42–54, 2007.

[96] J. C. García, J. A. Montiel-Nelson, and S. Nooshabadi, "High performance cmos dual supply level shifter for a 0.5V input and 1V output in standard 1.2V 65nm technology process," in *Communications and Information Technology, 2009. ISCIT 2009. 9th International Symposium on*, pp. 963–966, IEEE, 2009.

[97] B. Razavi, *Design of Analog CMOS Integrated Circuits.* McGraw-Hill, 2001.

[98] C.-C. Liu, S.-J. Chang, G.-Y. Huang, Y.-Z. Lin, C.-M. Huang, C.-H. Huang, L. Bu, and C.-C. Tsai, "A 10b 100MS/s 1.13mw SAR ADC with binary-scaled error compensation," in *2010 IEEE International Solid-State Circuits Conference-(ISSCC)*, 2010.

[99] D. G. Muratore, *A study of successive approximatino register ADC architectures.* PhD thesis, University of Pavia, 2016.